VISUAL SALIENCY IN VIDEO COMPRESSION AND TRANSMISSION

by

Hadi Hadizadeh

M.Sc., Iran University of Science and Technology, 2008

B.Sc., Shahrood University of Technology, 2005

A Thesis submitted in partial fulfillment of
the requirements for the degree of

Doctor of Philosophy

in the
School of Engineering Science
Faculty of Applied Sciences

SIMON FRASER UNIVERSITY
Spring 2013

APPROVAL

Name: Hadi Hadizadeh

Degree: Doctor of Philosophy

Title of Thesis: Visual Saliency in Video Compression and Transmission

Examining Committee: Dr. Andrew Rawicz
Chair, Professor, School of Engineering Science

Dr. Ivan V. Bajić, Senior Supervisor,
Associate Professor, School of Engineering Science

Dr. Parvaneh Saeedi, Supervisor,
Associate Professor, School of Engineering Science

Dr. Jie Liang, Supervisor,
Associate Professor, School of Engineering Science

Dr. Rodney G. Vaughan, Internal Examiner,
Professor, School of Engineering Science

Dr. Zhou Wang, External Examiner,
Associate Professor, Electrical and Computer Engineering, University of Waterloo

Date Approved: April 18, 2013

Partial Copyright Licence

Abstract

This dissertation explores the concept of visual saliency—a measure of propensity for drawing visual attention—and presents various novel methods for utilization of visual saliency in video compression and transmission. Specifically, a computationally-efficient method for visual saliency estimation in digital images and videos is developed, which approximates one of the most well-known visual saliency models. In the context of video compression, a saliency-aware video coding method is proposed within a region-of-interest (ROI) video coding paradigm. The proposed video coding method attempts to reduce attention-grabbing coding artifacts and keep viewers' attention in areas where the quality is highest. The method allows visual saliency to increase in high quality parts of the frame, and allows saliency to reduce in non-ROI parts. Using this approach, the proposed method is able to achieve the same subjective quality as competing state-of-the-art methods at a lower bit rate. In the context of video transmission, a novel saliency-cognizant error concealment method is presented for ROI-based video streaming in which regions with higher visual saliency are protected more heavily than low saliency regions. In the proposed error concealment method, a low-saliency prior is added to the error concealment process as a regularization term, which serves two purposes. First, it provides additional side information for the decoder to identify the correct replacement blocks for concealment. Second, in the event that a perfectly matched block cannot be unambiguously identified, the low-saliency prior reduces viewers' visual attention on the loss-stricken regions, resulting in higher overall subjective quality. During the course of this research, an eye-tracking dataset for several standard video sequences was created and made publicly available. This dataset can be utilized to test saliency models for video and evaluate various perceptually-motivated algorithms for video processing and video quality assessment.

To my lovely parents and family

Acknowledgements

I am thankful to many people for helping me during my Ph.D. program at Simon Fraser University (SFU). Without their help, I would not be able to complete my program.

First and foremost, I wish to express my sincere gratitude and appreciation to my senior supervisor, Prof. Ivan V. Bajić, for his persistent support and guidance during my doctoral work. I would like to thank him for allowing me the freedom to explore my research and industrial interests, with continual understanding, encouragement, and intellectual support. I have learned a lot from him during my Ph.D. years. Many of his brilliant ideas have become the very foundation of the present dissertation. He was the first person who introduced me to the concept of visual saliency. I will always remain thankful and grateful to him.

I would also like to thank my supervisor, Prof. Parvaneh Saeedi. She was one of my main motivations for coming to SFU for my graduate studies. During the past four years, I had a very good and memorable collaboration with her on different research projects about digital image processing, and it was my great honor and pleasure working with her.

I am also grateful to Prof. Jie Liang. I have learned a lot about image and video compression and digital signal processing from his very valuable, up-to-date, and comprehensive courses. He has a very nice personality, and it was my pleasure working with him at the Multimedia Communications Laboratory at SFU.

I am very thankful to Prof. Zhou Wang for accepting to be my external examiner, and taking his valuable time to read my thesis. I am also very grateful to my internal examiner, Prof. Rodney G. Vaughan, for the patience to read my thesis. I like to thank Prof. Andrew Rawicz for chairing my defence.

I feel very privileged to get to know many of my good friends at Multimedia Communications Laboratory at SFU. I am especially grateful to Dr. Yue-meng Chen, Dr. Jing Wang, Dr. Upul Samarawickrama, Ali Amiri, Mahtab Torki, Duncan Chan, Carl Qian, Xiaonan

Ma, Choong-hoon Kwak, Sohail Bahmani, Hossein Khatoonabadi, Homa Eghbali, Victor Mateescu, and Hanieh Khalilian for all the entertainment and caring they provided.

Lastly, and most importantly, I would like to express my great and special gratitude to my lovely parents and family who continuously encouraged and supported me during the difficult times of being away from home. In particular, I would like to dedicate this dissertation to my lovely father who has always been my inspiration.

Contents

List of Tables

List of Figures

List of Symbols

$\mathbf{F}$	A video frame
$\mathbf{X}$	A block or macroblock in the current frame
$\mathbf{X}_0$	The co-located block or macroblock in the previous frame
$\mathbf{X}_i$	The i-th macroblock in the frame
$\mathcal{S}(\mathbf{X})$	The saliency of $\mathbf{X}$
$\mathcal{S}_{gmc}(\mathbf{X})$	The global motion compensated saliency of $\mathbf{X}$
$\mathcal{S}_{spatial}(\mathbf{X})$	The spatial saliency of $\mathbf{X}$
$\mathcal{S}_{temporal}(\mathbf{X})$	The temporal saliency of $\mathbf{X}$
$\mathcal{S}_{motion}(\mathbf{X})$	The motion saliency of $\mathbf{X}$
$\mathcal{N}(\mathbf{X})$	A spatial neighborhood around $\mathbf{X}$
$\mathbf{Z}_\mathbf{X}$	The 2-D DCT of $\mathbf{X}$
$\mathbf{Z}_\mathbf{X}(j,l)$	The (j,l)-th DCT coefficient of $\mathbf{X}$
$\mathbf{Z}_\mathbf{X}^W$	The Wiener-filtered of $\mathbf{Z}_\mathbf{X}$
$H(\omega)$	The transfer function of the Wiener filter in the frequency domain
$S_S(\omega)$	The power spectral density of the signal
$S_V(\omega)$	The power spectral density of the noise
$\mathbf{H}$	The DCT-domain Wiener filter
$\mathbf{H}(j,l)$	The (j,l)-th coefficient of $\mathbf{H}$
$\mathbf{Q}$	The residual block
Q	The quantization step size
QP	The quantization parameter
QP_f	The quantization parameter of frame f
QP_i	The quantization parameter of the i-th macroblock
Q_i	The quantization step size of the i-th macroblock

J	The Lagrangian cost function
ψ	coding mode
D_{MSE}	The MSE distortion
D_{sal}	The saliency distortion
λ_R	The frame-level Lagrange multiplier
R	The rate
$\bar{s}$	The average saliency within the current frame
λ_{R_i}	The Lagrange multiplier of the i-th macroblock
λ_{S_i}	The saliency distrotion weight of the i-th macroblock
λ_S	The general saliency distrotion weight
$\tilde{\mathbf{X}}_i(\psi\|Q_i)$	The macroblock encoded under coding mode ψ with Q_i
λ	The Laplace parameter
Y	The transformed residual
Y_i	The transformed residual of the i-th macroblock
σ_Y	The standard deviation of Y
$\sigma^2_{Y_i}(j,l)$	The variance of the (j,l)-th DCT coefficient of Y_i
$\sigma^2_{r_i}$	The variance of the residual signal of $\mathbf{X}_i$
ρ_i	The correlation coefficient of the residual signal of $\mathbf{X}_i$
$\mathbf{A}(\psi)$	The $N \times N$ transform matrix of coding mode ψ
$\mathbf{K}(\psi)$	The covariance matrix of coding mode ψ
$h_i(j,l)$	The entropy of the (j,l)-th DCT coefficient
$F_{x,y}$	The pixel value at location (x,y) in frame $\mathbf{F}$
$F'_{x,y}$	The pixel value at location (x,y) in encoded frame $\mathbf{F}'$
W	The width of the frame (pixels)
H	The height of the frame (pixels)
$w_{x,y}$	The value of the Gaussian weight function at location (x,y)
σ_x	The width of the Gaussian weight function
σ_y	The height of the Gaussian weight function
$\mathbf{D}$	The down-sampling matrix
w	The width of a spatial window
h	The height of a spatial window
$vec(.)$	The vectorization operator
$\mathbf{I}$	The idenity matrix

$\mathbf{T}$	The thumbnail block
$\mathbf{L}$	A low-pass FIR filter
$\tilde{\mathbf{L}}$	The high-pass complement of $\mathbf{L}$
$\mathbf{R}_k$	The k-th RECAP candidate
K	The total number of RECAP candidates
d	The distance between the current frame and the reference frame
$\mathbf{X}_e$	The extended version of $\mathbf{X}$
$\mathbf{M}$	A $p \times m$ binary matrix
$\mathbf{N}$	A $m \times p$ binary matrix
$\mathbf{N}^t$	The transpose of matrix $\mathbf{N}$
$\mathcal{Z}(.)$	The matrix extension operator
d_s	The down-sampling factor
N_b	The width or height of a block
p	The width or height of a spatial neighborhood
$\zeta(.)$	The complexity operator

List of Acronyms

1-D	One-Dimensional
2AFC	Two Alternative Forced Choice
2-D	Two-Dimensional
AUC	Area Under Curve
AVC	Advanced Video Coding
BD	Bjontegaard Delta
CIF	Common Interchange Format
CRF	Conditional Random Field
CSF	Contrast Sensitivity Function
DBN	Dynamic Bayesian Network
DCT	Discrete Cosine Transform
DFT	Discrete Fourier Transform
DSCQS	Double Stimulus Continuous Quality Scale
EWPSNR	Eye-tracking-weighted Peak Signal to Noise Ratio
FA	FancyOne saliency normalization operator
FBA	Feature Based Attention
FEC	Forward Error Correction
FIT	Feature Integration Theory
FJND	Foveated Just-Noticeable Difference
GBVS	Graph Based Visual Saliency
GMC	Global Motion Compensation
GMC-MV	Global Motion-Compensated Motion Vector
GOP	Group of Pictures
HMM	Hidden Markov Model

HR	High Resolution
HVS	Human Visual System
IB	Itti-Baldi
IKN	Itti-Koch-Niebur
JM	Joint Model reference software
KL	Kullback-Leibler
KLD	Kullback-Leibler Divergence
LR	Low Resolution
MA	MaxNorm saliency normalization operator
MB	Macroblock
MOS	Mean Opinion Score
MSE	Mean Squared Error
MV	Motion Vector
PDF	Probability Density Function
PQFT	Phase Spectrum of Quaternion Fourier Transform
PSNR	Peak Signal to Noise Ratio
QP	Quantization Parameter
RD	Rate-Distortion
RDO	Rate-Distortion Optimization
RECAP	Receiver Error Concealment using Acknowledge Preview
ROI	Region of Interest
ROC	Receiver Operating Characteristic
SAD	Sum of Absolute Differences
SSIM	Structural Similarity Index
SVD	Singular Value Decomposition
SVM	Support Vector Machine
UEP	Unequal Error Protection
VA	Visual Attention
VAGBA	Visual Attention Guided Bit Allocation
VQM	Video Quality Metric
WTA	Winner Take All

Chapter 1

Introduction

1.1 Visual Attention

It is well-known that due to the limited capacity of the brain, only a small amount of visual information that is received at the retina of our eyes can reach the latter processing of the brain and impact our conscious awareness [3]. Visual attention provides a mechanism for selection of particular aspects of a visual scene that are most relevant to our ongoing behaviour while eliminating interference from irrelevant visual data in the background. Perhaps, one of the earliest definitions of attention was provided by William James in 1890 in his textbook "Principles of Psychology" [4]:

> *"Everyone knows what attention is. It is the taking possession by the mind, in clear and vivid form, of one out of what seem several simultaneously possible objects or trains of thought. Focalization, concentration, of consciousness are of its essence. It implies withdrawal from some things in order to deal effectively with others."*

Over the last decades, visual attention (VA) has been studied intensely, and research has been conducted to understand the deployment mechanisms of visual attention. According to the current knowledge, the deployment of visual attention is believed to be driven by "visual saliency," that is, the characteristics of visual patterns or stimuli, such as a red flower in a green grass field, that makes them stand out from their surroundings and draw our attention in an automatic and rapid manner. Various computational models of visual attention have then been developed based on this belief for different applications such as robotics, navigation, image and video processing, and so on [5], [6]. Such computational

models of human visual attention are commonly referred to as visual saliency models, and their goal is to predict where people are likely to look in a visual scene.

The perceptual coding of video using visual saliency models has been recently recognized as an increasingly promising approach to achieve high-performance video compression [5]. The rationale behind most of the existing saliency-based video coding methods is to encode a small area around the predicted gaze locations with higher quality compared to other less visually important or interesting regions. Such a spatial prioritization is supported by the fact that only a small region of several degrees of visual angle (i.e., the fovea) around the center of gaze is perceived with high spatial resolution due to the highly nonuniform distribution of photoreceptors on the human retina. Therefore, the idea is that it may not be necessary to encode each video frame with a uniform quality because human observers will perceive only a very small portion of each frame around their gaze locations, which we may call regions-of-interest (ROIs). Hence, based on these principles, ROIs should be encoded with a higher quality compared to the rest of the frame. The hope is that one may save bits while achieving the same subjective quality as a conventional approach that grants the same quality across the frame.

In practice, the encoding prioritization can be performed in several ways. In one popular approach, the compression ratio is decreased in ROI parts of the frame whereas it is increased in non-ROI parts. Using this approach, the overall compressed video size may decrease as ROI parts of the frame usually constitute a small portion of the frame, so the extra bits spent on their encoding are more than offset by the savings in non-ROI parts. Another approach is to apply a so-called "foveation filter" [5] to the video content before the encoding process. The foveation filter spatially blurs the video frame, increasingly with distance from ROI parts of the frame. Hence, due to the loss of higher spatial frequencies in non-ROI parts after applying the foveation filter, non-ROI parts take fewer bits to encode, and so bit rate savings can be achieved. In another, more sophisticated approach [7], the prioritization may be performed by a progressive or scalable scheme, for example, by delivering priority regions first or continuously scaling the video quality depending on a given transmission bandwidth or bit budget. Such encoding schemes are generally referred to as ROI-based video coding methods.

Although ROI-based video coding methods can achieve high compression, the selection of ROI parts remains an open and challenging problem. In recent years, several advances have been achieved to tackle this problem with two approaches. The first approach involves the

use of an eye-tracking device to interactively record eye gaze position of a human observer on the receiving side in order to find the ROI in real time [8], [9]. A foveation filter is then applied on the source video signal on the transmitting side, taking the detected ROI into account, and the foveated video is transmitted to the receiver. In a variant of this approach, gaze locations of a number of observers watching the same video are measured by an eye-tracking device off-line, and their union is treated as the ROI [10]. Although this approach can provide a good estimate of the ROI, it is neither generic nor cost-effective. It is very time consuming as it requires an eye-tracking setup and collecting and training various observers for every video to be compressed.

Rather than deducing ROI based on measurement, the second approach instead relies on visual saliency models for finding ROI [5]. Here, ROIs are declared to be the parts of the frame where viewers are most likely to focus their visual attention, according to the employed saliency model. This general-purpose and automatic approach has the advantage that it does not require human interaction, and so it is practical and cost-effective. The downside, of course, is that it is only as accurate as the saliency model it relies on.

ROI-based processing can also be employed in the context of video transmission to combat the effects of transmission channel errors. For instance, ROI parts of the frame can be protected heavily (e.g., by using stronger channel codes) than non-ROI parts of the frame [11], so that in the case of channel errors or losses, important parts of the frame can still be decoded correctly. In this case, also, ROI could be detected either based on direct eye-tracking measurement or based on visual saliency models.

Despite the increasing popularity of saliency-based video compression and transmission methods, such approaches are still immature. Integrating a complex saliency model within another video processing task can be cumbersome. The main goal of this dissertation is to develop novel methods for better utilization of visual saliency in video compression and transmission. For this purpose, we first develop an efficient approximation to a popular visual saliency model that partially operates in the transform domain, and reuses some of the data that is normally present in video compression. This reduces the computational cost of estimating visual saliency and makes it easier to incorporate into various video processing systems. We then utilize this approximation within a ROI-based framework for efficient video compression and transmission.

1.2 Contributions

The main contributions of this research are as follows.

1.2.1 An eye-tracking database for a number of standard video sequences

The best way to test the accuracy of visual saliency models is to compare their predictions with real eye-tracking data. Such data can also be used to evaluate various saliency-based video processing algorithms. However, eye-tracking devices are still fairly expensive and are not easily accessible to most researchers. To facilitate the development and testing of novel perceptually-motivated algorithms and models of visual attention, we developed a publicly available database of eye-tracking data, collected on a set of standard video sequences that are frequently used in video compression, processing, and transmission simulations. A unique feature of this database is that it contains eye-tracking data for both the first and second viewings of the sequence. The dataset is described in [12], and will be discussed in Chapter 3.

1.2.2 Computationally-efficient visual saliency models

Among the existing saliency models, the Itti-Koch-Niebur (IKN) saliency model [2] is the most well-known and widely-used model. However, this bottom-up model of visual attention is very complex as it requires multiresolution analysis of the input image or video in in various feature channels such as intensity, color, and orientation. In this dissertation, we present two computationally-efficient saliency models inspired by the IKN model. Both models are described in Chapter 4.

The first proposed model is a convex approximation to the IKN saliency model. It consists of two parts: spatial and temporal. The spatial part can be used to estimate saliency in static images, whereas the temporal part in conjunction with the spatial part can be utilized to estimate saliency in video. The model estimates saliency using the signal energy in the Discrete Cosine Transform (DCT) domain, which makes it useful for saliency estimation in DCT-based image and video processing tasks. This model was first introduced in [13], and its application to video error concealment will be described in Chapter 6. Although this model is slightly less accurate than the IKN model, it has several practical advantages. First, its computational complexity is much lower than that of the IKN model, making it attractive for real time implementation. Second, it is convex in the input data.

This means that when the saliency estimate produced by this model is linearly combined with other convex measures (e.g., mean squared error), it results in a convex function, which can lead to convex optimization formulations (and corresponding efficient solutions) in various image and video processing tasks. One example is given in Chapter 6, where this approximation is used to make a saliency-cognizant error concealment problem convex, which in turn leads to an efficient solution.

The second proposed saliency model uses the convex approximation to the spatial IKN model mentioned above, but improves the temporal saliency estimation via global motion compensation [14]. We refer to this method as Global Motion-Compensated (GMC) saliency estimation. Overall, this method is not convex, but is more accurate than the IKN model on certain sequences with camera motion. This method was first introduced in [15], and will be used in saliency-aware video compression in Chapter 5.

1.2.3 Saliency-aware video compression

As stated earlier, in ROI-based video coding, ROI parts of the frame are encoded with higher quality than non-ROI parts. At low bit rates, such encoding may produce attention-grabbing coding artifacts, which may draw viewers attention away from ROI, thereby degrading visual quality. In this dissertation, we present a saliency-aware video compression method for ROI-based video coding. The proposed method aims at reducing salient coding artifacts in non-ROI parts of the frame in order to keep users attention on ROI. Further, the method allows saliency to increase in high quality parts of the frame, and allows saliency to reduce in non-ROI parts. The ideas behind this approach are described in [16] and [15], and will be discussed in Chapter 5.

1.2.4 Saliency-cognizant video error concealment

Visual saliency can be an effective tool in dealing with errors and losses in video transmission, and hiding their effects from the viewers. In this dissertation, we add a low-saliency prior to the under-determined problem of error concealment as a regularization term. There are multiple reasons for doing so. First, in ROI-based video transmission, low-saliency prior is likely the correct side information for the lost block and helps the client to identify the correct replacement block for concealment. Second, in the event that a perfectly matched block cannot be identified, the low-saliency prior reduces viewers' visual attention on the

loss-stricken region, resulting in higher overall subjective quality. In a way, the low-saliency prior tries to make error concealment live up to its name by attempting to hide damaged blocks from viewers attention. It is the low-saliency prior that puts *concealment* into error concealment – the rest is just interpolation. To the best of our knowledge, our work is the first to apply saliency analysis for error concealment in video transmission. This approach has been described in [1] and [13], and will be discussed in Chapter 6.

1.2.5 Scholarly publications

My research efforts during my Ph.D. program have resulted in the following scholarly publications. Please note that the material in this dissertation is only related to several of the most recent ones, specifically journal papers 1-3, and conference papers 3 and 5.

Journal Papers:

1. H. Hadizadeh and I. V. Bajić, "Saliency-aware video compression," submitted to *IEEE Trans. Image Processing*, Feb. 2013.

2. H. Hadizadeh, I. V. Bajić, and G. Cheung, "Video error concealment using a computation-efficient low saliency prior," submitted to *IEEE Trans. Multimedia,* Dec. 2012. Currently under revision. (**Invited Paper**)

3. H. Hadizadeh, M. J. Enriquez, and I. V. Bajić, "Eye-tracking database for a set of standard video sequences," *IEEE Trans. Image Processing*, vol. 21, no. 2, Feb. 2012.

4. H. Hadizadeh and I. V. Bajić, "Rate-distortion optimized pixel-based motion vector concatenation for reference picture selection," *IEEE Trans. Circuits Syst. Video Technol.*, vol. 21, no. 8, pp. 1139-1151, Aug. 2011. (Among top 25 most download papers from this journal in August 2011)

5. H. Hadizadeh and I. V. Bajić, "Burst loss resilient packetization of video," *IEEE Trans. Image Processing,* vol. 20, no. 11, pp. 3195-3206, Nov. 2011.

Conference Papers:

1. V. A. Mateescu, H. Hadizadeh, and I. V. Bajić, "Evaluation of several visual saliency models in terms of gaze prediction accuracy on video," *Proc. IEEE Globecom'12 Workshop: QoEMC,* pp. 1304-1308, Anaheim, CA, Dec. 2012.

2. H. Hadizadeh, M. Fatourechi, and I. V. Bajić, "An automatic lyrics recognition system for digital videos," presented at *IEEE MMSP'12* (On-going Work Track), Banff, AB, Sep. 2012.

3. H. Hadizadeh, I. V. Bajić, and G. Cheung, "Saliency-cognizant error concealment in loss-corrupted streaming video," *Proc. IEEE ICME'12*, pp. 73-78, Melbourne, Australia, Jul. 2012. (**Best Paper Runner-up**)

4. H. Hadizadeh, I. V. Bajić, P. Saeedi, and S. Daly, "Good-looking green images," *Proc. IEEE ICIP'11*, pp. 3177-3180, Brussels, Belgium, Sep. 2011.

5. H. Hadizadeh and I. V. Bajić, "Saliency-preserving video compression," presented at *IEEE AVCC*, in conjunction with *IEEE ICME'11*, Barcelona, Spain, Jul. 2011.

6. H. Hadizadeh and I. V. Bajić, "Pixel-based motion vector concatenation for reference picture selection," *Proc. IEEE ICME'10*, pp. 209-213, Singapore, July 2010.

7. H. Hadizadeh, S. Muhaidat, and I. V. Bajić, "Impact of imperfect channel estimation on the performance of inter-vehicular cooperative networks," presented at *25th Queen's Biennial Symposium on Communications (QBSC'10)*, Kingston, ON, Canada, May 2010.

8. H. Hadizadeh and I. V. Bajić, "Burst loss resilient packetization of video," *Proc. IEEE ICC'10*, Cape Town, South Africa, May 2010.

9. H. Hadizadeh and I. V. Bajić, "NAL-SIM: An interactive simulator for H.264/AVC video coding and transmission," presented at *Proc. IEEE CCNC'10*, Las Vegas, NV, USA, Jan. 2010.

1.3 Organization

This dissertation is organized as follows. In Chapter 2, we present a brief description of the concept of visual attention and its deployment mechanisms. We also present a survey of several existing computational models of visual attention. In particular, we briefly describe two popular saliency models, the Itti-Koch-Neibur (IKN) model [2] and the Itti-Baldi (IB) model [17]. In Chapter 3, we present our eye-tracking database for a number of standard video sequences. Two novel computationally-efficient visual saliency models are presented

in Chapter 4. Our proposed saliency-aware video compression method is presented and evaluated in Chapter 5. The proposed saliency-cognizant error concealment method for video streaming is described in Chapter 6. Finally, the conclusions and future directions are given in Chapter 7.

Chapter 2

Visual Attention and Its Computational Models

It is known that the brain in primates has a "massively parallel" computational structure [3]. However, similar to any physical system, the processing and computational resources of the brain are limited. Every time that we open our eyes to the world, we encounter an overwhelming amount of visual information. It has been estimated that the amount of visual information coming to our visual system is on the order of 10^8 bits per second, which far exceeds the processing power and computational capacity of our brain [3]. Nevertheless, we are able to experience an almost effortless understanding of our visual world. This requires separating relevant information from irrelevant data in a preferential and serial manner. Such a process is operationalized by the mechanisms of "visual attention" [3, 18], which allows us to break down the daunting problem of visual scene understanding into a rapid series of computationally less demanding, localized visual analysis problems [19]. According to [20], attention is the cognitive process of selectively concentrating on one aspect of the environment while ignoring other irrelevant things. Attention has also been referred to as the allocation of processing resources [20]. Hence, visual attention optimizes the use of our visual system's limited resources for gathering and processing the most relevant information in a complex visual environment. In other words, visual attention turns our looking into seeing [18].

The topic of visual attention is vast, and since 1980, the concept of visual attention has been studied in several thousands of scientific papers with an increasingly growing rate [18],

[21], [22], [23], [3]. According to a recent review on visual attention [18], there are three main types of visual attention: (1) spatial attention, which can be either overt (i.e., when an observer moves his/her eyes to focus on a specific region in the visual scene) or covert (i.e., when a person mentally focuses on another sensory stimuli different from the stimuli at his/her current fixation); (2) feature-based-attention (FBA), which can be deployed covertly to specific aspects (e.g., color, orientation or motion direction) of objects in the environment, regardless of their location; (3) object-based attention in which attention is influenced or guided by a specific object structure or the relevance between different objects in a visual scene. At any given time, these three types of visual attention can co-exist [18]. For instance, when waiting to meet a friend in a restaurant, we may direct our spatial attention to the entrance door of the restaurant (i.e., where our friend is likely to appear), and deploy our FBA to red objects, assuming that our friend is wearing a red shirt [18].

2.1 Mechanisms of attentional deployment

Interesting questions related to the concept of visual attention are how the selection of one particular spatial location or object in a cluttered visual scene is performed, or where in a visual scene, the visual attention is deployed? In other words, if our brain can process only one region or object at a time, then how do we select the target of our attention? Many studies have been conducted for finding answers to these questions. Much evidence has been accumulated in favor of the following two principal beliefs about the mechanisms of visual attention deployment: [3],[24],[25],[26], [6]

1. There is a "bottom-up," fast, primitive, and stimulus-driven mechanism that biases the observer towards selecting stimuli based on their "visual saliency." Here, "visual saliency" means how much a certain stimulus (e.g., a region or object) is distinct from its surroundings in terms of visual attributes such as color, intensity, and orientation, so that it stands out from its surroundings. According to this scene-driven mechanism, visual attention is attracted towards visually salient locations in a seemingly effortless and automatic manner. Based on this mechanism, a red flower in a green grass field is visually salient due to its high color contrast, drawing visual attention towards itself. The terms "salient" and "visual saliency" are often utilized in the context of bottom-up modeling of visual attention [6].

2. A "top-down," slow, voluntary and user-driven mechanism with variable selection criteria that intentionally directs the visual attention towards specific locations or objects in the visual scene, regardless of their visual saliency. Such a task-dependent and expectation-driven mechanism can modulate or even sometimes override the bottom-up deployment of visual attention. For instance, if we want to find our misplaced car keys, those keys (i.e., their color, shape, etc.) become the primary drivers of our attention; other object in the room would have a hard time drawing our attention in this case.

The bottom-up control of visual attention relies on the fact that the brain does not process all parts of a visual scene equally well, but instead provides a selective prioritization with strong neural responses to a few parts of the scene, and poor responses to everything else. Several studies provide direct support for the idea that different visual stimuli in a visual scene compete for activity to draw visual attention [27], [28], [3], [19]. Those parts that are very different from their surroundings can elicit a strong neural response, and can draw visual attention to themselves. They are said to be salient. Directing attention to other, non-salient parts, is thought to require voluntary effort, which can be employed by the top-down mechanism of visual attention [3].

The top-down cues are often determined by cognitive phenomena such as knowledge, expectations, reward, tasks, and goals [6]. One of the most popular examples for showing the effect of the top-down guidance of visual attention on the eye movements is from the following experiment described in [29]. Subjects were asked to watch a scene showing a room with a family and an unexpected visitor entering the room. Some subjects were allowed to freely watch the scene, while others were asked questions such as "what are the ages of the people in the room?" or "estimate the material circumstances of the family." The results of this experiment showed that the eye movements were considerably different under each question, which suggests that a task can significantly affect the deployment of attention. Several researchers have studied the role of the task in the deployment of visual attention in natural environments, for tasks like driving, sandwich making, playing cricket, and walking [30], [31], [32].

2.2 Computational models of visual attention

In the past 25 years, modeling visual attention has been a very active research area. Various computational models of human visual attention (a.k.a. "saliency models") have been proposed in both the computer vision community and biological vision and neuroscience community. The main goal of such models is to predict the target of visual attention in a given visual scene, for example in a given image or video. In other words, their goal is to predict where people are likely to look.

In the computer vision community, the design and development of the so-called "saliency detectors" or "interest point detectors" has been a significant research objective in the past decades. Various saliency detectors have been proposed and adopted in many computer vision applications such as object tracking and recognition, robotics, image and video compression, advertising, etc. The majority of such models are closely related to object detection and feature extraction methods. Broadly speaking, the existing saliency detectors proposed in the computer vision literature can be classified into the following three classes:

- In the first class, the saliency detection problem is formulated as the detection of specific visual attributes such as edges, corners, contours, blobs, structure-from-motion, and so on [33], [34]. A prominent advantage of such bottom-up saliency detectors is that they can be defined with an explicit mathematical formulation, and can be implemented using efficient computational methods. A major drawback of such detectors, however, is that they cannot be generalized well for object recognition problems, and so they cannot provide useful information for the desired recognition task at hand. For instance, consider a white egg on top of a tree branch. A saliency detector that uses corner information will show a strong response to the highly textured tree branch, but not to the plain egg, even though the egg may be salient.

- In the second class, the saliency is defined as a measure of "image complexity." Several image complexity measures have been proposed in this context. For instance, in [35], the saliency is defined as the variance of Gabor filter responses in different orientation and frequency bands. In [36], the absolute values of 2-D wavelet coefficients are used a measure of saliency. In [37], the entropy of local intensity histograms in an image is used for saliency detection. The main advantage of such models is that they can detect several low-level image features in a unified and generic manner. However,

similar to the first class, their main drawback is that they cannot directly provide useful information for the recognition task of interest.

- In the third class, the saliency detection problem is formulated as an object detection and recognition problem. Hence, the models in this class can be considered as top-down saliency detectors. Examples of such models include those proposed in [38], [39], [40]. Several object detection approaches can be utilized by the models in this class. For instance, the deformable part model proposed in [41] and the attentional cascade of Viola and Jones [42] can be employed to achieve a very high detection accuracy for several objects such as cars, faces, and persons. The main advantage of such models is their superior performance for salient object detection, especially in cluttered scenes. However, by their very nature, such models are application-specific and hence have a limited application scope.

The main objection to the saliency detection models proposed in the computer vision literature is that they are application-oriented and seldom have a connection to the biological architecture of the human visual system. The main goal of such models is not to explain attentional behavior. Instead, the goal is usually to make a computer perform a vision-related task with the same end result as a human, regardless of whether or not the intermediate processing is performed in the same way as in human vision. While this is perfectly appropriate for application purposes, methods that shed light on the actual principles of human vision may have greater scientific value.

In the biological vision community, both the neurophysiological and psychophysical properties of visual attention have been extensively studied, and several computational models of human visual attention have been proposed. Most such models emphasize biological plausibility, and their goal is to replicate what is known about the biology and the neural architecture of the human visual attention mechanisms. With a few exceptions [29], [43], the majority of such models have been proposed for the bottom-up mechanism of visual attention. The reason is that the bottom-up mechanism of visual attention is better understood due to its reliance on low-level processing tasks, which are easier to measure and study. Meanwhile, the top-down attention relies on higher-level tasks in the brain that are still not well understood. Moreover, as we mentioned earlier, top-down cues are often related to tasks, expectations, rewards, and current goals. Hence, they are application-specific, related to context and prior knowledge, and therefore difficult to model.

The basis of many of existing attention models is the well-known "Feature Integration Theory" (FIT) proposed by Treisman and Gelade [44]. This theory postulates which visual features are important and how they are combined together to direct visual attention in search tasks [6]. More explicitly, FIT states that "different features are registered early, automatically and in parallel across the visual field, while objects are identified separately and only at a later stage, which requires focused attention" [44]. Based on FIT, Koch and Ullman [45] proposed a computational model to combine these features, and they introduced the concept of a two-dimensional topographical "master saliency map" that represents the saliency of various regions and objects in a given visual scene. They also proposed a winner-take-all (WTA) neural network that selects the most salient locations in a given saliency map. Competition among different neurons in this network results in a single winning location that corresponds to the most salient region in the scene. The next most salient region in the scene can be found by inhibition of the current most salient object using a specific inhibition of return (IOR) operator. Using this mechanism, the system can predict the next focus of visual attention in a serial fashion. Several systems were proposed to implement the Koch and Ullman model for computing the saliency maps of digital static images [46], [47]. The first comprehensive implementation of the model, however, was developed by Itti *et al.* [2]. This system was designed in a biologically plausible manner in the sense that it attempts to replicate the biological and neural processes involved in human vision. Itti *et al.* applied their attention model to synthetic and natural scenes, and they showed that their model's predictions have a high correlation with real eye-tracking data in free-viewing tasks, which verifies the effectiveness of their method for saliency detection in digital images [2].

Although the majority of existing models of visual attention have been developed for static images, there also exist several models for saliency detection in video [5], [48], [49], [50], [6]. Almost all such models consist of a spatial component and a temporal component, which distinguishes them from the purely spatial models for static images. Some of the saliency detection methods for video use a motion and a flicker channel for temporal saliency detection [5]. Other models attempt to capture the spatio-temporal features of a video by more sophisticated methods. For instance, the method in [51] computes the temporal saliency based on the motion contrast obtained from the homographic transformation between successive video frames. In [52], the temporal saliency is estimated in an irregularity detection framework by comparing the spatio-temporal patches of the video with a

learned dataset of expected spatio-temporal patches.

Following the seminal model by Itti *et al.* [2], many other bottom-up saliency models were proposed in the literature based on FIT. All such models of visual attention share three common components. The first component is the extraction of various low-level visual features from a given input image or video signal. Inspired by the processing mechanism of neurons in the primary visual cortex (V1) of the human brain and the feature integration theory, these features include various simple visual attributes such as intensity or luminance contrast, color opponency, orientation and motion [2]. The second common component is the so-called "center-surround" mechanism by which contrast features are computed in different feature channels [2], [17], [53]. The center-surround mechanism is supported by the neural responses of the visual receptive fields of neurons in the lateral geniculate nucleus (LGN) [54] and V1 cortex of the human brain. Typical visual neurons are most sensitive in a small region of the visual field (the center), and inhibit the neural response to stimuli presented in a broader region concentric with the center (the surround) [2]. Hence, such architectures can detect locations that stand out from their surroundings. The third component is the computation of a "master saliency map" by which the saliency of different locations in a visual scene can be estimated.

According to a recent survey of visual attention models presented in [6], the existing computational models of visual attention can be classified into the following general categories based their mechanism of computing saliency:

- Cognitive Models: These models have been built based on psychological and neurophysiological findings and cognitive concepts. Many of the existing attention models fall within this category, especially those that were developed in the biological and neuroscience community. Notable (popular) models from this category are the Itti-Koch-Niebur (IKN) model [2] and the model proposed by Le Meur *et al.* [55]. The IKN model is the most popular and widely-cited attention model, and it has been the basis for the development and benchmarking of many other attention models. Hence, it can be considered as the representative bottom-up attention model. Due to its importance, we briefly describe it in Section 2.2.1. The model proposed by Le Meur *et al.* [55] is also a bottom-up model, and shares some common features with the IKN model. The main difference between these two models is that the model of Le Meur *et al.* uses several psychophysical properties of the human visual system (HVS) [56] such

as the luma and chroma contrast sensitivity functions (CSFs), multi-band frequency decomposition, visual masking, and center-surround computations. It also uses the temporal information so that it can be utilized for saliency detection in video as well. In other words, the model in [55] is a spatio-temporal saliency model while the original IKN model [2] is a spatial saliency model. However, in [5], several temporal features such as motion and flicker were added to the IKN model, which enabled its use for saliency detection in video.

- Bayesian Models: The models in this class are based on the Bayes' theorem to capture subjective aspects of sensory information under prior knowledge. More specifically, in these models, the sensory information (e.g., detected features) are combined with prior knowledge (e.g., scene context) in a probabilistic manner using the Bayes' rule to detect a salient region in a visual scene [6]. Several models within this category are [17], [57], [58], [59], [60], [61]. A representative model in this category is the Itti-Baldi (IB) model proposed in [17]. In this model, a Bayesian definition of surprise was presented. In their definition, a surprising stimulus is the one that significantly alters the prior beliefs of a Bayesian observer. To quantify the amount of surprise, they used the Kullback-Leibler (KL) divergence [62] between posterior and prior beliefs. In Section 2.2.2, we briefly describe the IB model.

- Decision Theoretic Models: The models in this category are based on the "discriminant saliency hypothesis" [63], which states that saliency is a discriminant process, and all saliency processes are optimal in a decision-theoretic sense, i.e., with minimum probability of decision error. Under this framework, the saliency of each location in the visual field is considered as the discriminant power of the image features with respect to a classification problem that opposes a class of interest (i.e., the target) to all other visual classes. Notable (popular) model in this category is the model proposed by Gao and Vasconcelos [63].

- Information Theoretic Models: These models are developed based on the hypothesis that perceptual systems are designed to maximize information collected from the environment, so that only the most relevant and informative parts of the visual field are selected and the rest is discarded [6]. The idea behind such models is supported by the biological evidence that the primate visual system is built on the principle of establishing a sparse representation of image statistics [53]. The notable (popular) model

in this category is the model proposed by Bruce and Tsotsos [53]. Their bottom-up model is based on Shannon's self-information measure for computing saliency of image regions. In their formulation, saliency of a local image region is the information that region conveys relative to its surroundings, based on the probability density functions of various RGB features.

- Graphical Models: The attention models in this category consider eye movements as stochastic time series. Since there are hidden variables influencing the eye movements, graphical networks [64] such as Hidden Markov Models (HMM), Dynamic Bayesian Networks (DBN), and Conditional Random Fields (CRF) have been used by such models to predict eye fixations or movements. The well-known model in this category is the Graph-Based Visual Saliency (GBVS) model proposed by Harel *et al.* [38]. In this model, similar to the IKN model, several feature maps are first created at different scales. A fully-connected graph is then created over all grid locations of each feature map. The weight between each pair of nodes in each graph is computed by the similarity of the feature values of the two nodes, as well as their spatial distance. The resulting graphs are then considered as Markov chains, and a random walker [64] is used to find the equilibrium distribution of each graph. The obtained equilibrium distributions are used to construct the master saliency map for a given image.

- Spectral Analysis Models: In these attention models, saliency is estimated in the spectral (frequency) domain instead of the spatial (pixel) domain. The popular models in this category are the spectral residual saliency model proposed by Hou and Zhang [65] and the "Phase Spectrum of Quaternion Fourier Transform" (PQFT) model proposed by Guo and Zhang [48]. The spectral residual saliency model in [65] was designed based on the idea that statistical singularities in the amplitude of the Fourier spectrum of an image may be responsible for salient regions. Hence, by finding such regions, one can construct a saliency map of the scene. In the PQFT method, it was observed that the phase spectrum of the Fourier transform can also be utilized for saliency prediction. Based on this idea, a quaternion representation of a video was proposed in [48], and it was used for spatio-temporal saliency detection.

- Pattern Classification Models: The models in this category employ machine learning approaches for discovering the relation between image features and measured eye fixations. A popular model in this category is the model proposed by Kienzle *et al.* [66], in

which a nonparametric bottom-up approach was proposed for saliency estimation by learning attention directly from human eye fixation data. In their method, a support vector machine (SVM) [64] was employed to learn the relation between local image intensities and real eye fixation data. The results were a set of spatial filters similar to center-surround filters, that can be used for saliency estimation in natural images. For video, they proposed to learn a set of temporal filters similar to their spatial filters.

A recent survey of various attention models can be found in [6]. In the sequel, we briefly describe two popular attention models: The IKN model [2] and the Itti-Baldi (IB) model [17].

2.2.1 The Itti-Koch-Niebur model

Among the existing bottom-up computational models of visual attention, the Itti-Koch-Niebur (IKN) model [2] is one of the most well-known and widely cited. In this biologically plausible model, the visual saliency of various regions is predicted by analyzing the input image through a number of pre-attentive independent feature channels, each locally sensitive to a specific low-level visual attribute, such as local opponent color contrast, intensity contrast, and orientation contrast. More specifically, nine spatial scales are created using dyadic Gaussian pyramids, which progressively low-pass filter and down-sample the input image, yielding an image-size-reduction factor ranging from 1:1 (scale zero) to 1:256 (scale eight) in eight octaves [2].

The contrast in each feature channel is then computed using a "center-surround" mechanism, which is implemented as the difference between fine and coarse scales: the center is a pixel at scale $c \in \{2, 3, 4\}$, and the surround is the corresponding pixel at scale $s = c + d$, with $d \in \{3, 4\}$. The "center-surround" mechanism simulates the visual receptive fields in the retina, lateral geniculate nucleus (LGN), and primary visual cortex [56], [2]. Such a mechanism is sensitive to local spatial discontinuities. Therefore, it can be used to detect locations which stand out from their surroundings. The across-scale difference between two levels of the pyramid is obtained by interpolation to the finer scale and point-by-point subtraction. The obtained contrast (feature) maps are then combined across scales through a non-linear normalization operator to create a "conspicuity map" for each feature channel. The normalization operator globally promotes maps with few strong peaks of activity, while

globally suppressing maps that contain numerous comparable peaks [2]. Such a normalization operator can be supported biologically as it simulates the operation of cortical lateral inhibition mechanism in the visual cortex [2], [56].

The conspicuity maps are then resized to level 4, and combined together via the same normalization operator to generate a "master saliency map" whose pixel values predict saliency. The maximum of the obtained master saliency map is considered as the most salient location, and determines the (most likely) focus of attention (FOA). The next gaze location can be predicted by inhibiting the current gaze location through a specific "inhibition of return" process [3], [2], which is implemented in the model by a biologically-plausible 2D "winner-take-all" (WTA) neural network [2], [3].

A motion and flicker channels were added to the IKN model in [67] to make it applicable to video. The flicker channel is created by building a Gaussian pyramid on the absolute luminance difference between the current frame and the previous frame. Motion is computed from spatially-shifted differences between intensity pyramids from the current and previous frame [67]. The same center-surround mechanism that is used for the intensity, color, and orientation channels is used for computing the motion and flicker conspicuity maps, which are then combined with spatial conspicuity maps into the final saliency map. Fig. 2.1 shows a schematic diagram of the IKN model.

2.2.2 The Itti-Baldi model

In [17], Itti and Baldi proposed a bottom-up model of visual attention based on the concept of "Bayesian Surprise." They argued that human attention is directed towards "surprising locations." They presented a principled definition of "surprise," and developed a computational model of visual attention in a Bayesian framework, which we shall call the Itti-Baldi (IB) model. Based on their definition, surprise is strong when a new observation substantially changes the previous beliefs of a Bayesian learner about the world. This is encountered when the distribution of posterior beliefs of the learner highly differs from its prior distributions. In their proposed framework, the amount of surprise is quantified by the Kullback-Leibler Divergence (KLD) [62] between the posterior and prior distributions of beliefs of the Bayesian learner.

The IB model retains the same feature channels of the IKN model, and attaches a surprise detector to each location of each feature channel. Surprise detectors compute both temporal surprise and spatial surprise, and they estimate a total spatio-temporal surprise

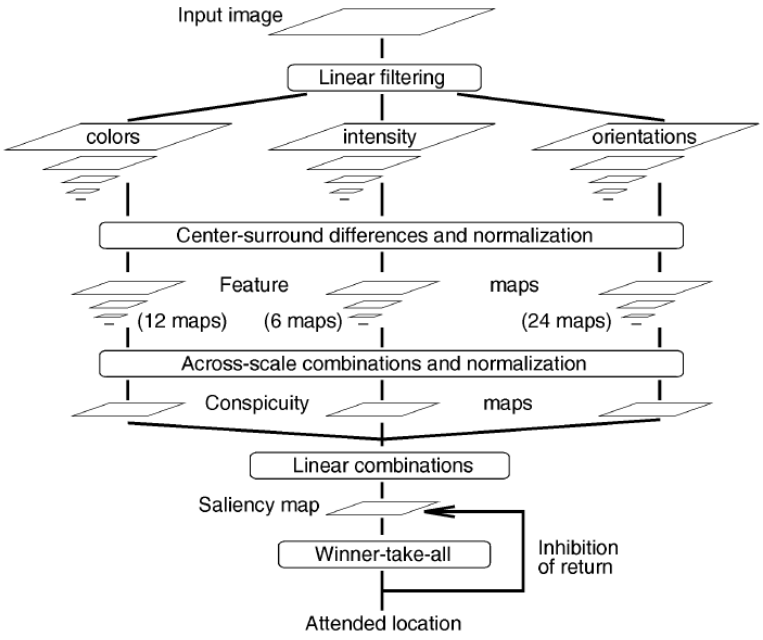

Figure 2.1: A schematic diagram of the IKN model [2].

value, which is computed by summing the spatial and temporal surprise values. It is assumed that surprise sums across feature channels, so that a location may be surprising by its color, motion, orientation, and so on. This results in the final surprise map for a given visual scene. Since the surprise is taken as a measure of saliency, the surprise map is the final master saliency map of this model.

Chapter 3

Eye-Tracking Data

As mentioned in Chapter 2, in the literature, several computational models of visual attention (VA) have been developed to predict gaze locations in digital images and video. Although the current VA models provide an easy and cost-effective way for gaze prediction, they are still imperfect. One must realize that human attention prediction is still an open and challenging problem. Ideally, the most accurate approach to find actual gaze locations is to use a gaze-tracking (aka. eye-tracking) device. In a typical gaze-tracking session, the gaze locations of a human observer are recorded when watching a given image or video clip using a remote screen-mounted or a head-mounted eye-tracking system. However, eye-trackers are still fairly expensive, and are not easily accessible to most researchers. This has intensified the need for eye-tracking datasets. In the past few years, several research groups have provided eye-tracking data for various image collections and videos. A survey of the existing eye-tracking datasets is presented in Section 3.1.

Over the past two decades, a set of "standard" video sequences (for example, *Foreman*, *Flower Garden*, etc.) have been frequently used by many researchers in the field of video compression, processing, and quality assessment. Given the growing popularity of VA-based video compression and quality assessment methods, the need for an eye-tracking database for these standard sequences is becoming apparent. Although there are several existing eye-tracking datasets mentioned in the literature, until the publication of our dataset in [12], there was no publicly available eye-tracking data for the standard sequences mentioned above.

In this chapter, we present our dataset from [12], which is a publicly available, free, on-line database of gaze-tracking data collected on a set of standard video sequences. The

database includes twelve uncompressed YUV (one luma channel, Y, and two chroma channels, U and V) video sequences in CIF (Common Intermediate Format, 352×288) resolution with their corresponding eye-tracking data. To generate the eye-tracking data, the sequences were presented to 15 non-expert subjects two times, and their gaze fixation points were recorded for each frame of each of the 12 selected video sequences using a head-mounted eye-tracking device. The recorded gaze locations provide subjects' gaze shifts caused by subjects' overt visual attention in both the first and the second viewing. We present an analysis of the congruency of the first and second viewing for each sequence. We also compare the accuracy of two well-known visual attention models, the Itti-Koch-Niebur (IKN) model [2] and the Itti-Baldi (IB) model [17], [57], [58], on the obtained eye-tracking data. The dataset can be utilized for various applications including psychovisual video compression, perceptual video quality assessment, and attention prediction purposes.

This chapter is organized as follows. Section 3.1 presents an overview of existing image and video eye-tracking datasets. Section 3.2 describes our dataset [12] for "standard" sequences. Some results obtained using the dataset are presented in Section 3.3, followed by conclusions in Section 3.4.

3.1 Existing eye-tracking data sets

In recent years, several eye-tracking datasets for images and videos have been developed and made publicly available by various research groups. In this section, we present a brief overview of such datasets.

3.1.1 Existing eye-tracking datasets for static images

In [68], an eye-tracking dataset of 120 static images of resolution 682×512 was provided. In this dataset, the eye fixations of 20 subjects were recorded in a free-viewing task. The images show indoor and outdoor scenes. The viewing distance was fixed at 75 cm, and each image was presented for 4 seconds with a 2-second gray mask in between. In [69], the eye-fixation data of 15 subjects on 1003 RGB indoor and outdoor images of resolution 1024×768 was provided. There were 779 landscape images and 228 portrait images in this dataset. The viewing distance was fixed at 48 cm, and each image was displayed for 3 seconds. In [70], the eye-tracking data of 7 subjects of 250 RGB images of resolution 1024×768 was provided. The viewing distance was fixed at 80 cm. The subjects were involved in three different tasks

including a free-viewing task, searching for a specific object (e.g., a face, a banana), and an image recognition memory task in which subjects were asked to answer whether or not they have seen the image before. In [66], the gaze data of 14 subjects on 200 RGB images of resolution 1024×768 was provided. The viewing distance was fixed at 60 cm, and each image was presented for 3 seconds. A comprehensive survey of the existing eye-tracking datasets for static images can be found in [6].

3.1.2 Existing eye-tracking datasets for video

There are also several existing eye-tracking datasets for video. For instance, in [55], an eye-tracking dataset of 7 CIF (352×288) video clips in a free-viewing task was provided. The clips were 4.5 to 33.8 seconds long, and they contained faces, sport events, logos, landscapes, and instructions. In total, there were about 2451 video frames in this dataset. For each clip, the data from 17-27 subjects is provided. A 50 Hz eye-tracker was utilized to record the eye fixations in this dataset. The viewing distance for the subjects was about 81 cm.

In [50], an eye-tracking dataset of 53 short video clips of resolution 720×576 was presented. The eye fixations of 15 subjects were recorded with an eye-tracker at 500 Hz in a free-viewing task. The video clips were about 1.3 seconds long, and they were collected from TV shows and news, animated movies, commercials, sports, music videos, indoor and outdoor scenes, etc. In total, there were about 1700 video frames in this dataset. The viewing distance was fixed at 57 cm. The eye-tracker was calibrated after every 5 video clips, and a control drift was performed before each stimulus.

In [17], the eye-tracking data of 8 subjects on 50 video clips (4 to 6 subjects per video clip) with a total length of 25 minutes (46,000 frames) was provided. The resolution of the video clips was 640×480. The video clips came from different genres such as TV programs, video games, outdoor scenes, crowds, sports, commercials, test stimuli, etc. The clips were 6 to 90 seconds long. An eye-tracker with a sampling rate of 240 Hz was utilized to record the right-eye position. A 9-point calibration was used to calibrate the eye-tracker after every 5 video clips. The viewing distance was fixed at 80 cm. About 200 calibrated eye movement traces (10,192 saccades) were analyzed, corresponding to 4 different observers for each of the 50 clips.

In [71], the gaze data of 5 subjects watching 24 game-play sessions with total length of 7.5 hours was recorded with a 240 Hz eye-tracker. Each game-play session was divided into smaller video segments. The video segments were 4-5 minutes long. In total, there were

about 216,000 video frames in this dataset. A 9-point calibration procedure was used before and after each video segment. The viewing distance was fixed at 80 cm.

In [72], a database of HD video clips alongside their eye-tracking data was presented. Fifty video clips of resolution 1920×1080 were used in this database. Each video clip was 300 frames long, and they included both indoor and outdoor scenes at daytime. The outdoor scenes included library, pool, traffic road, garden, lawn, park, etc. The indoor scenes included dinner hall, lab rooms, etc. Fourteen subjects were instructed to watch the video clips without any specific task, and they were asked to follow whatever interesting things they might like. A 240 Hz infrared-video-based eye-tracker was utilized to record the eye positions. The viewing distance was fixed at about 98 cm. A 9-point calibration procedure was used to calibrate the eye-tracker every ten video clips. The collected eye-tracking data was filtered for blinks, motion, eye wetting, and squinting. Also, the calibrated eye traces were visually inspected for their validity.

In [73], 23 subjects were asked to manually label salient regions of 431 videos with total length of about 7.5 hours (764,806 frames). This dataset covers videos from six different genres: documentary, advertisement, cartoon, news, movie and surveillance. In total, 62,356 key frames were selected from these videos, and 23 subjects were then asked to manually label salient regions in these key frames with one or multiple rectangles. Note that this is not really an eye-tracking dataset, since the salient regions were labeled manually by the subjects, which is a much more complicated task than free viewing. Another drawback of this dataset is that the salient regions were constrained to be collections of rectangles.

In [74], the eye gaze data of 10 subjects watching 2 video clips were recorded using a head-mounted eye-tracker. The eye-tracker tracks the center of the pupil based on dark pupil-corneal reflection video occulography at a sampling frequency of 60 Hz. Each video clip was one minute long, and it was extracted from a black-and-white film. The resolution of each video clip was 640×480. The viewing distance was fixed at 63.5 cm.

In [75], the eye gaze data of 250 participants watching 85 different videos were recorded. The videos were from different genres such as documentaries, game trailers, movie trailers, music videos, news clips and time-lapse footage, ranging from 27 to 217 seconds in length. In total, there were about 78,167 frames across all videos in this dataset. Participants' eye movements were tracked binocularly using an SR Research Eyelink 2000 desktop-mounted eye tracker with a sampling frequency of 1 KHz for each eye. Videos were displayed in

random order in their native resolutions on a 2100 Viewsonic Monitor with desktop resolution 1280×960 at 120 Hz at a viewing distance of 90 cm. Additional publicly-available eye-tracking datasets can be found in [76].

As seen above, although several eye-tracking datasets for video exist in the public domain, none of them has been made for "standard" video sequences that are familiar to video processing and compression research community, and are often used to evaluate new algorithms. This was our motivation to develop an eye-tracking dataset for "standard" sequences, such as *Foreman*, *Flower Garden*, etc.

3.2 Our database

3.2.1 Video sequences

To generate the eye-tracking data, we used the following 12 standard video sequences: *Foreman* (300 frames), *Bus* (150 frames), *City* (300 frames), *Crew* (300 frames), *Flower Garden* (250 frames), *Mother and Daughter* (300 frames), *Soccer* (300 frames), *Stefan* (90 frames), *Mobile Calendar* (300 frames), *Harbor* (300 frames), and *Tempete* (260 frames). The sequences were stored in YUV 4:2:0 format at CIF (352×288) resolution, and 30 frames per second (fps). These sequences were selected based on the fact that they are frequently used to test video compression, processing, and transmission algorithms. We believe that eye-tracking data for these sequences will facilitate the development and testing of novel perceptually-motivated video processing algorithms.

3.2.2 Eye tracker

To collect the eye-tracking data, we utilized a a Locarna "Pt-Mini" eye-tracker [77]. This eye tracker is head-mounted (using lightweight eye glasses) and allows subjects to move their head naturally. The eye tracker has two cameras, one pointing towards the subject's eye ("eye camera" of resolution 320×240), the other pointing forwards ("scene camera" of resolution 720×480). Both cameras operate at 30 fps. Fig. 3.1 shows a picture of the Locarna eye tracker.

To track the movement of the head relative to the screen, two red dots of radius 1 cm were placed in the left and right bottom corners of the screen. Tracking of these two dots in the scene camera view made it possible to compensate for the head movement and map

Figure 3.1: A photo of the Locarna eye tracker.

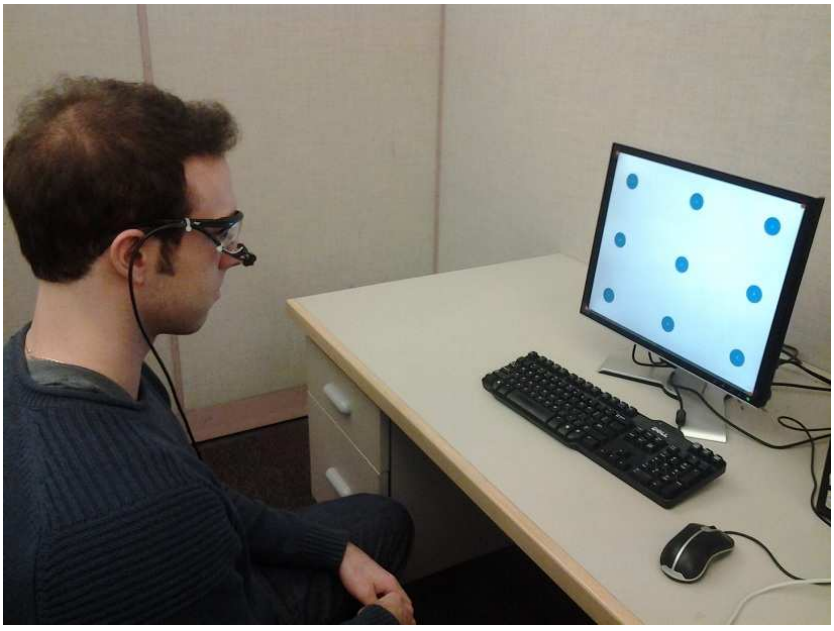

Figure 3.2: A photo of the eye-tracking setup.

the gaze locations onto the screen using a homographic transformation, without a head tracker. Given our experimental setup, subjects did not need to move their head much and further they remained at a fixed distance from the screen (80 cm) which allowed for a more precise mapping of the gaze data back onto the screen plane. Fig. 3.2 shows a picture of our experimental setup.

The advertised accuracy of the Locarna eye tracker is 1° or better in the field of view, which is the same as the advertised accuracy of other eye trackers on the market (e.g., Tobii, faceLAB, etc.). To verify this, we measured the accuracy of Locarna's eye tracker on 10 subjects. Out of these 10 subjects, 4 persons were wearing contact lenses, and the other 6 persons had normal vision. The subjects were graduate students in the School of Engineering Science at Simon Fraser University.

Each subject was seated in front of a 19″ Samsung SyncMaster 915N color monitor at a distance of 80 cm. The monitor resolution was set to 800×600, with vertical frequency of 75 Hz and horizontal frequency of 46.875 kHz. Other options were set to their factory default values. We first displayed the nine blue calibration dots shown in Fig. 3.3 on the monitor to calibrate the eye tracker. In the calibration procedure, the subject is instructed to fixate on the center of each of the nine dots in sequence: dot 1, dot 2, ..., dot 9. Each fixation was triggered by a vocal sound instructing the subject to look at the next dot. After each fixation, the two images captured by the scene camera and the eye camera were recorded for further processing. At the end of the calibration procedure, we obtained nine sets of coordinates in the real-world scene (the centers of the nine blue dots), and nine pupil locations. A manual inspection was then performed to make sure that the obtained center locations are correct and accurate. Finally, the obtained coordinates were used to compute the calibration matrix using a typical 8-point perspective projection and Singular Value Decomposition (SVD).

To test the eye tracker accuracy, we asked the subjects to fixate at each of the 12 red test dots shown in Fig. 3.4 for about one second, starting with the dot labeled "A," then moving to dot labeled "B" and so on up to dot labeled "L." The radius of the dots was 32 pixels. The relative position of the red test dots with respect to the blue calibration dots is shown in Fig. 3.5. As seen in Fig. 3.5, the test dots are positioned in between the calibration dots. The goal of this first test was to examine the accuracy of the eye tracker immediately after the calibration.

After the first test, we displayed a video (*Stefan*, CIF resolution) at the center of the

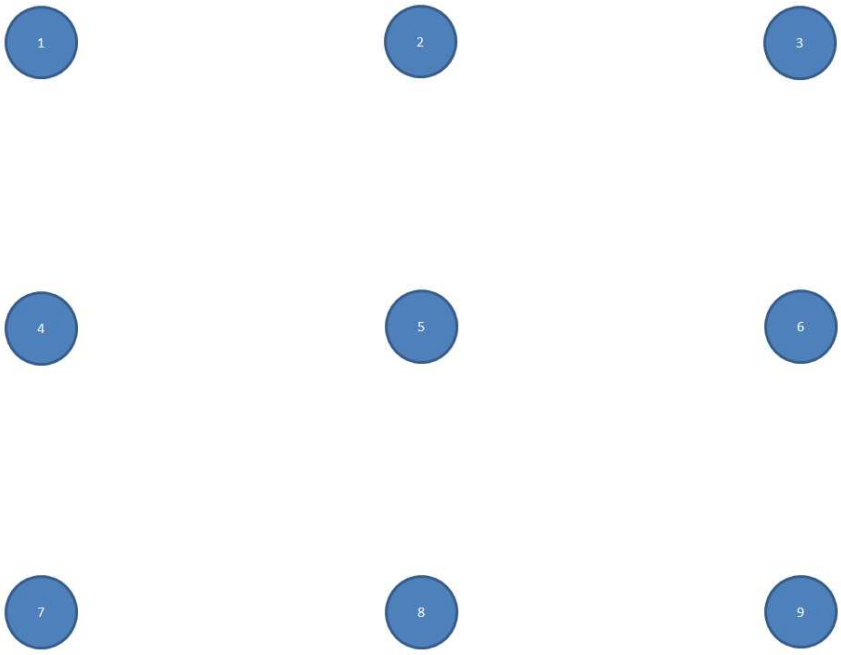

Figure 3.3: The dot pattern used for calibration.

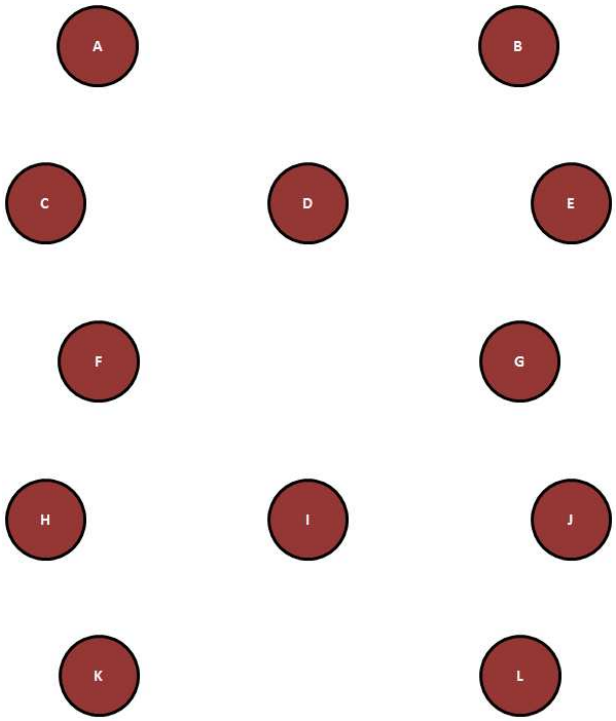

Figure 3.4: The dot pattern used for testing.

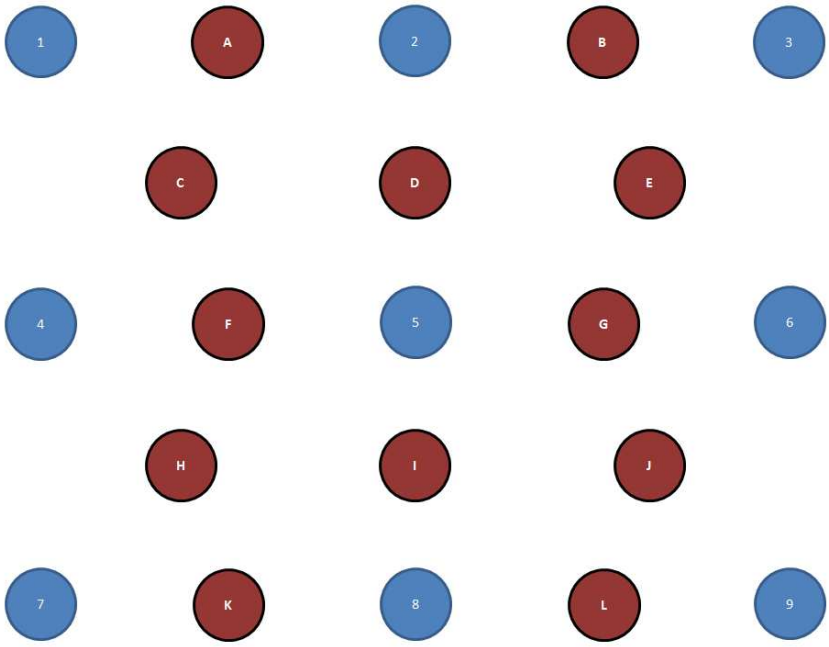

Figure 3.5: The relative position of the test dots with respect to the calibration dots.

screen for about 7 seconds. The subjects were instructed to look wherever they wish in the video during this time. After they were shown the video clip, the accuracy test was repeated on the red dot pattern shown in Fig. 3.4. The subjects were again asked to look at the test dots in sequence, starting with the dot labeled "A," down to the dot labeled "L." The goal of this second test was to examine the accuracy of the eye tracker some time after the calibration.

In order to measure the accuracy of the eye tracker, we first isolated those frames that recorded the fixation. These were the frames where the point of gaze did not move by more than n pixels in m consecutive frames. In other words, in a fixation group of frames, the gaze point is allowed to move by at most n pixels in m consecutive frames. In our experiments, we set $n = 50$ pixels and $m = 7$ frames. There were 6770 fixation frames in total, hence, on average, 677 per subject.

We then computed the Euclidean distance between the center of each test dot and the gaze location provided by the eye tracker in each frame of the corresponding fixation group. The computed distances were considered as the measurement errors in estimating the gaze location by the eye tracker. The obtained measurement errors are reported in Tables 3.1-3.3.

Table 3.1: Measurement error on all ten subjects.

Mean	Standard Deviation
16.56 pixels (0.45°)	13.36 pixels (0.36°)

Table 3.2: Measurement error on subjects with/without contact lenses.

Subjects	Mean	Standard Deviation
without contact lenses	15.61 pixels (0.42°)	11.25 pixels (0.30°)
with contact lenses	18.78 pixels (0.51°)	16.86 pixels (0.45°)
Difference	3.17 pixels (0.08°)	5.61 pixels (0.15°)

As seen in the tables, the average measured errors were under 0.5° of visual angle.

To check whether wearing contact lenses makes a difference to the accuracy, we performed a t-test [78] on the measurement errors with and without contact lenses in Table 3.2. The null-hypothesis was that the errors come from distributions with the same mean but unequal variance. The two-tailed p-value in this case was 9.3543×10^{-5}, indicating that the null-hypothesis needs to be rejected, and that the errors do come from distributions with different means. A similar test was performed for the two cases in Table 3.3 (before and after watching the video clip). The p-value was 7.8772×10^{-5} in this case, again indicating that the errors come from distributions with different means.

Based on the obtained results, the measurement error in the case of contact lenses tends to be higher than the error without lenses. However, the difference in the mean error in the two cases is very small, less than 0.1°. Fig. 3.6 shows two samples of the pupil detected by Locarna's eye tracker when using a hard contact lens. These two samples were extracted from a 1.5 hour video recorded by Locarna's eye tracker. As seen from these two samples, the pupil has been detected correctly.

Table 3.3: Measurement error before and after watching the video clip.

Viewing	Mean	Standard Deviation
before watching the video clip	15.63 pixels (0.42°)	13.24 pixels (0.35°)
after watching the video clip	18.25 pixels (0.49°)	13.16 pixels (0.35°)
Difference	2.62 pixels (0.07°)	0.08 pixels (0.00°)

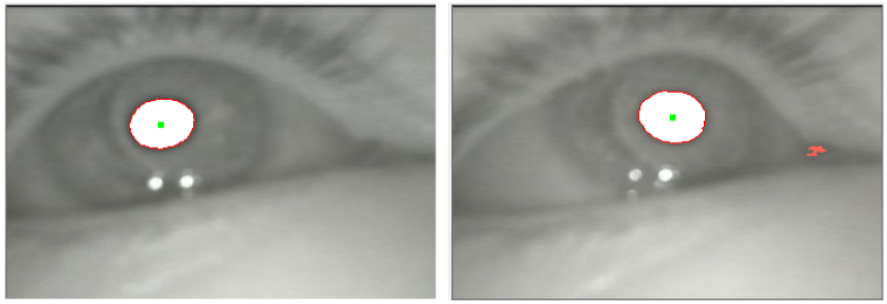

Figure 3.6: Two samples of the pupil detected by Locarna's eyetracker when using a hard contact lens.

We also note that the measurement error was higher on the second test (after watching the video clip) than on the first test, but again the difference in the mean error was very small, less than 0.1°. Overall, the mean measurement errors were around 0.5°, well below the advertised accuracy of the Locarna eye tracker of 1°. Even the mean error plus one standard deviation of the error was less than the advertised accuracy.

We uploaded a sample video of the performed experiment at the following online link at YouTube: `http://www.youtube.com/watch?v=lOL38F2VBFE`. This video shows the accuracy of the eye tracker on a subject wearing contact lenses with a mean error of about 0.5° of visual angle, which was roughly the mean error on the subjects with contact lenses. The video shows the measured gaze point with a cross-hair, along with two concentric circles. The smaller circle has a diameter of 1° (i.e., radius of 0.5°), and the larger circle has a diameter of 2° (radius of 1°). Overall, the tests confirmed the accuracy of the Locarna eye-tracker. This testing represents one of the unique features of our dataset. Most other datasets simply quote the advertised accuracy of their eye tracker, without really putting it to test.

3.2.3 Eye-tracking data collection

A total of 15 non-expert participants (2 women and 13 men) took part in the eye-tracking data collection study. They were recruited by a mass e-mail invitation and were paid $15 for their participation. All of them had normal or corrected-to-normal vision, and were asked to wear a Locarna "Pt-Mini" head mounted eye tracker [77] to determine their gaze direction. The participants consisted of undergraduate and graduate Simon Fraser University students aged between 18 and 30. None of the participants wore spectacles. The

pupil images captured by the eye camera were analyzed (in real time) by specific image processing techniques implemented in the eye tracker's software in order to find the exact location of the pupil center.

In order to map the location of the pupil to the real-world scene (i.e., scene camera view), a calibration matrix, obtained using the 9-dot calibration procedure described in Section 3.2.2, was used. In order to verify that the eye tracker remained calibrated throughout the duration of the experiment, a small crosshair was displayed on a blank screen after presenting each video clip, and the subjects were asked to fixate on the center of the crosshair. Any deviation from the true location was used as an out-of-calibration indicator. This allowed us to recalibrate the system in case of any miss-calibration.

The study was performed one participant at a time over a period of two days in June 2010. The experiment was run in a quiet room with an ambient light of 200 Lux, as recommended in [79] to simulate a "home environment." Each participant was seated in front of a 19″ Samsung SyncMaster 915N color monitor at a distance of 80 cm, and watched a video with pre-recorded instructions on how to complete the experiment before getting started. The monitor resolution was set to 800×600, with vertical frequency of 75 Hz and horizontal frequency of 46.875 kHz. Other options were set to their factory default values. The video clips were shown on the screen at twice their normal size so that they would occupy approximately 84% of the screen. The actual size of the video frames was about 40° of the visual angle. The video resolution was increased using nearest neighbor interpolation. This did not create visible artifacts at the viewing distance of 80 cm.

The 12 short video sequences were presented sequentially in a fixed order with a 3 second pause in-between. During this pause and before the beginning of each video, a small crosshair (centered on the video display area) was presented and the participants were asked to fixate on it. After the 12 videos had been presented, participants then had a 2-minute break after which the 12 videos were presented again. The participants were asked to look naturally at the videos and were not given any instructions as to what to look for in the sequences.

3.2.4 Gaze data visualization

The collected raw gaze data was analyzed, mapped from the head mounted eye tracker onto the video plane and stored in a comma separated value (CSV) file format. This file contains the frame-by-frame, pixel wise x- and y-coordinates (measured from the bottom

left corner) of the gaze location for each participant and each of the video sequences. All the obtained gaze data were inspected both manually and automatically to ensure that they are fairly reliable. Each gaze location stored in the mentioned CSV files was flagged as either correct (flag = 1) or incorrect (flag = 0) in a separate CSV mask file. The gaze data were also represented in two different visualizations for each video sequence: a moving heat map and a gaze plot comparing participants' first and second viewing of the sequences. In the heat map visualization (Fig. 3.7), the areas of the video that received the most visual attention are presented in white, followed by red, yellow green and blue as visual attention dropped. The heat maps were generated from the valid raw gaze location points collected for all participants based on the characteristics of the fovea. In each frame, we create a circular area with values following a Gaussian distribution around the gaze location of each participant. This Gaussian models the non-uniform distribution of the photoreceptors on the retina (i.e., the eccentricity of the fovea). The width of the Gaussian was set to 2 degrees of visual angle, which translates to 64 pixels in our case. The accumulation of the obtained Gaussian values resulted in the heat map for that frame. In the gaze plot visualization (Fig. 3.8), a pair of connected circles represent where each participant looked at the sequences the first and second time they were presented to them. Each participant's gaze location for the first and second view is represented in a different color. This data was collected in an effort to determine if a person who had just seen a particular video, and was thus familiar with it, would look at the same locations when viewing it a second time.

3.2.5 Database location, structure and accessibility

The database is available online at the following URL: `www.sfu.ca/~ibajic/datasets.html`. Each of the 12 video sequences is stored in a separate folder that contains the following:

- Original uncompressed sequences in YUV 4:2:0 format.
- Heat map visualization (-heatmap) video clips in compressed AVI format, similar to Fig. 3.7.
- First and second view visualization (-1vs2) video clips in compressed AVI format, similar to Fig. 3.8.
- A CSV file containing the x- and y-coordinates for each participant's first and second viewing for each frame of each video sequence.

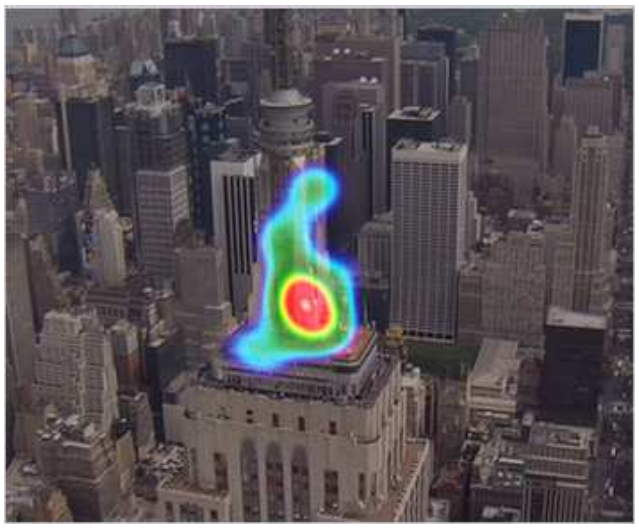

Figure 3.7: Heat map visualization of *City* for the first viewing.

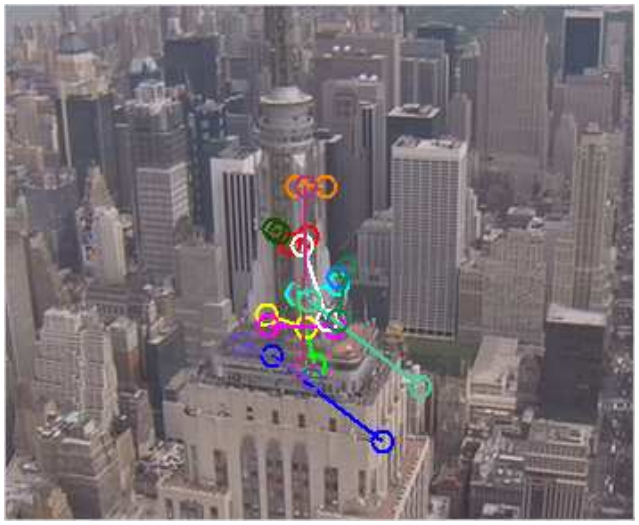

Figure 3.8: Gaze plot visualization comparing first and second viewing of *City*.

Table 3.4: Average distance between gaze locations in the first and second viewing.

Sequence	Average Distance	
	Pixels	% of diagonal
Bus	91.52	20.12
City	72.35	15.91
Crew	99.23	21.82
Foreman	46.18	10.15
Flower Garden	92.74	20.39
Hall Monitor	67.62	14.87
Harbor	78.27	17.21
Mobile Calendar	145.95	32.09
Mother & Daughter	70.03	15.40
Soccer	82.62	18.17
Stefan	41.38	9.10
Tempete	65.60	14.42

- A CSV file containing the binary flag matrix (-Mask) for each frame of each video sequence.
- A number of MATLAB functions to generate and visualize the heat maps and gaze data, as well as a user manual for the code.
- A brochure for the employed eye tracker (Pt-Mini), and a number of whitepapers and technical papers, which are also accessible at `http://www.locarna.com/docs/`.

3.3 Results

3.3.1 Congruency of first vs. second viewing

It is natural to ask whether people who view a particular video multiple times look at the same locations each time they view it. We hypothesized that this would not always be the case. In other words, we expect that in many cases people would tend to shift their gaze to different locations each time they view a particular video clip. We thus collected gaze location data for two sequential viewings of each sequence in our database in order to corroborate this hypothesis.

The gaze tracking data allowed us to compare where the participants' gaze was directed for each of the sequences the first time participants saw them, as well as when they were

viewed a second time. In each frame, there is a gaze location for the first and second viewing for each participant. Visualizations of the gaze locations for the first and second viewing (similar to Fig. 3.8) are also made available in the database. As anticipated, there was a notable difference in the locations of the participants' gaze for the first and second viewing. We computed the Euclidean distance between participants' gaze location on the first and second viewing, and then averaged those distances across different participants. The average distance for each of the video sequences is presented in Table 3.4, both in terms of pixels, and in terms of the percentage of the size of the CIF frame diagonal, which is $\sqrt{352^2 + 288^2} = 454.8$. As seen in the table, the average distance between the gaze locations could be as large as a quarter of the frame. Note, however, that the variability between the first and second viewing is likely to be influenced by the amount of time elapsed between the two viewings. Our main goal here is to raise awareness among the readers that such variability may exist, rather than provide an accurate model for such variability.

The shift in gaze locations was particularly evident for sequences such as *Crew*, *Flower Garden*, and *Mobile Calendar*, where there are numerous objects (none of which are strongly dominant) that compete for viewer's attention. Here, the word "dominant" refers to our subjective impression of what was dominant in a particular sequence or set of frames (e.g., the face in the initial part of *Foreman*). In cases where there was no single dominant object, the viewers tended to shift their gaze to a different object in the second viewing. On the other hand, in sequences with a single dominant object of interest, such as *City* and *Stefan*, the differences in gaze locations were related to the size of the object - small object (the tennis player) in *Stefan* gave rise to a small difference, while the large object (the central building) in *City* gave rise to a large difference. Bear in mind that in these sequences, as in those with multiple objects of interest, the gaze location did change between the first and second viewing, but usually remained within the dominant object of interest, as illustrated in Fig. 3.8.

Certain sequences presented interesting patterns when comparing first and second viewing. An example is *Foreman*, where the distance between gaze locations of the first and second viewing varied as the sequence progressed (Fig. 3.9). In the beginning of the sequence, when there is a face present in the video, gaze was concentrated on this face in both viewings. Hence, the gaze location difference in this part of the sequence was relatively small. As the sequence progresses, the camera pans to show a construction site, and there was a larger disparity between participants' gaze locations for the first and second viewing,

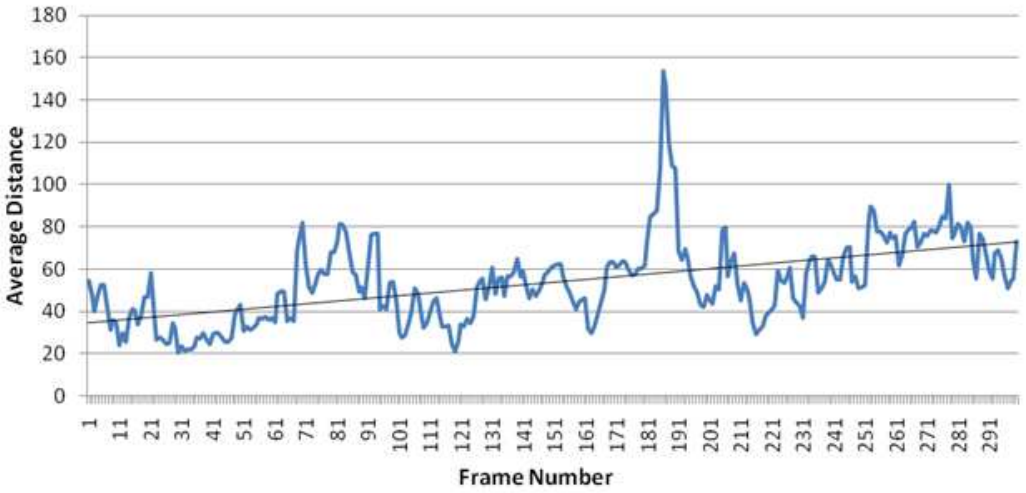

Figure 3.9: Average distance (in pixels) between gaze locations in the first and second viewing for *Foreman*, presented frame by frame.

because within the construction site, a larger number of regions of similar saliency compete for viewer's attention. In Fig. 3.9, we can see a definite trend: gaze distance between first and second viewing increases as the sequence progresses, and peaks between frames 180-190 when the camera starts to pan to the right. In general, such a behavior depends on the video content.

3.3.2 Accuracy of two popular visual attention models

One of the possible uses of this database is in testing prediction models of human attention. To show how this can be done, we utilized the gaze location data to determine the accuracy of two well-known visual attention prediction models: the Itti-Koch-Niebur (IKN) model [2], and the Itti-Baldi (IB) model [17], [57], [58]. Using the gaze location data, we were able to determine how well these two attention prediction models perform on each of the sequences in the database.

For each frame, both models produce a saliency map $s(x, y)$ that contains a predicted attention potential value (ranging from 0 to 255) for each pixel. However, they do not produce the same total saliency in each frame. In other words, $\sum s(x, y)$ is, in general, different for the two models. In order to have a fair comparison between the two models,

we normalized saliency values as follows:

$$s'(x,y) = \frac{s(x,y)}{\sum s(x,y)} N_{pixel}, \tag{3.1}$$

where N_{pixel} is the number of pixels in the frame. In our case (CIF resolution), $N_{pixel} = 352 \times 288 = 101,376$. After this normalization, both models produce the same total normalized saliency per frame, i.e., $\sum s'(x,y) = N_{pixel}$ for both models.

Using the normalized saliency maps, we proceeded to calculate the accuracy of the models by adding the normalized values of every pixel where a gaze was directed. If (x_i, y_i) is the pixel where i-th viewer's gaze was directed in a particular frame, the accuracy score of a model for that frame was computed as

$$Score = \sum_{i=1}^{15} \sum_{(x,y)} w_{x_i,y_i}(x,y) s'(x,y), \tag{3.2}$$

where i goes from 1 to 15 because there were 15 viewers in our study, and $w_{x_i,y_i}(x,y)$ is a 2-D isotropic Gaussian function centered at the i-th gaze location (x_i, y_i),

$$w_{x_i,y_i}(x,y) = \frac{1}{2\pi\sigma^2} \exp\left(-\frac{(x-x_i)^2}{2\sigma^2} + \frac{(y-y_i)^2}{2\sigma^2} \right). \tag{3.3}$$

This Gaussian function models both the non-uniform distribution of the photoreceptors on the retina, as well as the eye tracker measurement noise. It is assumed isotropic (i.e., $\sigma = \sigma_x = \sigma_y$) for convenience, and we set $\sigma = 64$ pixels, which corresponds to 2 degrees of visual angle. The average accuracy scores (over all frames) for each sequence are presented in Table 3.5, for both the first and second viewing. To examine whether the difference in the average scores between the IKN model and the IB model is statistically significant, we performed a paired t-test [78] on the frame-by-frame scores for each sequence and each viewing. The null-hypothesis was that the scores of both models come from the distributions with the same mean. Based on the results, the null-hypothesis was rejected (at the 5% significance level) in both viewings for all sequences. The obtained p-values were less than 10^{-6}, except for *Foreman* for the first viewing ($p = 0.000055$), and *Mother & Daughter* for the first viewing ($p = 0.002416$) and the second viewing ($p = 0.000027$). Therefore, based on our data, the difference in the average accuracy scores of two models was highly statistically significant in each case, and the model with the higher average score on a particular sequence can be considered more accurate on that sequence.

Table 3.5: Average accuracy score for predicting gaze location in first and second viewings.

Sequence	IKN Model [2]		IB Model [17]	
	View-1	View-2	View-1	View-2
Bus	23.50	20.83	15.77	14.94
City	9.12	10.67	13.39	14.61
Crew	19.60	18.95	16.16	16.53
Foreman	28.99	30.01	25.15	24.50
Flower Garden	51.31	48.93	19.35	20.48
Hall Monitor	81.62	83.71	59.35	59.00
Harbor	31.12	36.81	20.73	23.71
Mobile Calendar	44.74	40.21	21.40	21.17
Mother & Daughter	32.63	35.13	29.48	30.96
Soccer	31.19	29.12	23.04	22.62
Stefan	67.42	66.91	51.26	48.69
Tempete	34.33	34.05	28.02	28.80

Several observations can be made from the data in Table 3.5. First, the IKN model [2] showed better accuracy than the IB model [17] in 11 out of 12 sequences, while the IB model was more accurate in just one case (*City*). This finding is somewhat surprising, given that the IB model is more recent [17] and claimed to be an improvement over the IKN model.

We also ran the t-test to determine if there is any statistical basis for claiming that a particular model had better accuracy on the first or second viewing. The results were mixed. At the 5% significance level, the IKN model showed better accuracy on the first viewing for three sequences (*Bus*, *Mobile Calendar*, and *Soccer*), and on the second viewing for four sequences (*City*, *Foreman*, *Harbor*, and *Mother & Daughter*), while for the remaining sequences the difference was not statistically significant. The IB model showed better accuracy on the first viewing for three sequences (*Bus*, *Foreman*, and *Stefan*), and on the second viewing for five sequences (*City*, *Flower Garden*, *Harbor*, *Mother & Daughter*, and *Tempete*), while there was no statistically significant difference on other sequences. Overall, according to this data, both models seem to be roughly equally suitable for first and second viewing.

While Table 3.5 provides the data to compare the relative accuracy of the two models, it is natural to ask how accurate these models are in absolute terms. One way to tackle this question is to compare these models with uniformly spread saliency. Suppose we assign the same saliency to each pixel, i.e., $s_u(x, y) = 1$ for all (x, y). With such uniformly spread saliency, the total normalized saliency is the same as for the two models above ($\sum s_u(x, y) =$

Table 3.6: Average accuracy score for the uniformly spread saliency in the first and second viewing.

Sequence	View-1	View-2
Bus	14.55	14.63
City	14.57	14.44
Crew	13.21	13.62
Foreman	14.67	14.66
Flower Garden	14.48	14.55
Hall Monitor	13.48	14.65
Harbor	14.50	13.86
Mobile Calendar	14.26	14.41
Mother & Daughter	14.47	14.73
Soccer	12.91	14.26
Stefan	14.82	13.37
Tempete	14.42	13.79

N_{pixel}), so a fair comparison is possible. The average accuracy scores for such uniformly spread saliency computed using equation (3.2) are listed in Table 3.6. One could argue that if a particular model does not produce a score significantly above that listed in Table 3.6, it really isn't any more accurate than uniformly spread saliency. Again, we used the t-test to assess whether a particular model's score was significantly better (or worse) than that produced by uniform saliency. The IKN model's score on *City* was significantly lower than that produced by uniform saliency on both views of *City*, and significantly better in all other cases. Meanwhile, the IB model's score was significantly lower than that produced by uniform saliency on the first view of *City*, while there was no significant difference on the second view of *Bus* and *City*. In all other cases, the IB model had a significantly higher accuracy than uniform saliency. Overall, the scores were the highest (and the models were most accurate) on sequences with few dominant moving objects, such as *Stefan* and *Hall Monitor*, whereas both models showed lower accuracy on sequences where there were multiple objects competing for viewers' attention. One perhaps surprising finding was that both models had a problem with the sequence *City*, which contains a single large dominant object (the central building). A possible reason may be that this dominant object has a similar color and texture distribution as the background, and appears relatively static relative to the background as the camera revolves around it, so it is not being picked up by the contrast analysis modules employed by both models.

For completeness, we also compared the accuracy of the two models using the popular

receiver operating characteristic (ROC) area under curve (AUC) measure [80],[81],[82]. In order to compute the AUC score for a saliency map, the hit rate is computed by determining the locations where the saliency map is above a certain threshold and a fixation is present in those regions. Similarly, the false alarm rate is computed by finding the locations where the saliency values are above the threshold while there is no fixation present in those regions. The ROC curve is then generated by varying the threshold to cover a wide range of possible saliency values. The area under the ROC curve is the AUC score. An AUC value of 0.5 corresponds to pure chance, a value greater than 0.5 indicates positive correlation, and 1.0 corresponds to a perfect prediction of eye fixations [80].

The mean AUC scores of the two models for each viewing are shown in Table 3.7. To check for the statistical difference between the mean AUC scores of the two models, we performed a t-test with the null hypothesis that the mean AUC scores of the two models come from Gaussian distributions with equal means. The resultant p-values are also reported in this table. As seen from the results in this table, the IKN model outperforms the IB model in 8 out of 12 cases on the first viewing, and in 6 out of 12 cases on the second viewing. We also note that the performance of the two models is statistically the same on *Mother & Daughter* on both viewings, since the p-value is larger than 0.05. In all other cases, the corresponding p-values are below 0.05, which means that one of the methods obtained a statistically significant advantage in the average score. We also observe that the accuracy of the two models on *City* is around the chance level in both viewings, a result that was previously observed in Table 3.5. Fig. 3.10 shows the average ROC curve of the two models (across all the 12 sequences) for both viewings. As seen from these results, the average accuracy of the IKN model is better than the IB model across all the tested sequences. More specifically, in the first viewing, the average AUC score of the IKN model is about 0.6586 while the average AUC score of the IB model is about 0.6447 with a p-value of 0.022343. In the second viewing, the average AUC score of the IKN model is about 0.6599 while the average AUC score of the IB model is about 0.6561 with a p-value of 0.037517.

3.4 Conclusions

As video compression and processing algorithms evolve to incorporate models of human perception and attention, it becomes imperative to have the tools to test them. In this chapter

Table 3.7: Average AUC score for predicting gaze location in first and second viewing.

Sequence	View-1			View-2		
	IKN	IB	p-value	IKN	IB	p-value
Bus	0.621949	0.556842	0.000000	0.594323	0.526464	0.000000
City	0.465959	0.518376	0.000000	0.468320	0.521248	0.000000
Crew	0.589822	0.573459	0.004724	0.558933	0.577167	0.000439
Foreman	0.651316	0.615346	0.000000	0.673088	0.637185	0.000000
Flower Garden	0.641450	0.572421	0.000000	0.645224	0.585146	0.000000
Hall Monitor	0.818588	0.803635	0.000002	0.814053	0.798362	0.000002
Harbor	0.603295	0.552790	0.000000	0.641240	0.606229	0.000000
Mobile Calendar	0.662766	0.665117	**0.658195**	0.675020	0.668334	**0.203678**
Mother & Daughter	0.662984	0.747836	0.000000	0.669394	0.772578	0.000000
Soccer	0.724149	0.657288	0.000000	0.691267	0.631822	0.000000
Stefan	0.786270	0.812734	0.000059	0.806129	0.839072	0.000007
Tempete	0.674131	0.660761	0.002250	0.682309	0.709505	0.000000

we presented an eye-tracking database for a set of 12 standard CIF video sequences commonly used in the literature to compare video compression and processing algorithms. The database itself is available for public download at `www.sfu.ca/~ibajic/datasets.html`. We have described the procedure followed in order to produce this database, and also presented a preliminary analysis of the obtained data. An interesting finding stemming from the data is that gaze locations tend to be different in different viewings of the same video, which may have implications in the design of compression algorithms intended for one-time viewing (e.g., videoconference), compared to those intended for multiple viewings (e.g., DVD and Blu-ray). We also showed how the data can be used to compare models of visual attention in terms of their accuracy in predicting gaze locations. The eye-tracking data provided in this database can also be utilized for measuring the subjective quality of videos. For instance, the eye-tracking heat maps of the videos can be employed as a weight map to compute an Eye-tracking-Weighted Peak Signal to Noise Ratio (EWPSNR) [72]. Using this approach, the PSNR values in fixation regions get a higher weight than the rest of the frame. This makes the conventional PSNR more relevant for measuring the subjective quality of videos. The MATLAB code for computing the EWPSNR metric is also available in the database. It is worth pointing out that EWPSNR is similar to the Foveal Weighted SNR (FWSNR) metric proposed in [83]. However, unlike FWSNR, EWPSNR uses the actual gaze point measurements to weight the MSE distortion.

Some of the limitations of the database include the accuracy of the data, which is limited

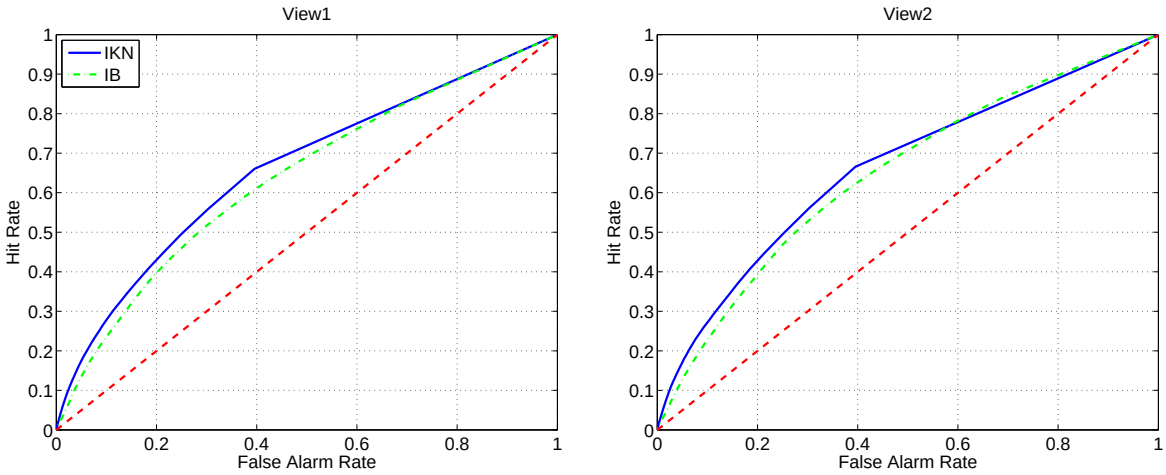

(a) (b)

Figure 3.10: Average ROC curves of the IKN and IB models for the first viewing (left) and second viewing (right). The dashed diagonal line in the two figures shows an AUC score of 0.5, corresponding to pure chance.

to about 1° in the field of view by the eye-tracking equipment and setup, and the number of video sequences and participants, both of which should ideally be as high as possible. Further, the distances between participants' gaze locations in the first and second viewing should be taken with a grain of salt, since they likely depend on the amount of time elapsed between the viewings. Our data is intended mainly to raise awareness that such variability may exist. Nonetheless, despite these limitations, we hope the data will be useful to the research community.

Chapter 4

Computationally-Efficient Saliency Estimation

4.1 Background

As mentioned in Chapter 2, the Itti-Koch-Niebur (IKN) saliency model [2] is one of the most well-known and widely-used bottom-up models of visual attention. However, this model is very complex as it requires multiresolution analysis of the input image or video in the pixel domain in various feature channels such as intensity, color, orientation, flicker, and motion. Hence, the high computational complexity of the IKN model limits its applications, especially in real-time scenarios, where fast saliency estimation is required.

In this chapter, we present two computationally-efficient saliency estimation methods. The first one is a convex approximation to the IKN model for both static images and video, which operates solely in the Discrete Cosine Transform (DCT) domain. The computational cost of this approximation is only a fraction of that of the IKN model, while at the same time, its accuracy is very close to the that of the IKN model. The lower computational cost is due to the fact that our approximation does not require multiresolution analysis as it operates in the DCT domain in which different DCT coefficients carry the information from different resolution levels. Many image and video processing systems (e.g., codecs) incorporate DCT. Hence, DCT information is often available at no extra computational cost, and it makes good engineering sense to reuse it. In addition to the lower computational cost, the convexity of our approximation makes it attractive to incorporate within various

optimization procedures in image and video processing. One example is given in Chapter 6, where this approximation is used to make a saliency-cognizant error concealment problem convex, which in turn leads to an efficient solution.

It is worth pointing out that in [84], a saliency detection method for static images in the JPEG compressed domain was proposed. In this method, several features such as the intensity, color, and texture information are first extracted from the DCT coefficients of each 8×8 block in the image. For example, the DC values of the luma and chroma channels are converted to the RGB color space so that the intensity and color opponent features (i.e., blue-yellow and red-green) can be computed for each block. The AC coefficients of each block are also used to extract the orientation or texture information of each block. This gives a texture feature vector per each 8×8 block. In the end, four feature maps are created: one intensity, two color opponent features, and one texture feature. The next step in this method is to compute the feature difference between the feature values of each pair of blocks in each feature map. To measure the feature difference in the intensity and color opponent channels, the feature values are directly subtracted from each other while a Hausdorff distance [84] is used to measure the dissimilarity between two texture feature vectors in the texture feature map. The saliency value for each DCT block in each feature map is then determined by the block differences between each DCT block and all other DCT blocks of the input image. The block differences are also weighted by a Gaussian function of the Euclidean distance so that spatially-closer blocks have more contribution to the saliency value of each block. This step gives a conspicuity map for each feature map. The final saliency map is then computed by combining all the computed conspicuity maps using a specific fusion method [84].

Although the method from [84] works in the DCT domain, it is different from our proposed approximation to the IKN model in several aspects. First, unlike [84], our method attempts to approximate the well-known IKN saliency, rather than provide a saliency estimate based on some other principles. Second, our method offers an estimate of saliency that is convex in the input data, which makes it attractive for use in various optimization problems. Third, the computational complexity of our method appears to be lower than that of [84], since our method simply sums up the weighted squared magnitudes of the DCT coefficients of individual image blocks, whereas the method in [84] involves computing and combining several feature maps over the entire image.

The second saliency estimation method presented in this chapter is an extension of the

abovementioned convex approximation to IKN saliency. The main difference is in the part that estimates motion-induced saliency, where we incorporate global motion compensation (GMC) [14] prior to saliency estimation. Although this second method is not convex in the input data and is more complex than the first method, it is still simpler than the IKN saliency model and offers comparable accuracy, somewhat higher on sequences with camera motion.

This chapter is organized as follows. In Section 4.2, we present our convex approximation to the IKN saliency model. We then present the second saliency estimation method based on GMC in Section 4.3. The results are presented in Section 4.4. We provide an analysis of the computational complexity of the proposed saliency detection methods in Section 4.5, and conclusions are drawn in Section 4.6.

4.2 A convex approximation to IKN saliency

Our convex approximation to the IKN saliency consists of two parts: spatial and temporal. Let $\mathbf{X}$ be a block within a given frame. We will show how to compute an approximation $\mathcal{S}(\mathbf{X})$ to the IKN saliency of that block.

The dyadic Gaussian pyramid employed in the IKN model approximately halves the normalized frequency spectrum of the input image at each level due to the successive low-pass filtering. Since the normalized frequency (in radians/pixel) of the original image at level 0 is $[0, \pi]$ in both horizontal and vertical directions, the normalized frequency spectrum at level c of the pyramid is in the range $[0, \pi/2^c]$. Hence, the normalized frequency spectrum at levels 4 and 8 will be, respectively, in the range $[0, \pi/16]$ and $[0, \pi/256]$. As mentioned in Section 2.2.1, in the IKN model, a center-surround feature map at center level $c \in \{2, 3, 4\}$ and surround level $s = c+\delta$, with $\delta \in \{3, 4\}$, is computed by interpolating the surround level to the center level followed by point-by-point subtraction. Hence, the normalized frequency spectrum of the center-surround feature map at center level c and surround level s will be, in the range $[\pi/2^s, \pi/2^c]$. To compute the conspicuity map of each feature channel, all the computed center-surround feature maps are resized to the size of level 4. Hence, the upper limit of the normalized frequency spectrum of the obtained conspicuity map is capped by $\pi/16$. Since the smallest surround map is at level 8, we conclude that the IKN model uses the image content in the normalized frequency range $[\pi/256, \pi/16]$ to construct the saliency map, as already observed in [1, 85]. Note that the normalized frequency (in radians/pixel)

is defined with respect to the original image, regardless of the resolution.

To compute spatial saliency, we need a way to use the pixels of a given block $\mathbf{X}$ to estimate the saliency of the original image at that position. Based on the discussion above, it seems natural to try to recapture the portion of the image signal from the normalized frequency range $[\pi/256, \pi/16]$ at the position of the block $\mathbf{X}$. However, the process of extracting a block from an image involves windowing and spectral down-sampling, which leads to spectral leakage. Some energy from the normalized frequency range $[\pi/256, \pi/16]$ *of the original image* will be present at other frequencies when one examines the spectrum of the block $\mathbf{X}$.

To demonstrate the effect of spectral leakage, consider a simple 1-D example shown in Fig. 4.1. The red signal in this figure shows the 1-D DCT of a pure first harmonic signal of length 16, which is defined as follows

$$x[n] = \cos(\frac{2\pi n}{16}), \tag{4.1}$$

for $n = 0, 1, \cdots, 15$. We will extract a segment of length 8 from the middle part of this signal as follows. We first multiply the signal by a rectangular window of length 8, centered in the middle of the signal; the 1-D DCT at this point is shown as green in the figure. Then we remove the zeros outside the interval where the window function is equal to one; the 1-D DCT of the resulting signal is shown as blue. Note that the signal energy, which was originally concentrated in only one DCT coefficient, has now leaked into certain higher frequency coefficients (coefficients 3, 5 and 7). However, since the ratio of the length of the original signal and the length of the extracted segment is an integer ($16/8 = 2$), no energy has leaked into the DC coefficient (coefficient 0).

Fig. 4.2 shows another example in which the original signal length is 16 but the extracted segment length is 7. Here, due to the non-integer ratio between the original signal length and the extracted segment length, some energy leaks into the DC coefficient as well. Hence, depending on the ratio between the signal size and the block size, original signal energy may or may not leak into certain DCT coefficients.

In order to address this issue we take the following approach. Consider the original image spectrum in the normalized frequency range $[0, \pi]$. We think of the image signal in the normalized frequency range $[\pi/256, \pi/16]$ as the "signal," and the signal in the remaining part of the spectrum, $[0, \pi/256) \cup (\pi/16, \pi]$, as "noise," or "undesired signal." After extracting a block from the image, both the signal and the noise leak from their native

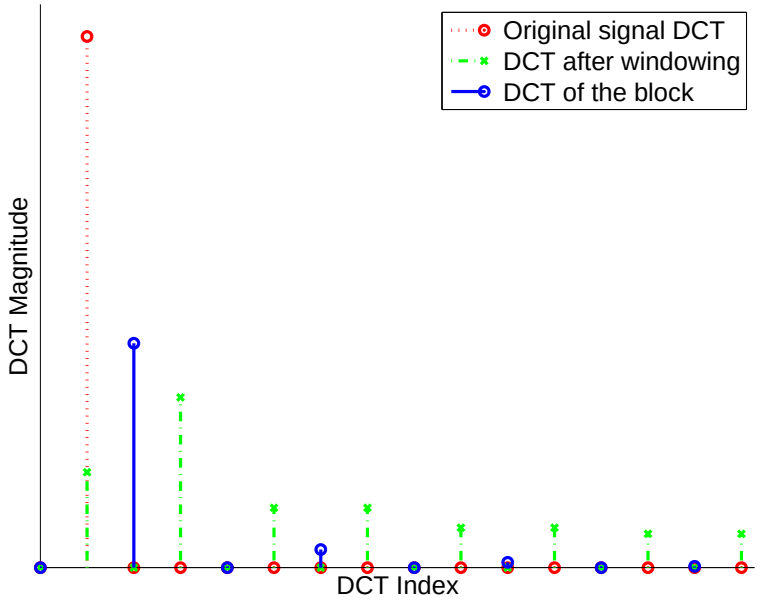

Figure 4.1: A simple example showing the effect of spectral leakage. In this example, the original signal is of length 16 while the extracted block is of length 8.

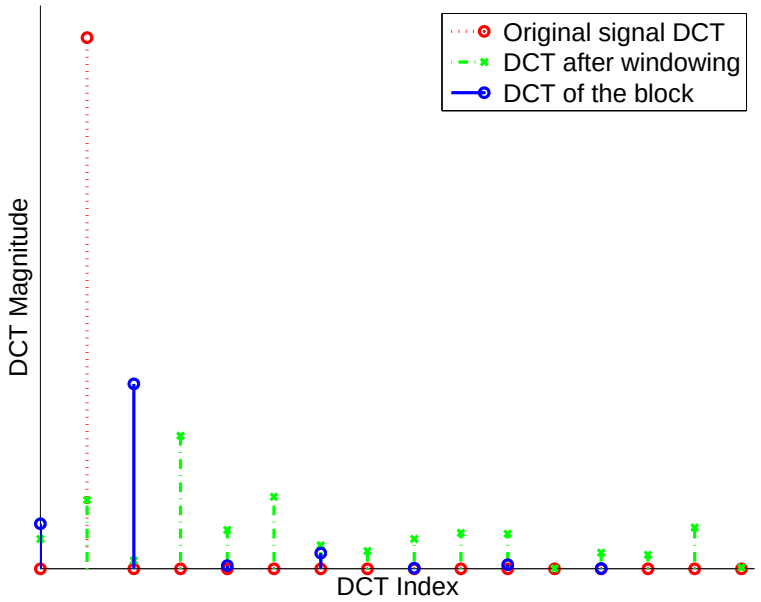

Figure 4.2: A simple example showing the effect of spectral leakage. In this example, the original signal is of length 16 while the extracted block is of length 7.

frequency bands into other bands. The spectrum of the block $\mathbf{X}$ is the sum of the leaked spectra of the signal and the noise. We need to extract the signal from noise. Since the signal and the noise come from non-overlapping frequency bands in the original image, they are orthogonal. The Wiener filter is the optimum linear filter for extracting the signal from noise, and when the signal and noise are orthogonal, its transfer function is [86]

$$H(\omega) = \frac{S_S(\omega)}{S_S(\omega) + S_V(\omega)}, \tag{4.2}$$

where $S_S(\omega)$ is the power spectral density of the signal, and $S_V(\omega)$ is the power spectral density of the noise. Hence, the Wiener filter is a frequency-domain weighting function [87].

We perform Wiener filtering in the DCT domain, rather than DFT domain, because DCT is simpler to compute (no need for complex arithmetic) and its efficient implementations are readily available in various image and video codecs. Let $\mathbf{Z}_{\mathbf{X}}(j,l)$ be the (j,l)-th 2-D DCT coefficient of $\mathbf{X}$, which is computed as follows

$$\mathbf{Z}_{\mathbf{X}}(j,l) = \frac{1}{4} C_j C_l \sum_{y=0}^{N_b-1} \sum_{x=0}^{N_b-1} \mathbf{X}(y,x) \cos\left(j\pi \frac{2y+1}{2N_b}\right) \cos\left(i\pi \frac{2x+1}{2N_b}\right), \tag{4.3}$$

where N_b is the width (and height) of $\mathbf{X}$, $\mathbf{X}(y,x)$ is the (y,x)-th element of $\mathbf{X}$, and

$$C_u = \begin{cases} \frac{1}{\sqrt{2}} & \text{if } u = 0 \\ 1 & \text{else,} \end{cases} \tag{4.4}$$

with $u \in \{j,l\}$. The Wiener-filtered coefficient is

$$\mathbf{Z}^W_{\mathbf{X}}(j,l) = \mathbf{H}(j,l)\mathbf{Z}_{\mathbf{X}}(j,l), \tag{4.5}$$

where $\mathbf{H}(j,l)$ is a coefficient that should be computed as in (4.2) based on signal and noise powers at the (j,l)-th 2-D DCT coefficient. A common way to design a Wiener filter is to postulate certain signal and noise models, and derive the filter from the resulting power spectral densities [88]. We use the $1/f$-model, which is thought to be an excellent model for natural images [89], as a starting point; our "signal" is the part of the $1/f$ signal in the frequency band $[\pi/256, \pi/16]$, and our "noise" is the part of the $1/f$ signal in the remainder of the spectrum.

To compute $\mathbf{H}(j,l)$, we proceed as follows. We generate a deterministic $1/f$ 2-D signal that covers the frequency band $[\pi/256, \pi/16]$, at a size equal to the target image resolution.

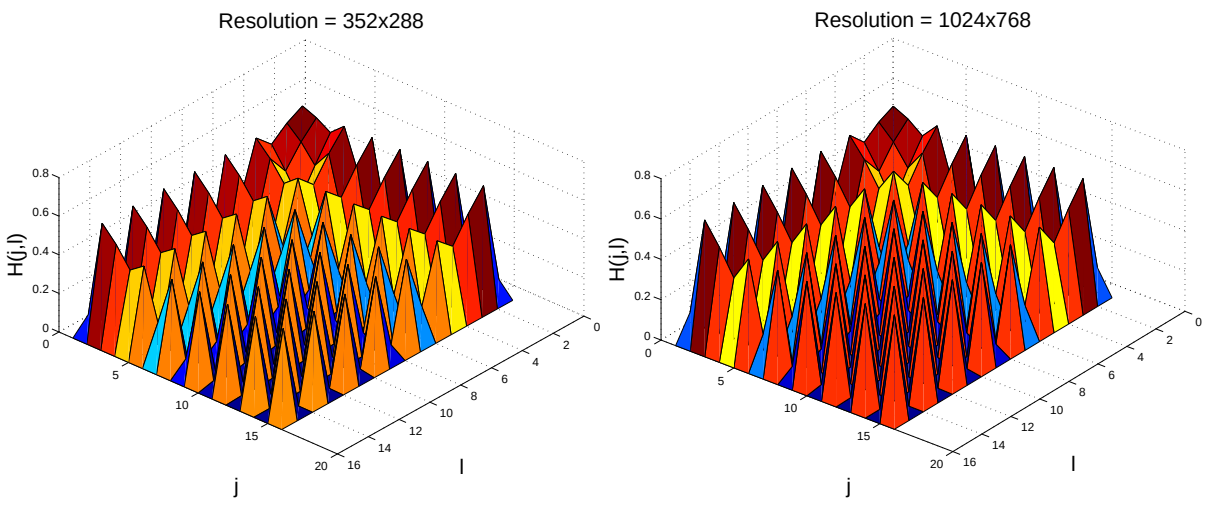

Figure 4.3: Wiener coefficients for a 16×16 block for two common resolutions.

We then extract from this signal a block whose size is equal to the block size of interest and perform a 2-D DCT on it. Let us denote the resulting DCT by $\mathbf{Z_S}(i,j)$. Then $\mathbf{Z_S}^2(i,j)$ is the signal power associated with that DCT coefficient, corresponding to $S_S(\omega)$ in (4.2). Similarly, we find the noise power associated with DCT coefficient (i,j), $\mathbf{Z_V}^2(i,j)$ by using a deterministic $1/f$ 2-D signal that covers the frequency band $[0,\pi/256) \cup (\pi/16,\pi]$. The DCT-domain Wiener filter coefficients are then given by

$$\mathbf{H}(j,l) = \frac{\mathbf{Z_S}^2(j,l)}{\mathbf{Z_S}^2(j,l) + \mathbf{Z_V}^2(j,l)}, \tag{4.6}$$

Note that $\mathbf{H}(j,l)$ depends on image resolution and the block size, due to the way $\mathbf{Z_S}(i,j)$ and $\mathbf{Z_V}(i,j)$ are computed, but can be easily pre-computed for typical resolutions and block sizes. Fig. 4.3 shows the Wiener coefficients obtained by the proposed method for two standard resolutions, 352×288 and 1024×768, and a block size of 16×16. Observe that Wiener coefficients for low frequencies are larger than those for high frequencies, as one would expect for a signal that came from the normalized frequency band $[\pi/256, \pi/16]$ in the original image. However, due to spectral leakage, some of the higher frequency coefficients also contain part of the signal, which makes their Wiener coefficients non-zero.

Our approximation to the spatial saliency of block $\mathbf{X}$ is the power of the Wiener-filtered

signal $\mathbf{Z}_{\mathbf{X}}^{W}$, that is

$$\mathcal{S}_{spatial}(\mathbf{X}) = \sum_{(j,l)} (\mathbf{Z}_{\mathbf{X}}^{W}(j,l))^2 = \sum_{(j,l)} \mathbf{H}^2(j,l) {\mathbf{Z}_{\mathbf{X}}}^2(j,l). \tag{4.7}$$

If block $\mathbf{X}$ has multiple color channels (e.g., YUV), the power in all channels is added together. Since DCT is a linear operation, as is Wiener filtering, while squaring is a convex operation, the saliency estimate $\mathcal{S}_{spatial}(\mathbf{X})$ in (4.7) is convex in $\mathbf{X}$.

As mentioned in the review of the IKN model in Section 2.2.1, the same center-surround mechanism that is used for the intensity, color, and orientation channels is used for computing the motion and flicker conspicuity maps. However, in the flicker and motion channels, the center-surround mechanism is applied on the absolute luminance difference or spatially-shifted difference between the current frame and the previous frame. Based on this fact, we now provide a convex approximation to temporal saliency. Let $\mathbf{X}_0$ be the co-located block of $\mathbf{X}$ in the previous frame, and let $\mathbf{Q} = |\mathbf{X} - \mathbf{X}_0|$ be the residual block obtained by taking the absolute difference between $\mathbf{X}$ and $\mathbf{X}_0$. Our approximation to the temporal saliency of block $\mathbf{X}$ is the power of the Wiener-filtered signal $\mathbf{Z}_{\mathbf{Q}}^{W}$, that is

$$\mathcal{S}_{temporal}(\mathbf{X}) = \sum_{(j,l)} (\mathbf{Z}_{\mathbf{Q}}^{W}(j,l))^2 = \sum_{(j,l)} \mathbf{H}^2(j,l) {\mathbf{Z}_{\mathbf{Q}}}^2(j,l), \tag{4.8}$$

where ${\mathbf{Z}_{\mathbf{Q}}}^2(j,l)$ is the (j,l)-th 2-D DCT coefficient of $\mathbf{Q}$. Note that $\mathcal{S}_{temporal}(\mathbf{X})$ is convex in $\mathbf{X}$ because $\mathbf{Q}$ is convex in $\mathbf{X}$, DCT and Wiener filtering are linear, and squaring is a convex operation.

In order to get the final saliency estimate of $\mathbf{X}$, we combine the spatial and temporal saliency terms as follows

$$\mathcal{S}(\mathbf{X}) = \mathcal{S}_{spatial}(\mathbf{X}) + \alpha \mathcal{S}_{temporal}(\mathbf{X}), \tag{4.9}$$

where α is a positive parameter that trades off between the two saliency terms. We note that $\mathcal{S}(\mathbf{X})$ is convex in $\mathbf{X}$ because it is a non-negative linear combination of convex terms.

This saliency estimate will be evaluated and compared against the IKN saliency in Section 4.4.1, where the results will show that (4.9) offers a very good approximation to IKN saliency. Next, we present the second saliency estimation method, which makes use of the spatial saliency term from above, but uses global motion compensation prior to computing motion saliency.

4.3 Global motion-compensated saliency

It is well-known that object motion is one of the strongest attractors of visual attention [90], [91], [55]. In many existing computational models of visual attention, such as the IKN model, the temporal saliency is estimated by measuring the local motion contrast [67]. An object with significant motion with respect to its surroundings would be considered as a strong, attention-grabbing "surprise" to the visual system, and hence salient.

In [92], it was observed that the accuracy of the IKN model degrades on scenes with camera motion. When the camera moves, the resulting apparent motion of the background competes with foreground object motion and may confuse the saliency model, leading to lower accuracy. To mitigate this problem, similar to [55] and [91], we remove the camera motion prior to computing temporal saliency.

To make the process computationally efficient, particularly for video compression applications, we use the previous frame's motion field (which is already computed) as an approximation to the current frame's motion field, and run an efficient global motion estimation algorithm [14] that uses only motion vectors (MVs), followed by global motion compensation, i.e. subtraction of global motion from the motion field. This way, we obtain one global motion-compensated MV (GMC-MV) per 4×4 block. For each block $\mathbf{X}$, the average magnitude of all GMC-MVs in it is taken as its motion saliency $\mathcal{S}_{motion}(\mathbf{X})$.

In order to obtain the overall global motion-compensated saliency $\mathcal{S}_{gmc}(\mathbf{X})$, we combine the spatial saliency $\mathcal{S}_{spatial}(\mathbf{X})$ from the previous section with the abovementioned motion saliency using the fusion method from [93], [94], as follows

$$\mathcal{S}_{gmc}(\mathbf{X}) = (1-\alpha_g)\mathcal{S}_{spatial}(\mathbf{X}) + \alpha_g \mathcal{S}_{motion}(\mathbf{X}) + \beta_g \mathcal{S}_{spatial}(\mathbf{X})\mathcal{S}_{motion}(\mathbf{X}), \qquad (4.10)$$

where α_g and β_g are positive constants. The first two terms in (4.10) allow the spatial and motion saliency to promote a block independently. On the other hand, the third term in (4.10) weighs the spatial saliency value by the motion saliency value and vice versa. Hence, it is a mutual reinforcement term, which promotes those blocks that are salient both spatially and temporally. As mentioned earlier, it is known that motion cues are one of the strongest attractors of visual attention [90]. Hence, in practice, a larger relative weight for the motion saliency ($\alpha_g > 0.5$) is recommended. In our experiments, we set $\alpha_g = 0.9$ and $\beta_g = 1$.

Our experimental results in Section 4.4.2 indicate that the performance of the global

motion-compensated saliency estimate in (4.10) is comparable to the IKN saliency model for video, even better when camera motion is present in the scene.

4.4 Accuracy

In this section, we first evaluate the accuracy of our convex approximation to IKN saliency in Section 4.4.1, followed by performance evaluation of the global motion-compensated saliency estimation method in Section 4.4.2.

4.4.1 Assessment of the convex approximation to IKN saliency

As explained in Section 4.2, our approximation to IKN saliency has two terms: spatial and temporal. The approximation accuracy of the spatial term (4.7) with block size was 16×16 is assessed first on two popular still image datasets with associated ground truth eye-tracking data (fixation points). The first dataset is the so-called Toronto data set [68], which contains 120 RGB images (688×512 pixels) of outdoor and indoor scenes with eye-tracking data of 20 subjects. The second data set is the so-called MIT data set [69],[82], which contains 1003 RGB indoor and outdoor images (1024×768 pixels) with eye-tracking data of 15 subjects.

The accuracy of spatial saliency detection is measured by the popular receiver operating characteristic (ROC) area under curve (AUC) measure [80],[81],[82]. In order to compute the AUC score for a saliency map, the hit rate is computed by determining the locations where the saliency map is above a threshold and a fixation is present in those regions. Similarly, the false alarm rate is computed by finding the locations where the saliency values are above the threshold while there is no fixation present in those regions. The ROC curve is then generated by varying the threshold to cover a wide range of possible saliency values. The area under the ROC curve is the AUC score. An AUC value of 0.5 corresponds to pure chance, a value greater than 0.5 indicates positive correlation, and 1.0 corresponds to a perfect prediction of eye fixations [80].

Table 4.1 shows the average AUC scores of the spatial IKN model and our approximation on each of the two datasets. As seen from the table, the average AUC scores of the proposed approximation are very close to the average AUC scores of the IKN model in each of the two datasets, indicating good approximation. To check for the statistical significance of this observation, we performed a paired t-test [95] between the AUC scores on each pair of images

Table 4.1: Average AUC scores of the spatial IKN saliency and the proposed approximation on two common datasets.

Dataset	IKN Saliency Model	Proposed Approximation	p-value
Toronto	0.6512	0.6468	0.6233
MIT	0.6261	0.6244	0.6426

in the two datasets, with the null hypothesis that the two samples come from Gaussian distributions with equal means and unknown variances. The resultant p-values [95] are also reported in Table 4.1. In experimental sciences, as a rule of thumb, the null hypothesis is rejected when $p < 0.05$. As seen from Table 4.1, the p-value for both data sets is well above 0.05, which indicates that the two sets of AUC scores are statistically very similar, i.e., virtually indistinguishable.

To further compare the saliency maps produced by the proposed spatial approximation (4.7) with those produced by the original IKN model, we employed the Kullback-Leibler Divergence (KLD) [62]. For this purpose, we first normalized each saliency map so that it sums up to 1, and then considered the normalized map as a 2-D probability distribution. We then computed the average symmetric KLD between the two sets of normalized maps on both datasets. The symmetric KLD between two probability density functions $p_1(x)$ and $p_2(x)$ is defined as

$$KLD_{sym}(p_1(x)||p_2(x)) = \frac{1}{2}(KLD(p_1(x)||p_2(x)) + KLD(p_2(x)||p_1(x))), \tag{4.11}$$

where $KLD(p_1(x)||p_2(x))$ is the KLD between $p_1(x)$ and $p_2(x)$.

The average symmetric KLD on the Toronto data set was 0.01630, and it was 0.01355 on the MIT data set. Averaging these two, taking into account the number of images in each, the overall average symmetric KLD between the IKN saliency maps and our approximation was 0.0138.

In order to get a feeling for what symmetric KLD of 0.0138 between saliency maps means, we performed an experiment using JPEG coding and compared IKN saliency maps of the original and encoded images. For this purpose, we compressed the images in the two datasets with a JPEG encoder at various quality factors, and for each quality factor, we computed the average symmetric KLD between the normalized IKN saliency maps of the original images and the normalized IKN saliency maps of the compressed images. We also computed the average PSNR for each quality factor. We then repeated this experiment

until we got an average symmetric KLD of 0.0138. At this KLD, the average PSNR was about 40.2 dB. Therefore, one can say that the loss in accuracy in our approximation for spatial IKN saliency is comparable to that incurred in high-quality image compression that results in a PSNR of about 40.2 dB. Fig. 4.4 shows several sample images from the Toronto data set, their IKN saliency maps, as well as the saliency maps generated by the proposed spatial saliency approximation.

As a further illustration, we repeated the above experiment with a "naive" spatial saliency approximation that uses only five DCT coefficients

$$(j, l) \in \{(0, 1), (0, 2), (1, 1), (1, 0), (2, 0)\}$$

and sets their weight to 1 in (4.7), while setting the weight of other coefficients to zero. These coefficients correspond to the normalized frequency band $[\pi/256, \pi/16]$ of a 16×16 block. As shown in Fig. 4.3, these coefficients do end up with some of the highest Wiener weights, but this approach ignores spectral leakage, which is why we call it "naive." This "naive" method produces saliency maps with an average KLD of 0.0165 with respect to IKN maps, over the two datasets. Using the JPEG coding analogy above, the average KLD of 0.0165 corresponds to compression at 38.5 dB. Hence, although not as good as the Wiener-based approach, this "naive" method still performs reasonably well in terms of spatial saliency approximation.

We next assess the temporal saliency approximation together with spatial saliency approximation in the context of saliency estimation in video. Our complete approximation (the combination of temporal and spatial approximation) will henceforth be referred to as "IKN-A." In this test, the benchmark is the IKN model outfitted by a flicker and motion channel [67]. Table 4.2 compares the spatial IKN saliency against the approximation in (4.7), the temporal IKN saliency against the approximation in (4.8), as well as the full IKN saliency (with MaxNorm normalization [2], which we call it "IKN-MA" in the rest of our analysis) against the combined saliency approximation in (4.9) on ten standard CIF sequences at 30 frames per second (fps). As seen in the table, the average symmetric KLD between the spatial IKN saliency and our approximation is 0.0233, which corresponds to a PSNR of about 36.2 dB using the JPEG coding analogy above. The average symmetric KLD between the full saliency maps is 0.0174, corresponding to a PSNR of about 38.3 dB, which is thought to be a fairly decent quality.

Next, we compared the accuracy of IKN-A against IKN-MA using the AUC scores on

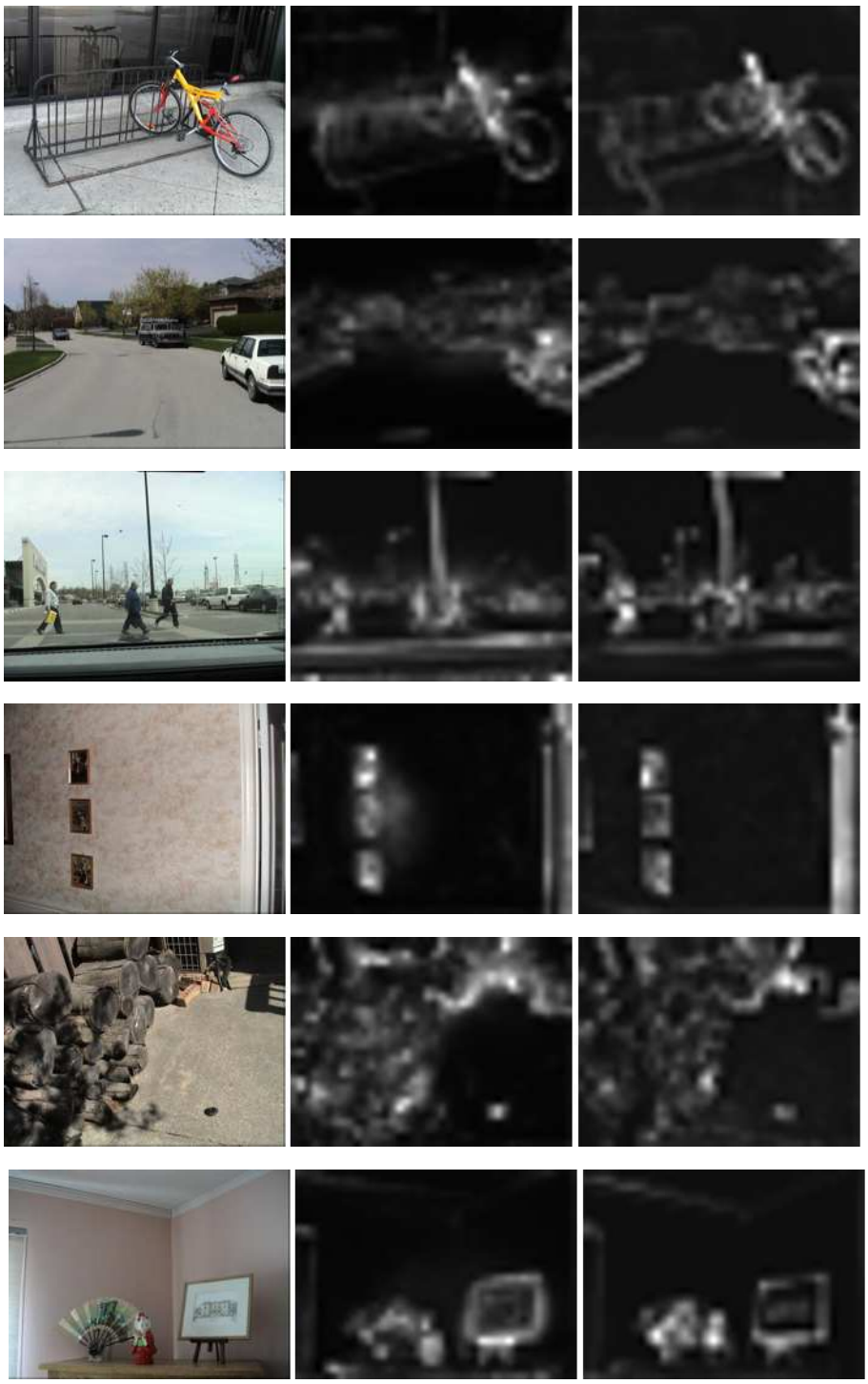

Figure 4.4: Sample images from the Toronto data set (left) along with their IKN saliency map (middle) and the saliency map generated by the proposed approximation (right).

the the video sequences from our dataset. The results for both viewings are shown in Table 4.3. As seen from these results, the average AUC scores of IKN-A are close to those of IKN-MA on both viewings. To check for the statistical significance, we performed a paired t-test between the AUC scores of the two models, with the null hypothesis that the AUC scores of the two models come from Gaussian distributions with equal means. The resulting p-values are also reported in Table 4.3. As seen from this table, for the first viewing, in 6 cases out of 12 cases, the p-values are larger than 0.05, indicating a statistical tie. In other cases, the accuracy of IKN-A is slightly lower than IKN-MA. The same situation holds for the second viewing as well. Fig. 4.5 shows the average ROC curves (across all videos) of the two models for both viewings. For the first viewing, the average AUC score of IKN-MA across all videos is about 0.6568 while the average AUC score of IKN-A is 0.6463. For the second viewing, the average AUC score of IKN-MA across all videos is about 0.6621 while that of IKN-A is 0.6504.

Finally, in addition to the KLD and AUC metrics, we also compared the saliency maps produced by IKN-MA with the saliency maps produced by IKN-A based on the average Mean Square Error (MSE). For this purpose, all saliency maps were normalized between 0 and 255, and the average MSE value across all videos was computed. The average MSE was about 51.53 on the sequences mentioned in Table 4.2, which is equivalent to a PSNR of about 31 dB.

According to the results reported in this section, we conclude that the accuracy of our proposed convex approximation to IKN saliency is satisfactory.

4.4.2 Evaluating GMC saliency estimation

In order to evaluate the performance of the global motion-compensated saliency estimation (GMC-S) from Section 4.3, we compared it against the spatio-temporal IKN model [67] on the eye-tracking dataset from Chapter 3. To generate the results for the IKN model, the original implementation of the IKN model [96] was utilized. Note that, as discussed in [67], in the original implementation of the IKN model for video, two main normalization operators are available for combining the conspicuity and feature maps: MaxNorm and FancyOne. MaxNorm yields smoother, more continuous saliency maps, while FancyOne yields increasingly sparser saliency maps, with only a few sharp peaks [67]. Since the saliency maps produced by MaxNorm are smoother than those of FancyOne, the MaxNorm operator is thought to be better suited to video compression [67]. However, FancyOne operator is

Table 4.2: Average symmetric KLD between the IKN saliency and our approximation on 12 standard CIF sequences.

Sequence	**Spatial Saliency**	**Temporal Saliency**	**Full Saliency**
Bus	0.0163	0.0198	0.0147
City	0.0144	0.0101	0.0115
Crew	0.0107	0.0095	0.0087
Foreman	0.0304	0.0110	0.0189
Flower Garden	0.0138	0.0192	0.0117
Hall Monitor	0.0293	0.0102	0.0189
Mother & Daughter	0.0142	0.0101	0.0120
Harbour	0.0389	0.0103	0.0243
Mobile Calendar	0.0184	0.0151	0.0146
Soccer	0.0162	0.0046	0.0106
Stefan	0.0477	0.0201	0.0301
Tempete	0.0294	0.0315	0.0333
Average	**0.0233**	**0.0143**	**0.0174**

Table 4.3: Average AUC score of IKN-MA and the proposed IKN approximation (IKN-A) on twelve standard video sequences.

Sequence	View-1			View-2		
	IKN-MA	IKN-A	p-value	IKN-MA	IKN-A	p-value
Bus	0.677901	0.749948	0.000000	0.642090	0.691229	0.000000
City	0.586142	0.570721	**0.065121**	0.587870	0.564346	**0.128152**
Crew	0.651511	0.658493	**0.153853**	0.655754	0.683478	0.000000
Foreman	0.642199	0.629129	**0.071223**	0.654281	0.646405	**0.054212**
Flower Garden	0.644158	0.628359	0.000000	0.676063	0.624593	0.000000
Hall Monitor	0.804911	0.763408	0.000000	0.816323	0.773894	0.000000
Harbor	0.537696	0.529202	**0.082716**	0.570529	0.566871	**0.192315**
Mobile Calendar	0.595226	0.599049	**0.497824**	0.599554	0.580717	**0.238125**
Mother & Daughter	0.660234	0.639038	0.000005	0.631714	0.628824	0.000000
Soccer	0.717283	0.684119	0.000000	0.707318	0.674214	0.000000
Stefan	0.716098	0.670241	0.000002	0.752651	0.716653	0.000000
Tempete	0.648412	0.633374	**0.056646**	0.650889	0.633327	**0.338122**

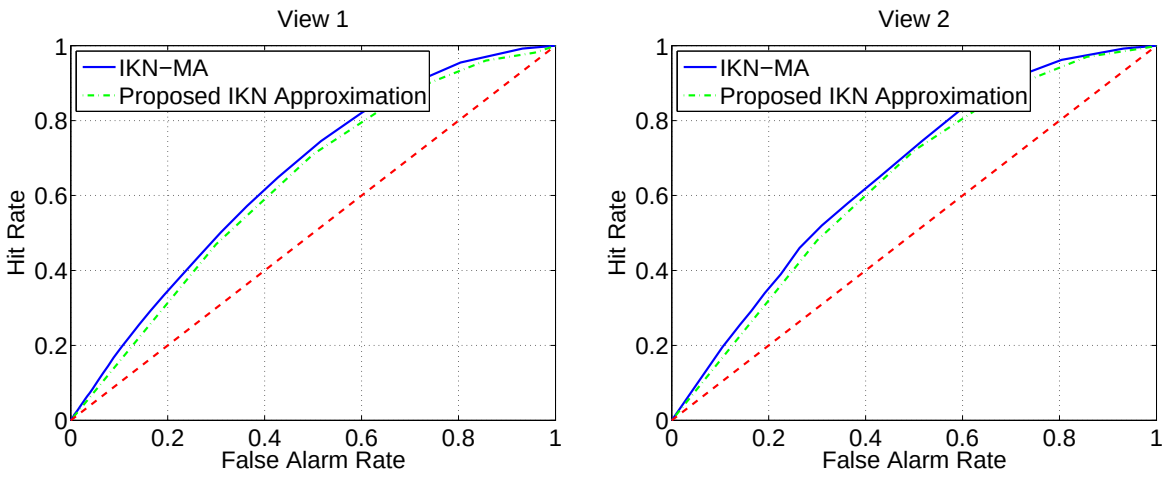

Figure 4.5: Average ROC curves of IKN-MA and the proposed IKN approximation (IKN-A) for the first viewing (left) and second viewing (right) of the 12 standard sequences in our eye-tracking dataset. The dashed diagonal line in the two figures shows an AUC score of 0.5, corresponding to pure chance.

more accurate in terms of gaze prediction; in fact, the spatio-temporal IKN model [67] with FancyOne feature integration is currently the most accurate publicly available gaze predictor for video, according to [92]. For the sake of simplicity in the rest of our analysis, we call the IKN model with the MaxNorm operator "IKN-MA," and the IKN model with FancyOne "IKN-FA."

Table 4.4 compares the proposed GMC saliency estimation method (GMC-S) with IKN-MA in terms of gaze prediction accuracy using the score defined in (3.2) for both viewings of each of the 12 test sequences. As seen from these results, in all cases the average accuracy score of our proposed method is higher than that of IKN-MA. To examine whether the difference in the average scores between IKN-MA and our method is statistically significant, we performed a paired t-test [78] on the frame-by-frame scores for each sequence and each viewing. The null hypothesis was that the scores of the two models come from the distributions with the same mean. Based on these results, we observe that the obtained p-values were less than 2×10^{-3}, except for *Crew* for both viewings, where the p-value was larger than 0.05. This means that in all cases except for *Crew*, the average accuracy score of the proposed GMC saliency estimation method was higher than IKN-MA, and these results were statistically significant due to a very small p-value. However, the average accuracy

Table 4.4: Comparing the proposed GMC saliency estimation method (GMC-S) with IKN-MA.

Video	*First Viewing*				*Second Viewing*			
	IKN-MA	GMC-S	p-value	Difference	IKN-MA	GMC-S	p-value	Difference
Bus	19.18	22.30	0.000006	+3.12	19.35	21.81	0.002081	+2.46
City	15.86	33.05	0.000000	+17.19	16.04	33.77	0.000000	+17.73
Crew	15.66	15.87	**0.323377**	+0.21	15.93	15.98	**0.775784**	+0.05
Foreman	20.05	22.71	0.000405	+2.66	19.99	23.67	0.000003	+3.68
Flower Garden	20.69	22.07	0.000000	+1.38	21.48	23.03	0.000000	+1.55
Hall Monitor	30.47	34.12	0.000245	+3.65	32.18	38.92	0.000000	+6.74
Harbor	18.83	21.27	0.001148	+2.44	19.37	22.06	0.000065	+2.69
Mobile Calendar	19.42	26.09	0.000000	+6.67	19.43	28.06	0.000000	+8.63
Mother & Daughter	15.51	16.78	0.000000	+1.27	16.03	17.06	0.000000	+1.03
Soccer	18.81	21.62	0.000000	+2.81	20.20	24.73	0.000000	+4.53
Stefan	21.07	23.97	0.007764	+2.90	18.67	23.05	0.000189	+4.38
Tempete	17.96	21.42	0.000000	+3.46	17.36	20.54	0.000000	+3.18

of the two models was statistically indistinguishable on *Crew*, at the 5% confidence level. Based on this data, we can claim that the proposed GMC saliency estimation method is more accurate than IKN-MA in terms of gaze prediction.

In order to compare the accuracy of our proposed GMC saliency estimation method with IKN-FA, we utilized the FancyOne normalization operator on all saliency maps produced by our GMC saliency estimation method. In other words, the saliency of each 16×16 block was first computed as in (4.10), and then similar to the IKN model, the FancyOne operator was applied on the resultant saliency maps to generate the final saliency maps for our method. We then performed the same analysis as in Table 4.4 based on the obtained saliency maps. The results are reported in Table 4.5. In this table, p-values larger than 0.05 have been indicated in bold typeset.

According to the results in Table 4.5, we observe that the performance of the proposed GMC saliency estimation method is statistically the same (at the 5% confidence level) as IKN-FA on *Bus* (for both viewings), *Crew* (for both viewings), *Flower Garden* (for the second viewing), *Harbor* (for both viewings), *Stefan* (for both viewings), and *Tempete* (for the second viewing). In these cases, the null hypothesis cannot be rejected because the corresponding p-values are larger than 0.05. In all other cases, the proposed GMC saliency estimation method outperforms IKN-FA except for the first viewing of *Flower Garden*, and both viewings of *Hall Monitor*, *Mobile Calendar*, and *Mother & Daughter*. Hence, one could argue that the proposed GMC saliency estimation method has comparable accuracy to IKN-FA in terms of gaze prediction.

Table 4.5: Comparing the proposed GMC saliency estimation method (GMC-S) with IKN-FA.

Video	*First Viewing*				*Second Viewing*			
	IKN-FA	GMC-S	p-value	Difference	IKN-FA	GMC-S	p-value	Difference
Bus	23.50	21.33	**0.161670**	−2.17	20.83	19.23	**0.365476**	−1.6
City	9.12	68.04	0.000000	+58.92	10.67	62.47	0.000000	+51.08
Crew	19.60	20.17	**0.598369**	+0.57	18.95	18.83	**0.891117**	−0.12
Foreman	28.99	38.40	0.000000	+9.41	30.01	41.62	0.000000	+11.61
Flower Garden	51.31	44.71	0.000000	−6.60	48.93	47.60	**0.371274**	−1.33
Hall Monitor	81.62	47.31	0.000000	−34.31	83.71	55.79	0.000000	−27.92
Harbor	31.12	33.14	**0.279229**	+2.02	36.81	34.29	**0.093973**	−2.52
Mobile Calendar	44.74	31.55	0.000000	−13.19	40.21	34.46	0.000708	−5.75
Mother & Daughter	32.63	18.60	0.000000	−14.03	35.13	17.84	0.000000	−17.29
Soccer	31.19	39.68	0.000000	+8.49	29.12	40.15	0.000000	+11.03
Stefan	67.42	73.92	**0.231836**	+6.50	66.91	73.50	**0.242396**	+6.59
Tempete	34.33	37.18	0.040270	+2.85	34.05	31.70	**0.086432**	−2.735

The study in [92] has evaluated nine publicly available saliency models on the dataset described in Chapter 3, which allows us to use the results from [92] in order to see how our GMC saliency estimation method (GMC-S) and our proposed IKN approximation (IKN-A) compare against these other models. Besides IKN-FA, the study in [92] included the following saliency models: Schauerte and Stiefelhagen [97], Harel *et al.* [38], Achanta and Susstrunk [85], Itti and Baldi [17], Goferman *et al.* [98], Fang *et al.* [99], Seo and Milanfar [100], and Kim *et al.* [101], For brevity, these models will henceforth be referred to as QDCT, GBVS, MSSS, IB, CA, QFTA, SR, WK, respectively.

The methodology employed in [92] was as follows. First, each model was applied to each of the sequences in the dataset, resulting in one saliency map per frame for each model. Then the score (3.2) was computed for each model in each frame using the gaze location data. The scores were analyzed using a multiple comparisons procedure known as the Tukey-Kramer test [102]. Specifically, for each sequence, the 95% confidence intervals for the mean score of each model was found. The top performing models were identified as those whose confidence intervals overlap that of model with the top mean score. Hence, for any sequence, there could be multiple models that are considered top performers.

The resulting mean scores are shown in Tables 4.6 and 4.7 for the first viewing and second viewing, respectively. The entries shown in bold indicate top performing models for each sequence. The ranking in terms of the number of appearances among top performers across both viewings is shown in Fig. 4.6. As seen from these results, out of 24 cases for the two viewings, both GMC-S and IKN-FA appeared 12 times among top performers. Also,

Table 4.6: Mean accuracy scores for several saliency estimation methods based on the first viewing in the eye-tracking dataset, with top scores indicated in bold.

Video	IKN-FA	QDCT	GBVS	MSSS	IB	CA	QFTA	SR	WK	GMC-S	IKN-A
Bus	23.50	22.35	23.20	15.54	15.77	24.02	19.32	16.44	25.21	21.33	**44.21**
City	9.12	15.17	23.49	15.58	13.39	18.15	18.70	10.19	10.57	**68.04**	16.01
Crew	19.60	20.88	23.16	19.40	16.16	21.20	19.04	13.06	21.63	20.17	**29.43**
Foreman	28.99	14.89	29.48	17.71	25.15	19.11	16.20	19.45	20.60	**38.40**	29.15
Flower Garden	**51.31**	20.04	27.86	20.31	19.35	19.03	18.40	19.94	17.70	32.55	30.08
Hall Monitor	**81.62**	21.82	33.98	30.42	59.35	21.95	17.03	39.82	**78.35**	47.31	39.83
Harbor	**31.12**	13.72	24.27	13.87	20.73	13.99	16.72	12.76	28.00	**33.14**	27.47
Mobile Calendar	**44.74**	14.84	25.30	12.72	21.40	13.77	10.94	30.16	18.31	31.55	39.67
Mother & Daughter	**32.63**	20.14	**29.93**	16.32	29.48	23.34	18.86	22.58	**33.25**	18.60	**33.98**
Soccer	31.19	23.34	26.96	25.44	23.04	24.62	21.43	22.01	20.61	**39.68**	**36.68**
Stefan	**67.42**	19.81	43.39	18.59	51.26	26.19	23.28	28.27	31.03	**73.92**	**70.31**
Tempete	34.33	21.46	24.20	25.64	28.02	24.55	15.39	17.24	10.32	**37.18**	28.64

Table 4.7: Mean accuracy scores for several saliency estimation methods based on the second viewing in our eye-tracking dataset, with top scores indicated in bold.

Video	IKN-FA	QDCT	GBVS	MSSS	IB	CA	QFTA	SR	WK	GMC-S	IKN-A
Bus	20.83	21.85	23.09	16.56	14.94	24.29	19.73	15.55	22.44	19.23	**35.53**
City	10.67	15.04	22.88	15.93	14.61	17.75	18.73	10.46	10.93	**62.47**	15.95
Crew	18.95	21.85	22.95	20.18	16.53	22.29	19.72	13.69	22.87	18.83	**33.40**
Foreman	30.01	15.04	29.79	17.85	24.50	19.42	16.37	20.07	20.85	**41.62**	30.05
Flower Garden	**48.93**	21.42	29.47	21.89	20.48	20.76	18.61	20.03	19.48	34.46	33.63
Hall Monitor	83.71	23.79	37.75	30.15	59.00	23.52	18.32	47.88	**91.66**	55.79	47.56
Harbor	**36.81**	14.14	23.86	13.90	23.71	13.75	16.38	13.83	31.66	**34.29**	27.79
Mobile Calendar	**40.21**	14.85	24.13	13.30	21.17	14.22	11.44	26.61	16.75	34.46	**37.02**
Mother & Daughter	**35.13**	20.00	30.10	15.86	30.96	23.70	19.26	23.23	**32.57**	17.84	**33.72**
Soccer	29.12	25.15	27.98	27.58	22.62	27.13	23.50	23.66	22.58	**40.15**	33.36
Stefan	**66.91**	19.47	40.78	17.03	48.69	25.98	22.17	27.39	30.55	**73.50**	**69.18**
Tempete	**34.05**	20.37	22.29	23.68	28.80	24.22	14.57	16.32	10.40	**31.70**	25.58

the proposed IKN-A appeared 10 times among top performers, and it ranks third in terms of the number of appearances among top performers, just behind IKN-FA and GMC-S.

We also compared the accuracy of the proposed GMC-S method against that of IKN-FA using the average AUC scores on our eye-tracking dataset. The results for both viewings are shown in Table 4.8. To check for the statistical significance, a t-test was performed with the null hypothesis that the AUC scores of the two models come from Gaussian distributions with equal means. The resulting p-values are also shown in this table. As seen from these results, GMC-S provides comparable results to IKN-FA in terms of the average AUC score metric in both viewings. All the obtained p-values are larger than 0.05, indicating statistical tie. The average ROC curves (across all sequences in the eye-tracking dataset) of the two models for both viewings are shown in Fig. 4.8. For the first viewing, the average AUC

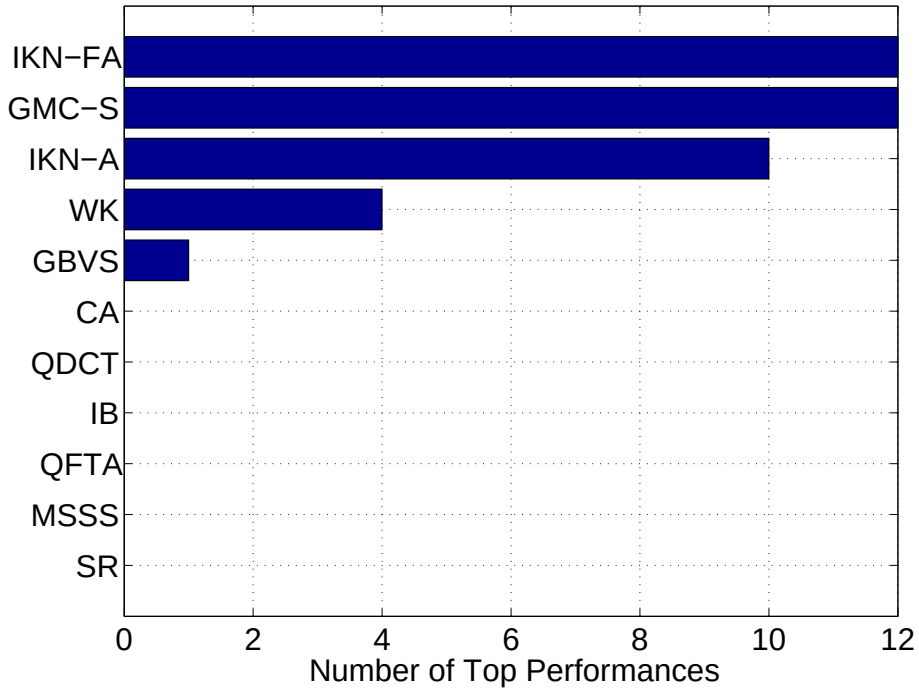

Figure 4.6: Model ranking based on the number of top performances.

score of IKN-FA across all videos is about 0.6586 while the average AUC score of GMC-S is 0.6461. For the second viewing, the average AUC score of IKN-FA across all videos is about 0.6599 while that of GMC-S is 0.6532.

Based on the results reported in this section, we observe that the proposed method has a higher accuracy score than IKN-FA on several sequences with camera motion such as *City*, *Soccer*, and *Tempete*, as may be expected based on its design. Fig. 4.7 shows an example. A frame from *City* is shown in this figure, along with the gaze locations from the dataset in Chapter 3, the corresponding saliency map generated by IKN-FA, and the one generated by the proposed GMC saliency estimation method. As seen in the figure, the proposed method is able to pinpoint the salient object more accurately than IKN-FA in this case.

4.5 Computational Complexity

Having assessed the accuracy of the our convex approximation to IKN saliency from Section 4.2 and the proposed GMC saliency estimation method from Section 4.3, we now analyze their computational complexity.

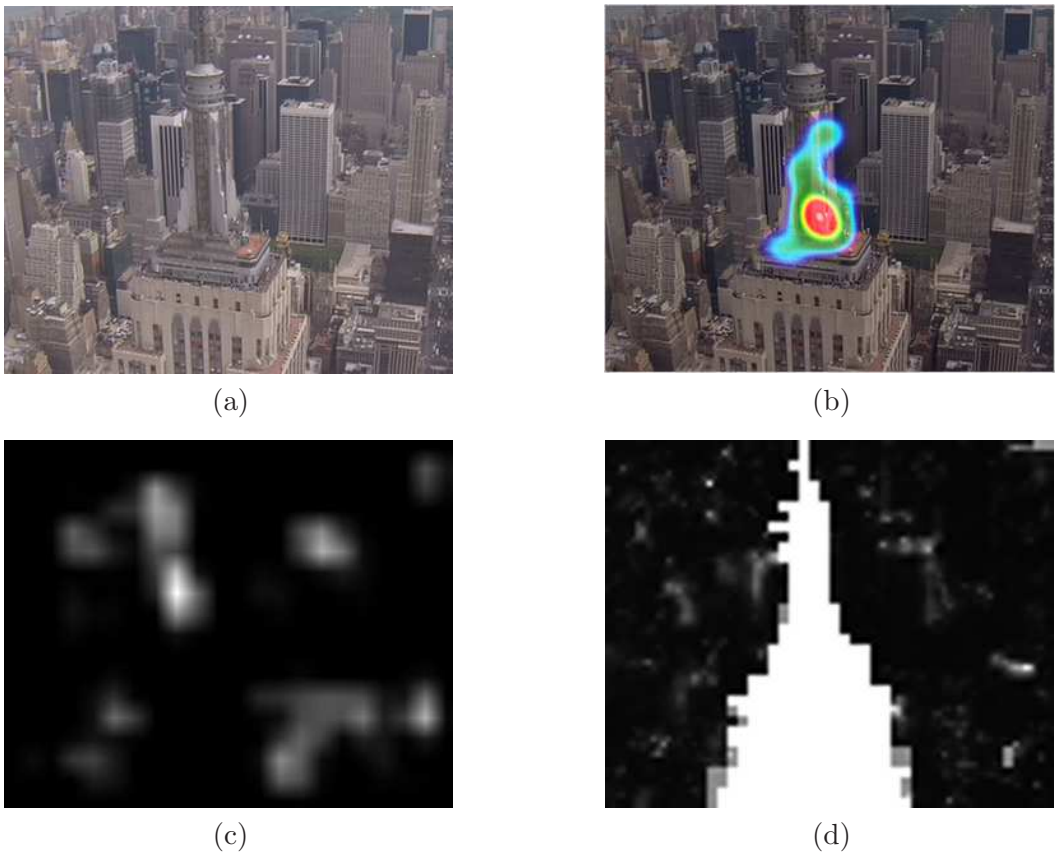

Figure 4.7: A frame from *City*: (a) original frame (b) heat map of the actual gaze locations (c) the saliency map generated by IKN-FA (d) the saliency map generated by the proposed GMC saliency detection method.

4.5.1 Complexity of the proposed convex approximation to IKN saliency

In this section, the computational complexity of our convex approximation to IKN saliency from Section 4.2 is estimated as the number of operations needed to produce the saliency map for one video frame. Note that by "operation" we mean operations such as addition/subtraction, multiplication/division, and absolute value computation.

Consider a video frame of size $W \times H$ pixels. To compute the saliency of a $N_b \times N_b$ block $\mathbf{X}$ based on (4.9), we need to compute both $\mathcal{S}_{spatial}(\mathbf{X})$ and $\mathcal{S}_{temporal}(\mathbf{X})$. The first step in computing $\mathcal{S}_{spatial}(\mathbf{X})$ is to compute the 2-D DCT of $\mathbf{X}$, which is of size $N_b \times N_b$. Note that the multiplication of a $A \times B$ matrix by a $B \times C$ matrix requires $A \cdot C \cdot (2B-1)$ operations, while computing the 2-D DCT of a $N_b \times N_b$ block requires two $N_b \times N_b$ matrix

Table 4.8: Comparing the proposed GMC saliency detection method (GMC-S) with IKN-FA based on mean AUC score.

Sequence	View-1			View-2		
	IKN-FA	GMC-S	p-value	IKN-FA	GMC-S	p-value
Bus	0.621949	0.594380	0.000085	0.594323	0.587702	0.000004
City	0.465959	0.704848	0.000000	0.468320	0.727083	0.000000
Crew	0.589822	0.580475	0.000000	0.558933	0.544043	0.000000
Foreman	0.651316	0.688162	0.000004	0.673088	0.682119	0.000000
Flower Garden	0.641450	0.598301	0.000005	0.645224	0.632190	0.000000
Hall Monitor	0.818588	0.655954	0.000002	0.814053	0.678976	0.000000
Harbor	0.603295	0.613706	0.000000	0.641240	0.638396	0.000000
Mobile Calendar	0.662766	0.583768	0.000000	0.675020	0.646586	0.000000
Mother & Daughter	0.662984	0.514667	0.000000	0.669394	0.498616	0.000000
Soccer	0.724149	0.737701	0.000000	0.691267	0.712680	0.000000
Stefan	0.786270	0.795846	0.000002	0.806129	0.812558	0.000008
Tempete	0.674131	0.685619	0.000000	0.682309	0.677392	0.000000

multiplications. Hence, if the 2-D DCT of $\mathbf{X}$ isn't already available in the video processing system, computing it requires $2N_b^2(2N_b - 1)$ operations.

We then need to compute the squares of the Wiener-filtered DCT coefficients, which requires $2N_b^2$ operations, and sum them up (4.7), which requires approximately N_b^2 operations. Hence, computing $\mathcal{S}_{spatial}(\mathbf{X})$ in one color channel requires approximately $N_b^2(4N_b+1)$ operations. For the common YUV 4:2:0 video format, the total computational cost for computing $\mathcal{S}_{spatial}(\mathbf{X})$ will be approximately $1.5(N_b^2(4N_b + 1))$.

To compute $\mathcal{S}_{temporal}(\mathbf{X})$, we first need to compute the absolute difference between $\mathbf{X}$ and the co-located $N_b \times N_b$ block in the previous frame in the luma (Y) channel. This step requires $2N_b^2$ operations. We then need to compute the 2-D DCT of the obtained residual block, which requires $2N_b^2(2N_b - 1)$ operations. After that we need to compute the sum of the squared Wiener-filtered DCT coefficients of the residual block (4.8), which requires approximately $2N_b^2 + N_b^2$ operations. Hence, computing $\mathcal{S}_{temporal}(\mathbf{X})$ requires approximately $N_b^2(4N_b + 3)$ operations. Overall, computing $\mathcal{S}(\mathbf{X})$ in (4.9) requires approximately $N_b^2(10N_b + 4.5) + 2$ operations.

According to the estimates obtained above, the number of operations needed by the proposed convex approximation for computing the saliency of all $N_b \times N_b$ blocks in a static image of size $W \times H$, without temporal saliency, would be

$$\zeta(CAS) \approx \frac{W \cdot H}{N_b \cdot N_b}(1.5(N_b^2(4N_b + 1))). \tag{4.12}$$

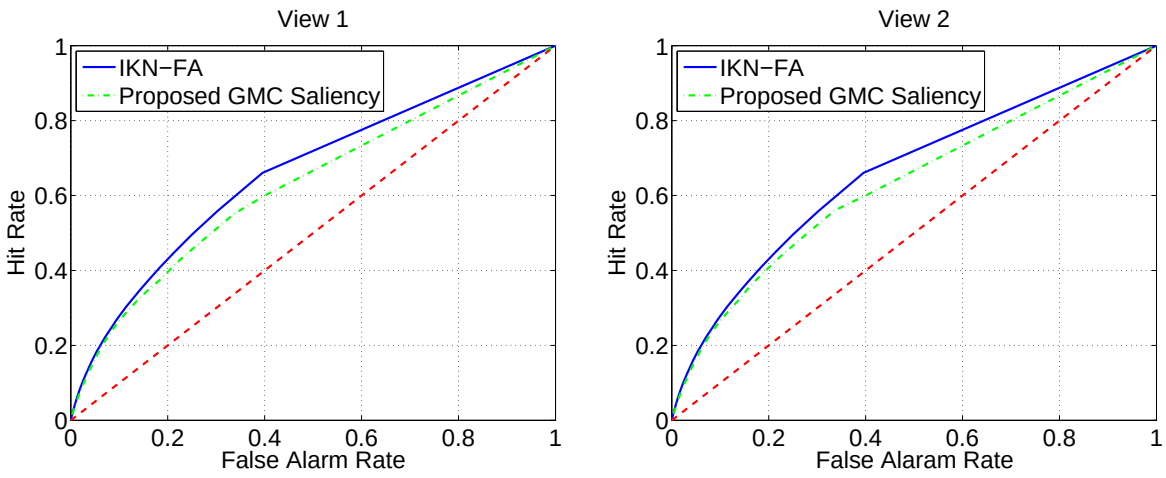

Figure 4.8: Average ROC curves of IKN-FA and the proposed GMC saliency detection method for the first viewing (left) and second viewing (right) of the 12 standard sequences in our eye-tracking dataset. The dashed diagonal line in the two figures shows an AUC score of 0.5, corresponding to pure chance.

The complexity of computing the saliency of all $N_b \times N_b$ blocks in a video frame of size $W \times H$, including the temporal saliency term, would be

$$\zeta(CAV) \approx \frac{W \cdot H}{N_b \cdot N_b}(N_b^2(10N_b + 4.5) + 2). \tag{4.13}$$

In our experiments, the block size was 16×16. Hence, $N_b = 16$, which gives $\zeta(CAS) \approx 98 \cdot W \cdot H$, and $\zeta(CAV) \approx 165 \cdot W \cdot H$.

Computational complexity of the IKN models for static images and video were studied in [103]. For a $W \times H$ image, saliency computation using the IKN model requires $\zeta(IKN) \approx 1119 \cdot W \cdot H$ operations. Comparing $\zeta(IKN)$ with $\zeta(CAS)$, we conclude that the complexity of our convex approximation for static images is about 1/11-th of the complexity of the IKN model. For a $W \times H$ video frame, taking motion and flicker into account, saliency computation according to the IKN model requires $\zeta(IKN_v) \approx 1539 \cdot W \cdot H$ operations [103]. Comparing $\zeta(CAV)$ with $\zeta(IKN_v)$ shows that our convex approximation to IKN saliency for video requires about 1/9-th of the complexity of the IKN model itself.

4.5.2 Complexity of the proposed GMC saliency estimation method

The GMC saliency estimation method was developed for video coding applications, as will be described in detail in Chapter 5. In such applications, motion estimation, which is a process of finding the best motion vector for each block, is performed for each predictively-encoded frame to achieve high compression effectiveness. Since motion estimation is performed in video coding anyway, the cost of estimating motion vectors is not included in the cost of GMC saliency estimation. We simply reuse the already-estimated motion vectors as an input to the GMC block.

We start with an estimate of the complexity of the global motion compensation (GMC) process. Although our GMC implementation is based on [14], we use the method from [104] as a representative GMC method for the purpose of estimating computational complexity, since its complexity is more tractable. In [104], motion model parameters $\mathbf{m}$ are estimated in an iterative process. Specifically, given a motion vector field with n motion vectors, the parameters $\mathbf{m}$ are estimated in each iteration as follows

$$\mathbf{m} = (\mathbf{\Omega}^t \mathbf{\Psi} \mathbf{\Omega})^{-1} \mathbf{\Omega}^t \mathbf{\Psi} \mathbf{V}, \tag{4.14}$$

where $\mathbf{\Omega}$ is a $2n \times 4$ matrix, $\mathbf{\Psi}$ is a diagonal $2n \times 2n$ matrix, $\mathbf{V}$ is a $2n \times 1$ vector, and $\mathbf{m}$ is a 4×1 vector. Since $\mathbf{\Psi}$ is diagonal, computing $\mathbf{\Omega}^t \mathbf{\Psi}$ requires $4 \cdot 2n = 8n$ operations. Given that the multiplication of a $A \times B$ matrix by a $B \times C$ matrix requires $A \cdot C \cdot (2B - 1)$ operations, computing $(\mathbf{\Omega}^t \mathbf{\Psi})\mathbf{V}$ needs $4(4n - 1)$ operations. We then need to compute $(\mathbf{\Omega}^t \mathbf{\Psi})\mathbf{\Omega}$, which needs $16(4n - 1)$ operations. A Singular Value Decomposition (SVD) [105] can be used to compute $(\mathbf{\Omega}^t \mathbf{\Psi} \mathbf{\Omega})^{-1}$. To compute the SVD of a $A \times B$ matrix, $4A^2B + 8AB^2 + 9B^3$ operations are needed [105]. The SVD results in three matrices by which we can compute the inverse of the matrix. Since $\mathbf{\Omega}^t \mathbf{\Psi} \mathbf{\Omega}$ is of size 4×4, it can be shown that the computation of $(\mathbf{\Omega}^t \mathbf{\Psi} \mathbf{\Omega})^{-1}$ requires $1344 + 2 \cdot (4 \cdot 4 \cdot (2 \cdot 4 - 1)) = 1568$ operations. Finally, we need to multiply $(\mathbf{\Omega}^t \mathbf{\Psi} \mathbf{\Omega})^{-1}$ by $\mathbf{\Omega}^t \mathbf{\Psi} \mathbf{V}$, which requires 28 operations. Thus, in total, computing $\mathbf{m}$ in each iteration requires $88n + 1576$ operations.

Within each iteration, we also need to compute a convergence error metric, which involves multiplying $\mathbf{\Omega}$ by the current $\mathbf{m}$ ($14n$ operations) and subtracting the result from a vector of size $2n \times 1$ containing the components of the n motion vectors ($2n$ operations), as well as the computation of the sum of the component-wise absolute differences of two $2n \times 1$ vectors ($4n + 2n = 6n$ operations). Hence, computing the convergence error metric

requires $14n + 2n + 6n = 22n$ operations. In total, $88n + 1576 + 22n = 110n + 1576$ operations are needed within each iteration of the GMC method [104] for obtaining $\mathbf{m}$. After obtaining the global motion parameters $\mathbf{m}$, we need to compute global motion vector within each 4×4 block. This can be achieved by multiplying $\mathbf{\Omega}$ by the obtained $\mathbf{m}$, which needs $14n$ operations. Finally, the global motion compensation is performed by subtracting the resulting global motion vectors from the existing motion vectors in the motion vector field. This needs $2n$ more operations. Thus, after obtaining $\mathbf{m}$, we need $16n$ operations for global motion compensation. In N_g iterations, the total number of operations is

$$\zeta(GMC) \approx (8n + 16n) + N_g(110n + 1576), \tag{4.15}$$

where we considered $4 \cdot 2n = 8n$ operations for computing $\mathbf{\Omega}^t$, which can be done outside the loop. In our experiments, we found that usually 20 iterations are enough to achieve convergence in the GMC process.

In our implementation, one motion vector was assigned to each 4×4 block in the frame. The motion saliency $\mathcal{S}_{motion}(\mathbf{X})$ of each 16×16 block is computed by taking the average magnitude of all global motion-compensated motion vectors of all 4×4 blocks within the 16×16 block. We need 4 operations to compute the magnitude of a 2-D motion vector. We also need 16 operations to compute the average magnitude of 16 motion vectors. Since there are sixteen 4×4 blocks within each 16×16 block, to compute the motion saliency of a 16×16 block, we need $16 \cdot 4 + 16 = 80$ operations. Based on the above estimates, the total number of operations for computing the motion saliency map of all 16×16 blocks in a $W \times H$ video frame is

$$\zeta(MS) \approx 80 \cdot \frac{W \cdot H}{16 \cdot 16} + (24n + N_g(110n + 1576)). \tag{4.16}$$

Given the above estimate of motion saliency complexity and using $N_g = 20$, the total number of operations required in (4.10) for a $W \times H$ video frame is as follows

$$\zeta(GMCS) \approx \zeta(CAS) + \zeta(MS) \approx 238 \cdot W \cdot H + 31520. \tag{4.17}$$

Comparing (4.17) with the complexity of the IKN model for video, which was found in [103] to be $\zeta(IKN_v) \approx 1539 \cdot W \cdot H$, shows that the complexity of our GMC saliency estimation method is considerably lower. For example, for CIF video resolution (352×288), we get $\zeta(IKN_v) \approx 6.457 \cdot \zeta(GMCS)$, while for HD resolution (1920×1080) we get $\zeta(IKN_v) \approx 6.466 \cdot \zeta(GMCS)$. Thus, the complexity of our GMC saliency estimation is about 1/6-th of the complexity of the IKN model for video.

4.6 Conclusions

In this chapter, we presented two computationally-efficient saliency estimation methods. The first one is a convex approximation to the IKN saliency model [67], which works solely in the DCT domain and has a low computational complexity. This makes it attractive for applications that involve convex optimization. Our experimental results indicated that the accuracy of the proposed approximation is close to the original IKN model. The second saliency estimation method proposed in this chapter uses global motion compensation prior to estimating motion-induced saliency. This method's performance is comparable to that of the IKN model, and better in certain sequences with camera motion.

Chapter 5

Saliency-Aware Video Compression

Lossy image and video encoders are known to produce undesirable compression artifacts at low bit rates [106],[107]. Blocking artifacts are the most common form of compression artifacts in block-based video compression. When coarse quantization is combined with motion-compensated prediction, blocking artifacts propagate from one frame into subsequent frames and accumulate, causing structured high-frequency noise or motion-compensated edge artifacts that may not be located at block boundaries, and so cannot be attenuated by deblocking filters that mostly operate on block boundaries [107]. Such visual artifacts may become very severe and attention-grabbing (salient), especially in low-textured regions.

Recently, region-of-interest (ROI) coding of video using computational models of visual attention [2] has been recognized as a promising approach to achieve high-performance video compression [5], [108], [72], [109]. The idea behind most of these methods is to encode an area around the predicted attention-grabbing (salient) regions with higher quality compared to other less visually important regions. Such a spatial prioritization is supported by the fact that only a small region of $2-5^{\circ}$ of visual angle around the center of gaze is perceived with high spatial resolution due to the highly non-uniform distribution of photoreceptors on the human retina [5].

Granting a higher priority to the salient regions, however, may produce visible coding artifacts in areas outside the salient regions where the image quality is lower. Such artifacts may draw viewer's attention away from the naturally salient regions, thereby degrading the perceived visual quality. It is worth pointing out that a visible artifact is not necessarily salient. A particular artifact may be visible if the user is looking directly at it or at its neighborhood, but may go unnoticed if the user is looking elsewhere in the frame. As

the severity of the artifact increases, it may become salient and draw user's attention. Although several methods have been developed for detecting visible (but not necessarily salient) artifacts [110], in our work, the concept of visual saliency is used to minimize salient coding artifacts, i.e., those coding artifacts that may grab user's attention.

In [16], we proposed a saliency-preserving framework for region-of-interest (ROI) video coding, whose main goal is to reduce attention-grabbing coding artifacts in non-ROI parts of the frame in order to keep viewer's attention on ROI parts where the video quality is higher. The method proposed in [16] was based on finding a quantization parameter (QP) matrix for each video frame so that the L_1-norm of the difference between the saliency map of the coded frame and the saliency map of the original raw frame is minimized under a given a target bit rate. In this method, the desired QP matrix is obtained after multiple encodings of each frame, which makes the process computationally expensive.

In this chapter, we extend our earlier work [16] in four ways. First, instead of using the computationally expensive IKN model [2], [67] to estimate saliency, as in [16], here we employ our global motion-compensated (GMC) saliency estimation method from Section 4.3. Second, we extend the conventional H.264/AVC rate-distortion optimization (RDO) [111] for video coding by introducing a saliency distortion term in the distortion metric. Unlike our earlier method [16], in the new method, the saliency of non-ROIs is allowed to decrease, and the saliency of ROIs is allowed to increase so long as the quality within ROIs is good. This enables higher flexibility in selecting coding parameters while producing visually pleasing results. Third, the complexity of the new method is significantly lower than that of our earlier method [16], which makes it more amenable for practical applications. This is a consequence of the fact that saliency estimation is performed by reusing some of the data from the coding process. Fourth, we evaluate the proposed method using several objective quality metrics, as well as an extensive subjective study, and compare its performance to two state-of-the-art perceptual video coding approaches.

The chapter is organized as follows. In Section 5.1, we present an overview of the rate distortion optimization in H.264/AVC video coding. The proposed video compression method is described in Section 5.2. Experimental results are presented in Section 5.3, followed by conclusions in Section 5.4.

5.1 Rate-distortion optimization in H.264/AVC

The H.264/AVC video coding standard supports various block coding modes such as INTER 16×16, INTER 16×8, INTER 8×16, INTER 8×8, INTRA 16×16, INTRA 4×4, and so on [111]. The coding mode specifies how prediction is performed (within the frame for INTRA, between frames for INTER) and determines the possible sizes of transform kernels employed on prediction residuals. The rate-distortion optimization (RDO) process proposed in H.264/AVC minimizes the following Lagrangian cost function for coding mode selection of each 16×16 macroblock (MB) [112, 111]:

$$J(\psi|Q, \lambda_R) = D_{MSE}(\psi|Q) + \lambda_R R(\psi|Q), \tag{5.1}$$

where Q is the quantization step size, $D_{MSE}(\psi|Q)$ and $R(\psi|Q)$ are, respectively, the Mean Squared Error (MSE) and bit rate for coding the current MB in the coding mode ψ with quantization step size Q, and λ_R is the Lagrange multiplier, which quantifies the trade-off between the rate and distortion [112]. The Lagrangian cost function (5.1) is minimized for a particular value of λ_R. Hence, λ_R has an important role in achieving optimal rate-distortion (RD) performance [112, 113]. In the H.264/AVC reference software [114], λ_R is computed as

$$\lambda_R = 0.85 \cdot 2^{\frac{(\mathrm{QP}-12)}{3}}, \tag{5.2}$$

where QP is the quantization parameter. The derivation of (5.2) was based on empirical results under a "high rate" assumption [115, 112, 113]. Although (5.2) provides a simple and effective method for finding λ_R, it has two main drawbacks. First, it is solely a function of QP, and so it does not consider any property of the input signal, which means that it does not adapt to the video content. Second, the high rate assumption does not hold at low bit rates [115], which threatens the optimality of (5.2) under such conditions.

In the literature, several methods have been proposed to obtain λ_R adaptively based on the video content when MSE is used as the distortion metric [115, 116, 117, 118]. Most such methods utilize RD models that are based on the distribution of transformed residuals. In particular, they use RD models that have a closed-form expression so that λ_R can be obtained in closed form. For instance, in [115], a Laplace distribution-based RD model was proposed to derive λ_R for each video frame adaptively based on the statistical properties of the transformed residuals. Several methods have shown that adjusting λ_R on the MB level results in better RD performance than λ_R adjustment on the frame level [118, 119, 120].

Many of the existing methods for RDO utilize the MSE or Sum of Absolute Differences (SAD) as a distortion metric, and they do not consider perceptual aspects. Recently, a number of RDO schemes have been proposed to consider several perceptual aspects of the Human Visual System (HVS). For instance, the authors in [121] proposed a motion-compensated residue signal pre-processing scheme based on just-noticeable-distortion (JND) profile for video compression. A foveated JND model was utilized in [122] for QP and Lagrange multiplier selection in which both the QP and the Lagrange multiplier are adjusted for each MB based on the visual noticeable distortion of the MB. Foveated imaging and image processing exploits the fact that the spatial resolution of the human visual system decreases significantly away from the gaze location (foveation point). By taking advantage of this fact, it is possible to remove significant high-frequency information redundancy from the peripheral regions around the gaze location and still obtain a perceptually good quality image. This way, large bit rate savings can be obtained in image/video compression. In [123], a real-time foveated multiresolution system for low-bandwidth video compression and transmission was proposed in which the gaze location was provided by a pointing device such as a mouse or an eye tracker. Another early work on the topic is [**?**]. In [83], a Foveal Weighted Signal to Noise (FWSNR) metric was proposed to take into account the non-uniform distribution of photoreceptors on the retina when computing SNR. Such a metric can be utilized within a foveated image/video compression framework. In [124], an embedded foveation image coding (EFIC) algorithm was proposed, which orders the encoded bitstream to optimize foveated visual quality at arbitrary bit rates. In [125], a foveation scalable video coding (FSVC) algorithm was proposed, which supplies good quality-compression performance as well as effective rate scalability. The key idea behind this method is to organize the encoded bitstream to provide the best decoded video at an arbitrary bit rate in terms of foveated visual quality.

Several methods employed the Structural Similarity Index Metric (SSIM) [126] for video coding and RDO [127, 128, 129, 130]. In [130], the authors utilized SSIM [126] as the distortion metric within the RDO process. They also presented an adaptive Lagrange multiplier selection scheme based on a novel statistical reduced-reference SSIM model and a source-side information combined rate model. Moreover, they proposed a method to adjust the Lagrange multiplier for each MB based on the motion information content and perceptual uncertainty of visual speed perception. In [131], the authors also employed the SSIM as the distortion metric, and weighted the SSIM distortion using the visual saliency of various

MBs, with the idea that the perception of distortions is stronger in more salient regions.

5.2 Saliency-aware video compression

The proposed saliency-aware video compression is based on the following principles:

1. Highly salient regions should end up with higher perceptual quality than less salient regions. This means that quality is directed towards the regions that viewers are likely to look at.

2. The coding should attempt to preserve the saliency of various regions, except in the following two cases:

   - If a region is highly salient, then its saliency is allowed to increase after compression, provided the quality remains sufficiently high. The reasoning here is that we don't mind viewers being even more drawn to high-quality regions in the scene.
   - If a region has low saliency to start with, then its saliency is allowed to decrease after compression. The logic here is that low-saliency regions will end up with lower quality, so the less likely the viewer is to look at such regions, the better.

In the remainder of this section, we present procedures for selecting the quantization parameter (QP), the Lagrange multipliers, and the optimal coding mode, to satisfy the above principles. For each MB in the frame, the QP is assigned first based on MB's saliency, followed by Lagrange multiplier selection and coding mode decision.

5.2.1 Macroblock QP selection

Let QP_f be the quantization parameter of the current video frame, which is provided by an appropriate frame-level rate control algorithm, e.g. [132, 133, 134]. Let $\mathcal{S}_{gmc}(\mathbf{X}_i)$ be the GMC saliency (4.10) of the i-th MB $\mathbf{X}_i$. Also, let $\bar{s}$ be the average GMC-saliency of all MBs in the current frame. Following the method from [122], the QP for the i-th MB in the current frame is obtained as

$$\mathrm{QP}_i = round\left(\frac{\mathrm{QP}_f}{\sqrt{w_i}}\right), \tag{5.3}$$

where w_i is obtained through a sigmoid function

$$w_i = a + \frac{b}{1 + \exp(-c(\mathcal{S}_{gmc}(\mathbf{X}_i) - \bar{s})/\bar{s})}, \tag{5.4}$$

and a, b, and c are constants. In our experiments similar to [122], we set $a = 0.7$, $b = 0.6$, and $c = 4$.

Note that (5.3) gives the QP of $\mathbf{X}_i$. In H.264/AVC, the relation between QP and the quantization step size Q is

$$Q = 2^{\mathrm{QP}/6} \cdot \nu(\mathrm{QP} \bmod 6),$$

where $\nu(0) = 0.675$, $\nu(1) = 0.6875$, $\nu(2) = 0.8125$, $\nu(3) = 0.875$, $\nu(4) = 1.0$, and $\nu(5) = 1.125$ [111].

5.2.2 RDO mode decision

In addition to the conventional rate and distortion terms commonly used in the Lagrangian cost function, we introduce a saliency distortion term $D_{sal}(\psi|Q_i, \mathbf{X}_i)$ in order to obtain the optimal coding mode according to the principles outlined above. For the i-th MB, the proposed cost function is

$$J_i(\psi|Q_i, \lambda_{S_i}, \lambda_{R_i}, \mathbf{X}_i) = D_{MSE}(\psi|Q_i, \mathbf{X}_i) + \lambda_{S_i} D_{sal}(\psi|Q_i, \mathbf{X}_i) + \lambda_{R_i} R(\psi|Q_i, \mathbf{X}_i), \tag{5.5}$$

where λ_{S_i} is the Lagrangian multiplier associated with saliency distortion $D_{sal}(\psi|Q_i, \mathbf{X}_i)$. The saliency distortion is defined as the absolute difference between the GMC saliency (4.10) of the uncompressed i-th MB and that of the i-th MB coded using coding mode ψ with quantization step size Q_i, that is,

$$D_{sal}(\psi|Q_i, \mathbf{X}_i) = |\mathcal{S}_{gmc}(\mathbf{X}_i) - \mathcal{S}_{gmc}(\widetilde{\mathbf{X}}_i(\psi|Q_i))|, \tag{5.6}$$

where $\mathbf{X}_i$ is the uncompressed i-th MB and $\widetilde{\mathbf{X}}_i(\psi|Q_i)$ denotes the i-th MB coded using coding mode ψ with quantization step size Q_i.

We note that compression generally does not change the direction or magnitude of motion of various regions, except possibly at extremely low bitrates. We will therefore assume that the change in motion saliency in (4.10) due to compression is negligible compared to the change in spatial saliency. Hence, using (4.10), $D_{sal}(\psi|Q_i, \mathbf{X}_i)$ can be approximated as

$$D_{sal}(\psi|Q_i, \mathbf{X}_i) = \mu_i \cdot |\mathcal{S}_{spatial}(\mathbf{X}_i) - \mathcal{S}_{spatial}(\widetilde{\mathbf{X}}_i(\psi|Q_i))|, \tag{5.7}$$

where $\mathcal{S}_{spatial}(\mathbf{X}_i)$ is the spatial saliency of $\mathbf{X}_i$, computed based on (4.7), and

$$\mu_i = 1 - \alpha + \beta \mathcal{S}_{motion}(\mathbf{X}_i), \tag{5.8}$$

where $\mathcal{S}_{motion}(\mathbf{X}_i)$ is the motion saliency of $\mathbf{X}_i$, which can be computed using the method described in Section 4.3.

Equations (5.7)-(5.8) suggest that the saliency distortion for a MB is the spatial saliency distortion weighted by the motion saliency of the MB. Hence, other things being equal, the saliency distortion is expected to be larger in regions where the motion saliency is higher.

According to the principles outlined at the beginning of this section, the saliency of highly salient regions (ROIs) is allowed to increase after compression, if the quality of such regions after compression is good. This condition can be characterized by

$$\text{Condition A} = \begin{cases} \mathbf{X}_i \in \text{ROI}, \quad \text{and} \\ \mathcal{S}_{spatial}(\mathbf{X}_i) < \mathcal{S}_{spatial}(\widetilde{\mathbf{X}}_i(\psi|Q_i)), \quad \text{and} \\ D_{MSE}(\psi|Q_i, \mathbf{X}_i) < \delta, \end{cases}$$

where δ is a user-defined threshold. Also, the saliency of low-salient regions (non-ROIs) is allowed to decrease after compression. Such condition is characterized by

$$\text{Condition B} = \begin{cases} \mathbf{X}_i \in \text{non-ROI}, \quad \text{and} \\ \mathcal{S}_{spatial}(\mathbf{X}_i) > \mathcal{S}_{spatial}(\widetilde{\mathbf{X}}_i(\psi|Q_i)). \end{cases}$$

If either of these two conditions holds, we set the saliency-related Lagrange multiplier λ_{S_i} to zero:

$$\lambda_{S_i} = \begin{cases} 0, & \text{if Condition A or B holds,} \\ \lambda_S, & \text{otherwise,} \end{cases} \tag{5.9}$$

where λ_S is a user-defined parameter. In our experiments, we set $\lambda_S = 1.5$. This means that the saliency distortion term will be ignored in the cost function (5.5) if either Condition A or B holds. Hence, in such cases, the coding mode will be chosen by considering conventional rate and distortion only, while the saliency will be allowed to change in the desired direction: increase in ROI, and decrease in non-ROI.

We next discuss the choice of λ_{R_i}. From (5.5), λ_{R_i} can be obtained by calculating the partial derivative of J_i with respect to R, then setting it to zero, and finally solving for λ_{R_i}.

More specifically, we need to have

$$\begin{aligned}&\frac{\partial J_i(\psi|Q_i,\lambda_{S_i},\lambda_{R_i},\mathbf{X}_i)}{\partial R(\psi|Q_i,\mathbf{X}_i)}\\&=\frac{\partial D_{MSE}(\psi|Q_i,\mathbf{X}_i)}{\partial R(\psi|Q_i,\mathbf{X}_i)}+\lambda_{S_i}\frac{\partial D_{sal}(\psi|Q_i,\mathbf{X}_i)}{\partial R(\psi|Q_i,\mathbf{X}_i)}+\lambda_{R_i}\\&=0.\end{aligned}\tag{5.10}$$

Solving for λ_{R_i} gives

$$\lambda_{R_i}=-\frac{\partial D_{MSE}(\psi|Q_i,\mathbf{X}_i)}{\partial R(\psi|Q_i,\mathbf{X}_i)}-\lambda_{S_i}\frac{\partial D_{sal}(\psi|Q_i,\mathbf{X}_i)}{\partial R(\psi|Q_i,\mathbf{X}_i)}.\tag{5.11}$$

With Lagrange multipliers set according to (5.9) and (5.11), the encoder can choose the optimal coding mode ψ for $\mathbf{X}_i$. We next derive a closed-form expression for λ_{R_i} for the case when the transformed residual of $\mathbf{X}_i$ obeys a Laplacian model.

5.2.3 Statistical modeling of transformed residuals

Following [135], we model the marginal density of transformed residuals Y by a zero-mean Laplace probability density function with parameter λ,

$$f_Y(y;\lambda)=\frac{\lambda}{2}e^{-\lambda|y|}.\tag{5.12}$$

The relationship between λ and standard deviation σ_Y is

$$\lambda=\frac{\sqrt{2}}{\sigma_Y}.\tag{5.13}$$

To describe the correlation structure of the signal, we adopt a separable autocorrelation function $r_i(m,n)=\sigma_{r_i}^2\rho_i^{|m|}\rho_i^{|n|}$, where m and n are the horizontal and vertical distances between samples, respectively, $\sigma_{r_i}^2$ is the variance of the residual signal of MB $\mathbf{X}_i$ before transformation, and ρ_i is the correlation coefficient of the residual signal of MB $\mathbf{X}_i$, assumed to be equal in horizontal and vertical directions. This model is thought to be a good model for natural digital images [136]. Using such a model, the variance of the (j,l)-th transform coefficient obtained under coding mode ψ can be obtained as follows [137, 106, 136]

$$\sigma_{Y_i}^2(j,l)=\sigma_{r_i}^2[\mathbf{A}(\psi)\mathbf{K}_i(\psi)\mathbf{A}(\psi)^T]_{j,j}[\mathbf{A}(\psi)\mathbf{K}_i(\psi)\mathbf{A}(\psi)^T]_{l,l},\tag{5.14}$$

where $\mathbf{A}(\psi)$ is the $N \times N$ transform matrix for the coding mode ψ and $\mathbf{K}_i(\psi)$ is the $N \times N$ covariance matrix

$$\mathbf{K}_i(\psi) = \begin{bmatrix} 1 & \rho_i & \rho_i^2 & \cdots & \rho_i^{N-1} \\ \rho_i & 1 & & & \\ \rho_i^2 & & \ddots & & \vdots \\ \vdots & & & & \rho_i \\ \rho_i^{N-1} & & \cdots & \rho_i & 1 \end{bmatrix}. \tag{5.15}$$

In (5.14), notation $[.]_{j,j}$ means the (j,j)-th element of the matrix. Hence, according to the adopted model, the (j,l)-th transform coefficient of the residual of $\mathbf{X}_i$ is a Laplacian random variable with parameter

$$\lambda_i^{jl} = \frac{\sqrt{2}}{\sigma_{Y_i}(j,l)}. \tag{5.16}$$

Note that the correlation coefficient ρ_i and variance $\sigma_{r_i}^2$ are estimated from the residual signal of MB $\mathbf{X}_i$ for each i. Hence, the model is adapted locally to the data.

5.2.4 The rate model

The rate of MB $\mathbf{X}_i$ is obtained from the entropy of its quantized transformed residual. The entropy of the (j,l)-th coefficient is given by

$$h_i(j,l) = -p_{i_0}(j,l)\log_2 p_{i_0}(j,l) - 2\sum_{n=1}^{\infty} p_{i_n}(j,l)\log_2 p_{i_n}(j,l), \tag{5.17}$$

where p_{i_0} and p_{i_n} are the probabilities of transformed residuals being quantized to the zeroth and n-th quantization levels, respectively, and can be obtained as

$$p_{i_0}(j,l) = \int_{-(Q_i-\gamma Q_i)}^{(Q_i+\gamma Q_i)} f_{\lambda_i^{jl}}(x)dx, \tag{5.18}$$

$$p_{i_n}(j,l) = \int_{nQ_i-\gamma Q_i}^{(n+1)Q_i-\gamma Q_i} f_{\lambda_i^{jl}}(x)dx, \tag{5.19}$$

where Q_i is the quantization step size of $\mathbf{X}_i$, and $F_i = \gamma Q_i$ denotes the rounding offset of the quantizer with $\gamma \in (0,1)$. In H.264/AVC, $\gamma = 1/6$ for inter frames and $\gamma = 1/3$ for intra

frames [115, 114]. The total rate of MB $\mathbf{X}_i$ coded under coding mode ψ with quantization step size Q_i can be estimated from the sum of entropies of individual transform coefficients

$$R(\psi|Q_i, \mathbf{X}_i) = \zeta \sum_{(j,l)} h_i(j,l), \tag{5.20}$$

where ζ is a factor to compensate for the inaccuracies in the model. For example, the transform coefficients are assumed to be correlated in Section 5.2.3, which will result in a lower rate than the sum of their individual entropies. Hence, we expect $\zeta < 1$. In our experiments, we set $\zeta = 0.8$.

In order to simplify subsequent equations, we define the following symbols for commonly used quantities:

$$\begin{aligned}
\nu_i^{jl} &= \lambda_i^{jl} Q_i \\
\phi_i^{jl} &= e^{-\nu_i^{jl}} - 1 \\
\xi_i^{jl} &= e^{\lambda_i^{jl}(F_i - Q_i)} \\
\psi_i^{jl} &= e^{\nu_i^{jl}} \\
\kappa_i^{jl} &= (\lambda_i^{jl})^2 Q_i F_i \\
\theta_i^{jl} &= \lambda_i^{jl} \xi_i^{jl} \\
\eta_i^{jl} &= 1 - e^{\lambda_i^{jl}(F_i - Q_i)}.
\end{aligned} \tag{5.21}$$

Substituting (5.17)-(5.19) into (5.20), using (5.21), we obtain a closed-form expression for the rate of $\mathbf{X}_i$ in (5.22).

$$R(\psi|Q_i, \mathbf{X}_i) = -\frac{\zeta}{\ln 2} \sum_{(j,l)} \left(\xi_i^{jl} \Big(\ln(-\phi_i^{jl}) - \ln 2 + F_i \lambda_i^{jl} + \frac{\nu_i^{jl}}{\phi_i^{jl}} \Big) + \eta_i^{jl} \ln(\eta_i^{jl}) \right). \tag{5.22}$$

5.2.5 The distortion models

The total MSE distortion in $\mathbf{X}_i$ is the sum of quantization distortions contributed by individual transform coefficients:

$$\begin{aligned}
D_{MSE}(\psi|Q_i, \mathbf{X}_i) = \sum_{(j,l)} \Big(& \int_{-(Q_i - \gamma Q_i)}^{(Q_i + \gamma Q_i)} x^2 f_{\lambda_i^{jl}}(x) dx \\
& + 2 \sum_{n=1}^{\infty} \int_{nQ_i - \gamma Q_i}^{(n+1)Q_i - \gamma Q_i} (x - nQ_i)^2 f_{\lambda_i^{jl}}(x) dx \Big).
\end{aligned} \tag{5.23}$$

After some algebraic manipulation, $D_{MSE}(\psi|Q_i, \mathbf{X}_i)$ can be expressed in the closed form as

$$D_{MSE}(\psi|Q_i, \mathbf{X}_i) = \sum_{(j,l)} \chi_i^{jl} = \sum_{(j,l)} \frac{e^{\lambda_i^{jl} F_i}(2\nu_i^{jl} + (\nu_i^{jl})^2 - 2\kappa_i^{jl}) + 2 - 2\psi_i^{jl}}{-\phi_i^{jl}(\lambda_i^{jl})^2}. \tag{5.24}$$

Based on (5.7), the saliency distortion of a MB is proportional to the spatial saliency distortion of the MB weighted by the motion saliency of the MB. As described in Section 4.2, our approximation to the spatial saliency of a MB is the power of the Wiener-filtered DCT of the MB. In order to estimate the spatial saliency distortion of a block due to quantization, we model the quantization process by an equivalent quantization noise [138], and consider the Wiener-weighted energy of the quantization noise in the DCT domain as our spatial saliency distortion. More specifically, we consider the following expression as a model for $D_{sal}(\psi|Q_i, \mathbf{X}_i)$.

$$D_{sal}(\psi|Q_i, \mathbf{X}_i) = \mu_i \sum_{(j,l)} \mathbf{H}(j,l)\chi_i^{jl}, \tag{5.25}$$

where χ_i^{jl} is as defined in (5.24).

5.2.6 A closed-form expression for λ_{R_i}

From the expressions for $R(\psi|Q_i, \mathbf{X}_i)$, $D_{MSE}(\psi|Q_i, \mathbf{X}_i)$ and $D_{sal}(\psi|Q_i, \mathbf{X}_i)$, we can obtain the expression for λ_{R_i}. To do this, using the chain rule, we express the ratios in (5.11) in terms of partial derivatives with respect to Q_i,

$$\lambda_{R_i} = -\frac{\frac{\partial}{\partial Q_i}(D_{MSE}(\psi|Q_i, \mathbf{X}_i) + \lambda_{S_i} D_{sal}(\psi|Q_i, \mathbf{X}_i))}{\frac{\partial}{\partial Q_i} R(\psi|Q_i, \mathbf{X}_i)}, \tag{5.26}$$

where the numerator is given in (5.27), and the denominator is given in (5.28).

$$\begin{aligned}
&\frac{\partial}{\partial Q_i}(D_{MSE}(\psi|Q_i, \mathbf{X}_i) + \lambda_{S_i} D_{sal}(\psi|Q_i, \mathbf{X}_i)) \\
&= \sum_{(j,l)} (1 + \mu_i \lambda_s \mathbf{H}(j,l)) \Bigg(\frac{2\lambda_i^{jl}\nu_i^{jl} - e^{F_i\lambda_i^{jl}}\left(2\lambda_i^{jl} - 2F_i(\lambda_i^{jl})^2 + 2(\lambda_i^{jl})^2 Q_i\right)}{(\lambda_i^{jl})^2(\psi_i^{jl} - 1)} + \\
&\qquad \frac{\psi_i^{jl}\left(e^{F_i\lambda_i^{jl}}\left((\nu_i^{jl})^2 - 2F_i(\lambda_i^{jl})^2 Q_i + 2\lambda_i^{jl} Q_i\right) - 2\nu_i^{jl} + 2\right)}{\lambda_i^{jl}(\psi_i^{jl} - 1)^2} \Bigg).
\end{aligned} \tag{5.27}$$

$$\frac{\partial R(\psi|Q_i,\mathbf{X}_i)}{\partial Q_i} = \frac{-\zeta}{\ln 2}\sum_{(j,l)}\theta_i^{jl}\Bigg(1+\Big(\frac{\lambda_i^{jl}}{\phi_i^{jl}}-\frac{\lambda_i^{jl}}{\psi_i^{jl}\phi_i^{jl}}+\frac{(\lambda_i^{jl})^2 Q_i}{\psi_i^{jl}(\phi_i^{jl})^2}\Big)+\ln(-\phi_i^{jl})- \Big(\ln(-\phi_i^{jl})-\ln 2+F_i\lambda_i^{jl}+\frac{\nu_i^{jl}}{\phi_i^{jl}}\Big)\Bigg). \tag{5.28}$$

Note that several quantities, such as ν_i^{jl} and λ_i^{jl}, appear in both (5.27) and (5.28), which means that computational effort can be reduced by computing these quantities only once. In our implementation, we first compute (5.27), and values of the quantities that are shared with (5.28) are reused.

It is worth pointing out that λ_{R_i} in (5.26) depends on the content of each MB through the variance and correlation of the residual of MB $\mathbf{X}_i$, as well as the motion and spatial saliency of $\mathbf{X}_i$, based on (5.7). Hence, using (5.26), we can adjust the Lagrange multiplier in a content-adaptive manner on a MB-by-MB basis.

5.3 Experimental results

5.3.1 Objective quality assessment

In order to objectively compare the perceptual quality of video produced by the proposed saliency-aware video compression method versus that of other methods, we used the eye-tracking-weighted Mean Square Error (EWMSE) metric proposed in [72]. The EWMSE value of an encoded video frame can be computed as follows [72]

$$\text{EWMSE} = \frac{\sum_{x=1}^{W}\sum_{y=1}^{H}\left(w_{x,y}\cdot(F'_{x,y}-F_{x,y})^2\right)}{WH\sum_{x=1}^{W}\sum_{y=1}^{H}w_{x,y}}, \tag{5.29}$$

where $F'_{x,y}$ and $F_{x,y}$ respectively denote the pixel at location (x,y) in the encoded frame $\mathbf{F}'$ and the original frame $\mathbf{F}$, W and H are the width and height of $\mathbf{F}$ in pixels, and $w_{x,y}$ is the weight for distortion at pixel location (x,y), obtained using the following 2-D Gaussian function

$$w_{x,y} = \frac{1}{2\pi\sigma_x\sigma_y G}\sum_{g=1}^{G}\exp\left\{-\left(\frac{(x-x_{p_g})^2}{2\sigma_x^2}+\frac{(y-y_{p_g})^2}{2\sigma_y^2}\right)\right\}, \tag{5.30}$$

where (x_{p_g}, y_{p_g}) is the eye fixation position of the g-th subject. We used eye fixation data from our database in Chapter 3, where the total number of subjects is $G = 15$. In (5.30), σ_x

and σ_y are two parameters that specify the width of the Gaussian function, and they depend on the viewing distance and viewing angle. The values of σ_x and σ_y can be taken based on the fovea size, which is about $2-5^\circ$ of visual angle [12], [72]. Here, similar to [12], [72], we use $\sigma_x = \sigma_y = 64$ pixels, which is equivalent to 2° of the visual angle. Using the EWMSE metric given by (5.29), the eye-tracking-weighted PSNR (EWPSNR) in dB is defined as

$$\text{EWPSNR} = 10 \log \left(\frac{255^2}{\text{EWMSE}} \right). \tag{5.31}$$

In our experiments, the average EWPSNR across all frames is considered as one measure of the perceptual quality of the video - the higher the EWPSNR, the higher the quality of the encoded video.

In order to evaluate the proposed saliency-aware video compression method, we compared its EWPSNR performance at several bit rates with the conventional RDO method implemented in the H.264/AVC reference software JM 16.1 [114], as well as two recent ROI-coding methods: the FJND method proposed in [122] and the visual attention guided bit allocation (VAGBA) method proposed in [72]. The comparison was made on the 12 sequences from our database in Chapter 3. Higher average EWPSNR is expected if, on average, the predictions of highly salient regions are closer to the actual human fixation points. To compute the EWPSNR values, we used the luma (Y) pixel values and the eye-tracking data of the first viewing in our eye-tracking database.

All videos were encoded by each of the aforementioned methods at different bit rates with a GOP structure of IPPP. To encode a video at different bit rates, we varied the frame-level QP (QP_f) of the video between 25 to 40, and at each value, we computed the average EWPSNR and PSNR of the encoded video. Two sample sets of results, for *Foreman* and *Tempete*, are shown in Fig. 5.1 and 5.2, respectively. In these figures, EWPSNR is plotted against the bit rate. In these experiments, FJND and VAGBA used IKN-FA saliency maps, while the proposed saliency-aware coding method used the saliency maps produced by our GMC saliency estimation method from Section 4.3. As seen in the figures, the proposed method achieves higher EWPSNR than the other three methods across a range of bit rates.

In the next set of results, we utilized the Bjontegaard Delta (BD) method [139] to measure the average difference between rate-distortion (RD) curves. We applied this procedure on both EWPSNR and PSNR curves. To be able to compare the performance of various methods, we considered the conventional RDO method as the baseline and computed the average difference of various metrics relative to this baseline.

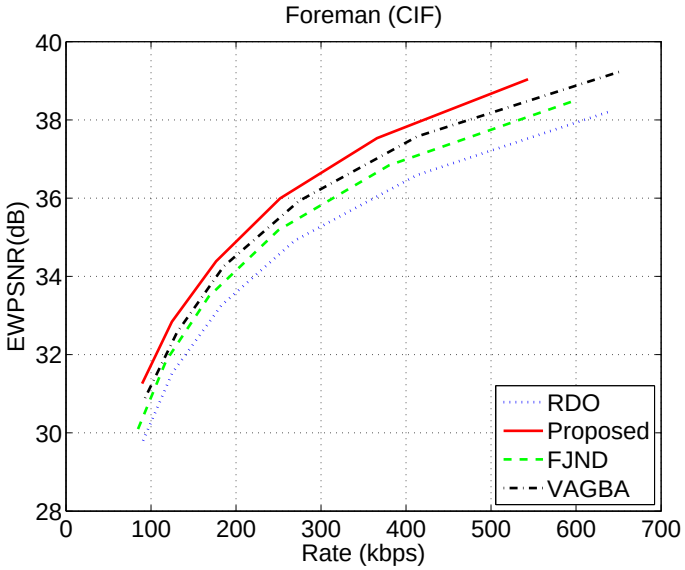

Figure 5.1: A plot of EWPSNR versus rate for *Foreman*.

We first compare the various methods in terms of their bit allocation strategy. To do this, we remove the influence of saliency estimation and its accuracy by using saliency maps produced by eye-tracking heat maps from the database in Chapter 3. This way, FJND, VAGBA, and the proposed method use the same saliency maps, which in turn precisely match the eye-tracking data, leaving bit allocation as the main difference among the methods. Table 5.1 shows BD-EWPSNR and BD-PSNR results with conventional RDO method taken as the baseline. As seen from the results, the proposed method is able to provide an average EWPSNR gain of 2.05 dB with respect to RDO, 1.00 dB (= 2.05 dB −1.05 dB) with respect to VAGBA, and 0.67 dB (= 2.05 dB −1.38 dB) with respect to FJND. In terms of conventional PSNR, the average gain of the proposed method is 0.25 dB (= −0.01 dB +0.26 dB) with respect to FJND, and 0.14 dB (= −0.01 dB +0.15 dB) with respect to VAGBA, while the average loss against RDO is minimal (0.01 dB). These results indicate that the bit allocation strategy of the proposed method is more efficient than that of FJND and VAGBA.

Next, we compare the combination of the proposed methods (that is, the proposed video coding method coupled with the GMC saliency estimation from Section 4.3) against the state of the art. As the state of the art, we take FJND and VAGBA coupled with the IKN-FA saliency model, which was shown as the most accurate in terms of gaze prediction

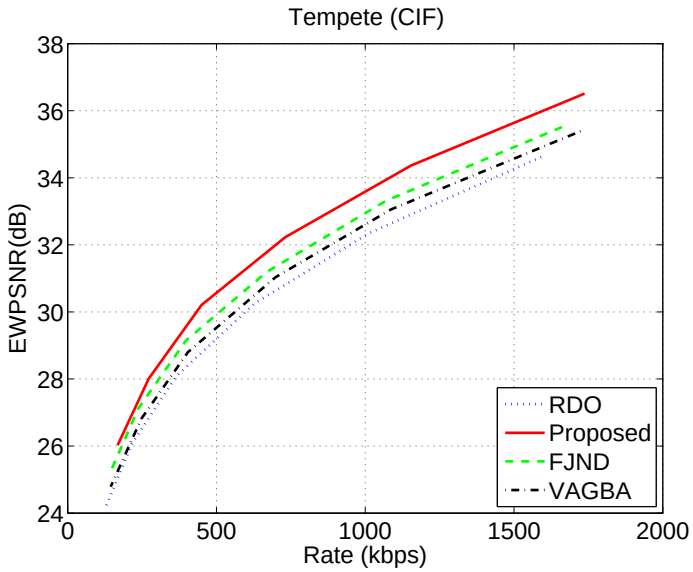

Figure 5.2: A plot of EWPSNR versus rate for *Tempete*.

among the nine tested methods in [92] on the eye-tracking dataset described in Chapter 3. The methods are compared in terms of BD-EWPNSR, BD-PSNR, BD-SSIM [126], and BD-VQM [140],[141] in Table 5.2, with RDO taken as the baseline. Note that the lower the VQM value, the higher the visual quality measured by VQM. As seen from the table, on average, the proposed methods increase the BD-EWPSNR by 1.45 dB with respect to conventional RDO, while achieving zero average loss in PSNR (BD-PSNR = 0.00). Moreover, the proposed methods improve the video quality in terms of all metrics (EWPSNR, PSNR, SSIM, VQM) compared to FJND and VAGBA.

It is interesting to note that RDO performs slightly better, on average, than any of the perceptually-motivated video coding methods in terms of SSIM and VQM. This is likely due to the fact that both SSIM and VQM ignore visual attention (i.e., saliency), while SSIM in addition does not capture temporal aspects of visual quality.

5.3.2 Subjective evaluation

Finally, we performed a subjective evaluation of the perceptual quality of sequences encoded using the proposed saliency-aware compression method versus sequences encoded using FJND [122]. We chose FJND as the competing method here because it performed slightly better than VAGBA in the tests described above. We utilized a Two Alternative

Table 5.1: Comparing the proposed video compression method with the FJND method [122] and the VAGBA method [72] based on the average BD-EWPSNR and BD-PSNR values with respect to the conventional RDO method when the eye-tracking heatmaps are used as the saliency maps.

Video	*FJND* [122]		*VAGBA* [72]		*Proposed*	
	BD-EWPSNR	BD-PSNR	BD-EWPSNR	BD-PSNR	BD-EWPSNR	BD-PSNR
Bus	+1.58	−0.21	+1.16	−0.15	+2.16	+0.08
City	+1.40	−0.27	+1.01	−0.15	+1.98	−0.15
Crew	+1.53	−0.10	+1.02	−0.07	+1.90	+0.20
Foreman	+1.52	−0.31	+0.89	−0.19	+1.98	−0.17
Flower Garden	+1.77	−0.25	+1.26	−0.11	+2.31	+0.02
Hall Monitor	+1.33	−0.54	+0.94	−0.29	+1.79	−0.33
Harbor	+1.02	−0.19	+1.07	−0.14	+1.95	−0.16
Mobile Calendar	+1.00	−0.18	+1.15	−0.13	+2.39	+0.31
Mother & Daughter	+1.28	−0.37	+0.91	−0.18	+2.03	−0.31
Soccer	+1.01	−0.13	+0.93	−0.14	+1.88	−0.05
Stefan	+1.80	−0.39	+1.13	−0.16	+2.04	−0.04
Tempete	+1.67	−0.15	+1.15	−0.09	+2.21	+0.43
Average	+1.38	−0.26	+1.05	−0.15	+2.05	−0.01

Forced Choice (2AFC) method [142] to compare subjective video quality. In 2AFC, the participant is asked to make a choice between two alternatives, in this case, the video encoded using the proposed method vs. video encoded using FJND. This way of comparing quality is less susceptible to measurement noise than quality ratings based on scale, such as Mean Opinion Score (MOS) and Double Stimulus Continuous Quality Scale (DSCQS) [143], because participant's task is much simpler than mapping quality to a number on the scale.

All 12 CIF sequences from the database in Chapter 3 were used in the experiment. All sequences were encoded with a GOP structure of IPPP using the two compression methods. The average PSNR of the encoded videos was around 31 dB, and their bit rates were matched to within 1% difference. In each trial, participants were shown two videos, side by side, at the same vertical position separated by 1 cm horizontally on a mid-gray background. Each video pair was shown for 10 seconds. After this presentation, a mid-gray blank screen was shown for 5 seconds. During this period, participants were asked to indicate on an answer sheet, which of the two videos looks better (Left or Right). They were asked to answer either Left or Right for each video pair, regardless of how certain they were of their response. Participants did not know which video was produced by the proposed method and which one was produced by FJND. Randomly chosen half of the trials had the video

Table 5.2: Comparing various methods with conventional RDO based on the average BD-EWPSNR, average BD-PSNR, average BD-SSIM, and average BD-VQM values.

FJND [122]				
Video	BD-EWPSNR	BD-PSNR	BD-SSIM	BD-VQM
Bus	+0.28	−0.18	−0.007362	+0.011053
City	+0.07	−0.09	−0.003250	+0.004384
Crew	+0.27	−0.08	−0.002006	+0.009742
Foreman	+0.19	−0.16	−0.002003	+0.006101
Flower Garden	+0.60	−0.12	−0.002202	+0.007403
Hall Monitor	+0.67	−0.12	−0.002378	+0.014506
Harbor	+0.13	−0.15	−0.004979	+0.017908
Mobile Calendar	+0.21	−0.12	−0.003537	+0.009658
Mother & Daughter	+0.46	−0.29	−0.004065	+0.016102
Soccer	+0.23	−0.17	+0.024222	−0.008660
Stefan	+0.65	−0.12	−0.000593	+0.000102
Tempete	+0.98	−0.09	−0.003144	+0.009854
Average	+0.40	−0.15	−0.003484	+0.010925
VAGBA [72]				
Video	BD-EWPSNR	BD-PSNR	BD-SSIM	BD-VQM
Bus	+0.37	−0.14	−0.005982	+0.009714
City	+0.06	−0.15	−0.005329	+0.012298
Crew	+0.49	−0.13	−0.003320	+0.017451
Foreman	+0.48	−0.24	−0.003009	+0.011736
Flower Garden	+0.81	−0.13	−0.002743	+0.013063
Hall Monitor	+0.81	−0.13	−0.003006	+0.031234
Harbor	+0.28	−0.16	−0.004281	+0.011610
Mobile Calendar	+0.32	−0.13	−0.003245	+0.004019
Mother & Daughter	+0.32	−0.23	−0.002226	+0.006420
Soccer	+0.54	−0.23	−0.008660	+0.021080
Stefan	+0.67	−0.13	−0.000863	+0.000119
Tempete	+0.71	−0.13	−0.002862	+0.009357
Average	+0.49	−0.17	−0.003794	+0.012347
Proposed				
Video	BD-EWPSNR	BD-PSNR	BD-SSIM	BD-VQM
Bus	+0.93	+0.02	−0.002766	0.001434
City	+1.55	−0.27	−0.014254	+0.028715
Crew	+0.94	+0.11	+0.001360	+0.005731
Foreman	+1.62	−0.11	−0.001289	+0.007552
Flower Garden	+1.73	+0.14	+0.003143	−0.001978
Hall Monitor	+1.65	−0.09	−0.002385	+0.017588
Harbor	+0.98	−0.12	−0.005621	+0.022322
Mobile Calendar	+1.50	+0.38	+0.006875	−0.006075
Mother & Daughter	+1.54	−0.26	−0.004703	+0.017603
Soccer	+1.30	−0.31	−0.014136	+0.036290
Stefan	+1.67	+0.07	+0.001622	−0.000051
Tempete	+1.95	+0.45	+0.007581	−0.011511
Average	+1.45	+0.00	−0.002048	+0.009802

produced by the proposed method on the left side of the screen and the other half on the right side, in order to counteract side bias in the responses. This gave a total of $12 \cdot 2 = 24$ trials.

The experiment was run in a quiet room with 15 participants (14 male, 1 female, aged between 18 and 30). All participants had normal or corrected to normal vision. A 22-inch Dell monitor with brightness 300 cd/m^2 and resolution 1680×1050 pixels was used in our experiments. The brightness and contrast of the monitor were set to 75%. The actual height of the displayed videos on the screen was 185 millimeters. The illumination in the room was in the range 280-300 Lux. The distance between the monitor and the subjects was fixed at 80 cm. Each participant was familiarized with the task before the start of the experiment via a short printed instruction sheet. The total length of the experiment for each participant was approximately 6 minutes.

The results are shown in Table 5.3 in terms of the number of responses that showed preference for the FJND method vs. the proposed method. To test for statistical significance, we used a two-sided χ^2-test [144], with the null hypothesis that there is no preference for either method, i.e., that the votes for each method come from distributions with equal means. Under this hypothesis, the expected number of votes in each trial is 15 for each method, because each video pair was shown twice to each of the 15 participants. The p-value [144] of the test is indicated in the table. As a rule of thumb, the null hypothesis is rejected when $p < 0.05$. When this happens in Table 5.3, it means that the two methods under the comparison cannot be considered to have the same subjective quality, since one of them has obtained a statistically significantly higher number of votes, and therefore seems to have better quality.

In 8 out of the 12 cases in Table 5.3 we have $p < 0.05$, which indicates that subjects showed a statistically significant preference for the proposed method vs. FJND. In only 4 cases (*Bus*, *Flower Garden*, *Harbor*, and *Mobile Calendar*) the p-value is larger than 0.05, which means that neither method achieved a statistically significant advantage. Looking across all trials (i.e., summing up all the votes for the two methods), the results show that participants have preferred the proposed method much more than FJND (268 vs. 92 votes) with overall $p = 0.0001$, which is a very statistically significant result. This confirms that the proposed method is able to provide higher perceptual video quality compared to FJND.

Table 5.3: Subjective comparison of the proposed video compression method against FJND.

Sequence	FJND	Proposed	p-value
Bus	12	18	**0.2733**
City	4	26	0.0001
Crew	7	23	0.0035
Foreman	8	22	0.0106
Flower Garden	10	20	**0.0679**
Hall Monitor	9	21	0.0285
Harbor	11	19	**0.1441**
Mobile Calendar	10	20	**0.0679**
Mother & Daughter	4	26	0.0001
Soccer	5	25	0.0003
Stefan	4	26	0.0001
Tempete	8	22	0.0106
Total	92	268	0.0001

5.4 Conclusions

In this chapter, we presented a saliency-aware video compression method in the context of ROI-based video coding. The proposed method attempts to reduce attention-grabbing coding artifacts, and further allows the saliency of the encoded video to change in a controlled manner – increase in ROI and decrease in non-ROI. This is achieved by adding a saliency distortion term to the distortion metric used in H.264/AVC rate distortion optimization. The GMC saliency estimation method from Section 4.3 was used to estimate saliency distortion. The results indicate that the proposed method is able to improve the visual quality of encoded video compared to conventional RDO video coding, as well as two state-of-the-art perceptually-motivated video coding methods.

Chapter 6

Saliency-Cognizant Video Error Concealment

Despite ongoing efforts to further advance communication technologies, high quality real-time video streaming over best-effort, packet-switched networks remains challenging for a number of reasons. First, consumer demand for interactive streaming video (e.g., conference video such as Skype, Google Talk, etc.) continues to outpace the rate of increase in network bandwidth [145], resulting in congestion and packet queue overflows in packet-switched networks. Second, when packet losses do occur, persistent server-client retransmission is not practical due to playback constraints – a video packet arriving at decoder past its playback deadline is essentially useless. Third, new media types such as ultra-high-resolution video and multiple-view video [146] that promise enhancement of viewing experience are also further straining resource-limited networks due to their large size. Under these practical constraints, it is difficult to guarantee error-free delivery of the entire video from sender to receiver in a timely manner.

Many previous works [147, 148, 149] employed the pro-active methodology of unequal error protection (UEP) of video data, where important packets are protected more heavily, for example, using stronger Forward Error Correction (FEC) codes. Typically, more important packets contain viewer's probable Regions-of-Interest (ROI) [122] in a video frame, or regions with higher visual saliency [2], where viewers most likely will focus their visual attention. In such a scheme, when a packet is lost, the affected region is very likely to be of low visual saliency. While the loss of high-saliency information is still possible, this is a rare

event compared to the loss of low-saliency information, which is less protected. Instead of proactive error protection schemes like UEP, in this chapter, we study the complementary problem of *error concealment*: given the occasional unavoidable packet loss during network transmission, causing the loss of a group of macroblocks (MB) in a video frame, how to best conceal the effect of data loss at the decoder to minimize visual distortion.

Error concealment is typically an under-determined problem: there are insufficient number of well-defined criteria, such as smoothness conditions for boundary pixels adjacent to correctly received neighboring blocks [150], to recover all missing MBs perfectly. This makes choosing the appropriate set of pixels to replace the missing blocks a technically challenging problem. In this chapter, we propose to add a *low-saliency prior* to the error concealment problem as a regularization term. It serves two purposes. First, in ROI-based UEP video streaming, low-saliency prior is likely the correct side information for the lost block and helps the client identify the correct replacement block for concealment. Second, in the event that a perfectly matched block cannot be identified, the low-saliency prior reduces viewer's visual attention on the loss-stricken spatial region, resulting in higher overall subjective quality. At this point, it is appropriate to recall the definition of the word "conceal" from the Oxford English Dictionary [151], which means to keep from sight; hide; keep (something) secret; prevent from being known or noticed. In a way, the low-saliency prior tries to make error concealment live up to its name by attempting to hide damaged blocks from viewers' attention.

We study the effectiveness of a low-saliency prior in the context of a previously proposed RECAP error concealment system [152]. RECAP transmits a low-resolution (LR) version of a video frame alongside the original high-resolution (HR) version, so that if blocks in the HR version are lost, the correctly-received LR version serves as a template for matching of suitable replacement blocks from a previously correctly-decoded HR frame. We add a low-saliency prior to the block identification process, so that only replacement candidate blocks with good match *and* low saliency can be selected. To estimate saliency, we employ our convex approximation to the Itti-Koch-Niebur (IKN) saliency model [2, 67] from Section 4.2. This makes it possible to formulate low-saliency error concealment as a convex optimization problem and solve it efficiently using convex optimization techniques. Indeed, the complexity of the proposed method using the convex saliency approximation can be orders of magnitude lower compared to our previous concealment method in [1], while the resulting video quality

is equal or better. Specifically, experimental results show that: i) PSNR of the error-concealed frames can be increased dramatically – up to 3.6 dB over the original RECAP, and up to 0.7 dB compared to our earlier method in [1], showing the effectiveness of a low-saliency prior in the under-determined error concealment problem; and ii) subjective quality of the repaired video using our proposal, as confirmed by an extensive user study, is better than the original RECAP.

The outline of the chapter is as follows. We discuss related work in Section 6.1, with an overview of the RECAP video transmission system [152] and our earlier error concealment method from [1] in Sections 6.1.1 and 6.1.2, respectively. The new error concealment strategy with low-saliency prior is presented in Section 6.2.1. In Section 6.2.2 we show how the convex approximation to IKN saliency from Section 4.2 can be applied to the missing block and its neighborhood. Finally, experimental results and conclusions are presented in Sections 6.4 and 6.5, respectively.

6.1 Related work

In the last two decades, error resilient video transmission over lossy channels and unreliable networks has been studied extensively [147, 148, 149, 153]. One general approach for recovering lost video data (as well as other kinds of data) is retransmission [153]. Although retransmission is very effective, it increases transmission latency. For example, a round-trip time (RTT) of about 200 ms between California and Singapore [152] makes even a single retransmissions lead to latency that would severely degrade interactivity in applications such as videoconferencing. It should be mentioned that video streaming is generally able to tolerate higher latency than videoconferencing, but even streaming clients have finite playout buffers, which means that the number of possible retransmissions is limited. To avoid retransmission, another general approach is to use Forward Error Correction (FEC). A video-specific variant of FEC is Unequal Error Protection (UEP) [154], which provides stronger protection to more important video data, such as macroblock coding modes and motion vectors. To handle losses in channels with bursty losses, data interleaving techniques are typically necessary in both FEC and UEP. However, data interleaving also increases latency [152].

Another approach to deal with losses in video transmission is decoder-side error concealment. The H.264 video coding standard provides an error resilient feature called Flexible Macroblock Ordering (FMO), which allows macroblocks in slices to be arranged in a checker-board pattern [155], or other, more advanced, 2-D interleaving patterns [156], for more effective error concealment. However, such techniques are not effective when an entire frame is lost. Another technique is Reference Picture Selection (RPS) [153], which can be used to stop error propagation in video transmission with a reaction time of one RTT. In RPS, in order to prevent long-term error propagation, the encoder uses only past reference frames that have been positively acknowledged by the decoder. In [152], a practical solution for low-latency video communications over lossy networks called RECAP (Receiver Error Concealment using Acknowledge Preview) was proposed, which improves upon RPS such that visual quality can be high even when RTT is large. Later in this section, we briefly describe the RECAP framework, upon which we build our error concealment strategy with low-saliency prior at the decoder.

In the face of challenging network conditions during real-time video streaming, UEP strategies protect visually important (salient) regions more heavily. If concealment is done in a *saliency-myopic* way, so that the resulting salient features draw attention to the (likely) imperfectly recovered blocks, it will adversely affect the subjective visual quality. This is one of the main reasons why we apply the low-saliency prior to the error concealment problem, so that concealment can be done in a *saliency-cognizant* manner, resulting in recovered blocks that do not draw unnecessary attention.

Although we apply our low-saliency prior to the RECAP video transmission system [152] for concreteness, we believe that low-saliency prior itself has more general applicability to other ROI-based UEP video streaming systems that may employ other error concealment tools. For example, in [150], where smoothness condition for boundary pixels is used as one condition for recovery, low saliency can be an additional requirement to further facilitate correct block recovery. Note that in our proposed method, we address packet losses in low-saliency spatial regions because that is the *typical* case. Packet loss in more heavily protected highly salient regions, while possible, is a *rare* case, and hence will not affect much the average performance of the system, as long as some default concealment scheme is performed.

Visual saliency—a measure of propensity for drawing visual attention—has been a subject of intense study in the past decade [2, 157, 85]. While earlier works have applied visual

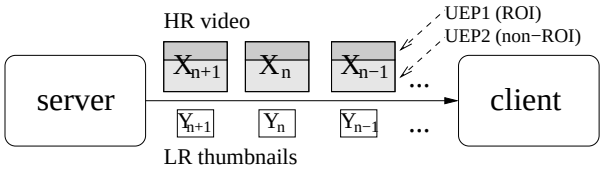

Figure 6.1: Overview of RECAP packet loss recovery system.

saliency principles to video compression [67], to the best of our knowledge, we are the first to apply saliency analysis for error concealment of streaming video. A recent evaluation of saliency models for gaze prediction in video [92] found that the well-known Itti-Koch-Niebur (IKN) saliency model [2], enhanced by the temporal features and 'FancyOne' feature integration [67], was the most accurate among the nine methods tested in that study. In our earlier work on low-saliency error concealment [1], we used the IKN model for saliency calculation. In this chapter, we utilize our convex approximation to the IKN saliency from Section 4.2, which allows us to formulate the error concealment problem with low-saliency prior as a convex optimization problem, leveraging existing polynomial-time convex optimization algorithms for globally optimal solutions. In so doing, as will be shown in Section 6.3 and 6.4, we are able to find far better solutions more computation-efficiently than our previous work in [1].

6.1.1 RECAP video transmission system

Fig. 6.1 shows an overview of the RECAP video transmission system [152]. The server compresses HR video into ROI layer and non-ROI layer. Using UEP, the ROI layer is more heavily protected by stronger FEC than the non-ROI layer. Typically, ROI layer contains more visually salient objects and accounts for 25% or less of the total area of each frame (to be discussed in more detail in Section 6.4). Given the relatively small size of the ROI layer, we will assume it is protected well enough that unrecoverable packet losses, as observed by the client, take place only in the non-ROI layer.

Along with the encoded HR video, the server also low-pass filters and down-samples HR frames into LR thumbnails (preview frames) and transmits them with heavy protection. In practice, the size of a thumbnail is 1/16 (down-sampled by a factor of 4 in both dimensions) of the size of the HR image, and hence it does not incur much redundant transmission overhead. For encoding purposes, when there is no loss, the HR video frames are predicted from any past HR reference frame. However, when a loss is detected, HR video frames are predicted

only from a positively acknowledged reference frames. In contrast, the LR thumbnails are always predicted from positively acknowledged LR frames. The key advantage of such acknowledged thumbnails is that every received thumbnail can be properly decoded.

While data-agnostic FEC suffers from the well-known "cliff" effect, where each block of FEC-protected source data is either recoverable in its entirety or severely damaged and not recoverable at all, the thumbnail-based scheme enables a more graceful recovery, where lost HR video blocks can be partially recovered via block search in previous correctly received HR reference frame, using the corresponding LR thumbnail as a template. Experimental results in [152] showed that by transmitting thumbnails, RECAP outperformed FEC-only schemes. The experimental results in [152] also showed that RECAP outperforms FMO, especially when all slices in a frame are lost. In fact, the effectiveness of RECAP relies on three principles [152]. First, as many lost blocks may exist in previously decoded frames at the decoder, the decoder can exploit the thumbnail frame to search for an appropriate HR block as a replacement for a missing block. Second, in case an appropriate replacement block cannot be identified, the decoder can form a coarse reconstruction from the thumbnail frame. Third, the LR stream does not cost too much overhead as thumbnails are of low resolution. Also, since the thumbnails are predicted only from acknowledged frames, the overall reliability of the system is increased.

In this chapter, we employ RECAP as a platform to demonstrate the performance and effectiveness of our proposed low-saliency prior for video error concealment in loss-corrupted video streaming. As mentioned before, RECAP is employed only for concreteness, to generate a number of good candidates to replace a missing block. Our low-saliency prior can be used in any situation where there is insufficient information to decide among multiple candidate blocks that could potentially replace a missing block.

6.1.2 Overview of the error concealment method from [1]

In [1], we proposed a saliency-cognizant video error concealment method to study the effectiveness of a low-saliency prior in the context of error concealment. In that method, we added a low-saliency prior to the block identification process in RECAP, so that only replacement candidate blocks with good match and low saliency can be selected. In particular, we designed and applied four saliency reduction operators iteratively, in order to reduce the saliency of candidate blocks. These operators were:

1. A notch filter that suppresses the signal in the normalized frequency range $[\pi/256, \pi/16]$;
2. A frequency outlier filter that suppresses large frequency components that are not present in the neighboring blocks;
3. An intensity and color contrast reduction operator that reduces the contrast (and therefore also saliency) in the intensity and color channels of the IKN saliency model;
4. A deblocking filter [158], which was observed to often have the effect of reducing the saliency of the block it is applied to.

These operators were applied on a given RECAP candidate block using the following algorithm:

- **Step 1:** Set $j = 1$, where j refers to the index of one the four saliency reduction operators listed above.
- **Step 2:** Apply the j-th saliency-reduction operator on the current RECAP block.
- **Step 3:** Project the result of Step 2 onto the thumbnail block using a project-to-thumbnail operator to make sure that the low-frequency content of the new candidate is in good match with the thumbnail block.
- **Step 4:** Compute the saliency of the new block obtained after Step 3.
- **Step 5:** Compute a saliency-distortion cost, where the saliency is given by Step 4, and distortion is obtained by the L_2-norm of the difference between the new candidate and the thumbnail block. If the computed cost is lower than the smallest already-known saliency-distortion cost, then go to Step 2. Otherwise go to Step 6.
- **Step 6:** If $j < 4$, then fetch the original RECAP block again, set $j = j + 1$, and go to Step 2. Otherwise end.

The above algorithm was performed on the best K RECAP candidates whose L_2-difference with respect to the thumbnail block was the lowest. In the end, the reconstructed block whose saliency-distortion cost was the lowest was chosen as the final replacement block. To compute the saliency of the new block in Step 4, the IKN saliency model was utilized.

In the present chapter, we extend this earlier work in two ways. First, the objective function in the present work is somewhat improved. In the new objective function, we allow two different weights for the matching to the thumbnail and matching to RECAP candidates. This enables higher emphasis on low-frequency matching to the thumbnail block, which is more reliable than RECAP candidate blocks. And second, instead of the IKN model, we employ our convex approximation to the IKN saliency from Section 4.2, which allows us to make the objective function convex. With the help of this approximation, we are able to solve the error concealment problem at a significantly lower computational cost.

6.2 The proposed error concealment method

In this section, we present our proposed video error concealment method. In the sequel, capital bold letters (e.g., $\mathbf{X}$) denote matrices, lowercase bold letters (e.g., $\mathbf{x}$) denote vectors, and italic letters (e.g., x or X) represent scalars.

6.2.1 Problem formulation

Consider a video frame $\mathbf{F}$ in which some blocks from non-ROI (i.e., low-salient) regions have been lost. Let $\mathbf{X}$ be a lost block of size $N_b \times N_b$, and $\mathcal{N}(\mathbf{X})$ be a $w \times h$ window in $\mathbf{F}$, with $w, h \geq N_b$, such that it covers only the available blocks in $\mathbf{F}$ (i.e., correctly-decoded or already-concealed blocks) in the neighborhood of $\mathbf{X}$, as well as the location of $\mathbf{X}$ itself. Let $\mathcal{S}(\mathcal{N}(\mathbf{X}))$ be a saliency operator that computes the saliency of block $\mathbf{X}$ within $\mathcal{N}(\mathbf{X})$. Also, let $vec(\mathbf{X})$ be the vectorization operator that vectorizes its input matrix $\mathbf{X}$ in a raster scan, $\mathbf{D}$ be a down-sampling matrix [159], $\mathbf{L}$ be a low-pass FIR filter [159], and $\widetilde{\mathbf{L}}$ be the high-pass FIR complement of $\mathbf{L}$, i.e. $\widetilde{\mathbf{L}} = \mathbf{I} - \mathbf{L}$, where $\mathbf{I}$ is the identity matrix.

Our goal is to reconstruct the missing block $\mathbf{X}$ so that the reconstructed block, $\widehat{\mathbf{X}}$, has low saliency after reconstruction. To achieve this goal, we propose the following algorithm, which is applied on every lost block in $\mathbf{F}$ in a raster-scan order:

- **Step 1:** Apply the RECAP algorithm on the missing block $\mathbf{X}$ to obtain the best K RECAP HR candidates $\mathbf{R}_k$, $k = 1, \cdots, K$, whose L_2 difference with respect to the LR thumbnail block $\mathbf{T}$ is the lowest.

- **Step 2:** Compute the 2-D DCT of all available spatial neighbors of $\mathbf{X}$. Let $\mathbf{B}_l$ be a matrix whose entry (i, j) is the DCT coefficient (i, j) with the smallest magnitude

among all available spatial neighboring blocks of $\mathbf{X}$. Similarly, Let $\mathbf{B}_u$ be a matrix whose entry (i, j) is the DCT coefficient (i, j) with the largest magnitude among all available spatial neighboring blocks of $\mathbf{X}$.

- **Step 3:** Given a RECAP candidate block $\mathbf{R}_k$, solve the following minimization problem to obtain the reconstructed block $\widehat{\mathbf{X}}_k$

$$\widehat{\mathbf{X}}_k = \underset{\mathbf{X}}{\operatorname{argmin}} \left[\mathcal{S}\left(\mathcal{N}(\mathbf{X})\right) + \lambda_1 \left\| \mathbf{D}\mathbf{L}vec(\mathbf{X}) - vec(\mathbf{T}) \right\|_2^2 + \lambda_2 \left\| \widetilde{\mathbf{L}}vec(\mathbf{X}) - \widetilde{\mathbf{L}}vec(\mathbf{R}_k) \right\|_2^2 \right], \quad \text{subject to} \quad \mathbf{B}_l \leq \mathbf{\Phi}\mathbf{X}\mathbf{\Phi}^t \leq \mathbf{B}_u, \tag{6.1}$$

  where λ_1 and λ_2 are two positive real scalars, $\|.\|_2$ denotes the L_2-norm, and $\mathbf{\Phi}$ is the 2-D DCT matrix, which is of the same size as $\mathbf{X}$. The down-sampling factor of $\mathbf{D}$ is set to the same down-sampling factor that is used to generate $\mathbf{T}$, and $\mathbf{L}$ is used to avoid aliasing due to down-sampling.

- **Step 4:** Repeat Step 3 for all the K RECAP candidates. Select the candidate with the smallest objective function value (6.1) as the final reconstructed block $\widehat{\mathbf{X}}$.

The first term in the objective function in (6.1) measures the saliency of the reconstructed block within $\mathcal{N}(\mathbf{X})$. The minimization of this term ensures that the reconstructed block has low saliency after reconstruction. At the same time, the constraint defined in (6.1) tries to eliminate any potential frequency outliers in the reconstructed block by restricting the frequency content of the reconstructed block to be within the extremes of the frequency content of its available neighboring blocks. This constraint plays the role of the frequency outlier filter from our previous approach [1].

The second term of the objective function in (6.1) ensures that the reconstructed block remains in good match with the thumbnail block, while the third term in (6.1) tries to match the high-frequency content in the candidate block to that of the RECAP candidate block. In practice, λ_1 should be set to a larger value than λ_2. The reason is that the thumbnail block can be considered as a very reliable side information for the low frequency content of the missing block, so it makes sense to enforce a very good match to the thumbnail block, i.e., large λ_1. However, the match does not have to be exact, because the thumbnail block has been quantized and compressed as well, and we do not want to over-fit the low frequency content of the reconstructed block to the quantized thumbnail.

Unlike the low-frequency content in the second term in (6.1), we do not have a very reliable side information for the high-frequency content of the missing block in the third term in (6.1). All we know comes from the high frequency information of the RECAP candidate block, which might not be the same as the original high frequency content of the missing block. Hence, λ_2 should be set to a smaller value than λ_1. In our experiments, we used $\lambda_1 = 1.5$ and $\lambda_2 = 0.5$. The hope is that saliency consideration will provide sufficient additional information to reconstruct the high-frequency content of the missing block reasonably well.

6.2.2 The saliency operator $\mathcal{S}(\mathcal{N}(\mathbf{X}))$

The error concealment problem formulation in (6.1) involves the saliency operator $\mathcal{S}(\mathcal{N}(\mathbf{X}))$ that computes the saliency of $\mathbf{X}$ within $\mathcal{N}(\mathbf{X})$. In our previous work [1], we used the IKN saliency model as an implementation of $\mathcal{S}(\mathcal{N}(\mathbf{X}))$. However, this approach has two disadvantages: (i) it is computationally expensive, as discussed in [103], and (ii) it is non-convex in $\mathbf{X}$, making it difficult to find the globally optimal solution to (6.1). To solve these problems, we use our convex approximation to the IKN saliency from Section 4.2. With a saliency operator $\mathcal{S}(\mathcal{N}(\mathbf{X}))$ that is convex in $\mathbf{X}$, the optimization problem in (6.1) becomes convex (the last two terms in the objective function are already convex, as is the constraint), making it possible to solve (6.1) using a variety methods for convex optimization [160, 161]. As was demonstrated in Section 4.4.1, our convex saliency operator approximates the IKN saliency very well, yet has an advantage of being simpler to compute and easier to integrate into various optimization problems.

Equation (4.9) is a convex approximation to the IKN saliency of block $\mathbf{X}$ by itself, regardless of its neighborhood. We now define the operator $\mathcal{S}(\mathcal{N}(\mathbf{X}))$ that computes the saliency of $\mathbf{X}$ within a neighborhood $\mathcal{N}(\mathbf{X})$. Let $\mathcal{N}(\mathbf{X})$ be a $p \times p$ matrix of pixels in $\mathbf{F}$ (with $p > N_b$) such that it covers both the $N_b \times N_b$ missing block $\mathbf{X}$ and parts of the available 8-connected spatial neighbors of $\mathbf{X}$. Hence, the position of $\mathcal{N}(\mathbf{X})$ relative to $\mathbf{X}$ depends on the available neighbors of $\mathbf{X}$. In Appendix A, we describe various possible cases for defining $\mathcal{N}(\mathbf{X})$ relative to $\mathbf{X}$. The saliency $\mathcal{S}(\mathcal{N}(\mathbf{X}))$ is computed as in (4.9), with $\mathbf{X}$ replaced by $\mathcal{N}(\mathbf{X})$. Below we show that both the spatial and temporal saliency terms of (4.9) are still convex in $\mathbf{X}$ when $\mathbf{X}$ is replaced by $\mathcal{N}(\mathbf{X})$.

Let $\mathbf{B}$ be a $p \times p$ matrix whose elements are all equal to the elements of $\mathcal{N}(\mathbf{X})$ except for the elements whose coordinates coincide with $\mathbf{X}$, which are set to zero. In other words, $\mathbf{B}$ is

a matrix that contains the boundary pixels of $\mathcal{N}(\mathbf{X})$ around the missing block $\mathbf{X}$. Fig. 6.2 illustrates $\mathbf{X}$, $\mathcal{N}(\mathbf{X})$, and $\mathbf{B}$.

$\mathcal{N}(\mathbf{X})$ can be obtained by zero-padding (expanding) $\mathbf{X}$ via a matrix expansion operator, $\mathcal{Z}(\mathbf{X},\mathcal{N}(\mathbf{X}))$, and adding the resulting matrix to $\mathbf{B}$. The matrix expansion operator, $\mathcal{Z}(\mathbf{X},\mathcal{N}(\mathbf{X}))$, zero-pads the $N_b \times N_b$ matrix $\mathbf{X}$ up to a $p \times p$ matrix, $\mathbf{X}_e$, and can be realized as a linear operation

$$\mathbf{X}_e = \mathcal{Z}(\mathbf{X},\mathcal{N}(\mathbf{X})) = \mathbf{MXN}, \tag{6.2}$$

where $\mathbf{M}$ is a binary matrix of size $p \times N_b$, and $\mathbf{N}$ is a binary matrix of size $N_b \times p$, both of which depend on $\mathcal{N}(\mathbf{X})$. The method to derive $\mathbf{M}$ and $\mathbf{N}$ based on $\mathcal{N}(\mathbf{X})$ is given in Appendix A. Finally, since

$$\mathcal{N}(\mathbf{X}) = \mathbf{X}_e + \mathbf{B} = \mathbf{MXN} + \mathbf{B} \tag{6.3}$$

is an affine function of $\mathbf{X}$, it is also convex in $\mathbf{X}$. Due to this, we have that

$$\mathcal{S}_{spatial}(\mathcal{N}(\mathbf{X})) = \mathcal{S}_{spatial}(\mathbf{MXN} + \mathbf{B}), \tag{6.4}$$

where $\mathcal{S}_{spatial}(\cdot)$ is computed as in (4.7),

$$\mathcal{S}_{temporal}(\mathcal{N}(\mathbf{X})) = \mathcal{S}_{temporal}(\mathbf{MXN} + \mathbf{B}), \tag{6.5}$$

where $\mathcal{S}_{temporal}(\cdot)$ is computed as in (4.8), and

$$\mathcal{S}(\mathcal{N}(\mathbf{X})) = \mathcal{S}_{spatial}(\mathcal{N}(\mathbf{X})) + \alpha\mathcal{S}_{temporal}(\mathcal{N}(\mathbf{X})), \tag{6.6}$$

where α is positive as in (4.9), are all convex in $\mathbf{X}$.

6.2.3 Solving the error concealment problem

By using a saliency operator $\mathcal{S}(\mathcal{N}(\mathbf{X}))$ that is convex in $\mathbf{X}$, the optimization problem in equation (6.1) becomes convex. The objective function is the sum of three terms. The first term is convex in $\mathbf{X}$ if the convex saliency operator discussed above is used. The second and third terms are compositions of vectorization (which is convex [162]), linear filtering, and the squared L_2-norm (which is also convex [161]), making them both convex in $\mathbf{X}$. Finally, the constraint is a combination of affine functions in $\mathbf{X}$, making it convex in $\mathbf{X}$. Hence, in this case, a variety of methods for convex optimization [161], such as interior-point, ellipsoid, subgradient, etc., can be used to solve (6.1). In our expeirments, we used the SeDumi algorithm available in the cvx Matlab package [163].

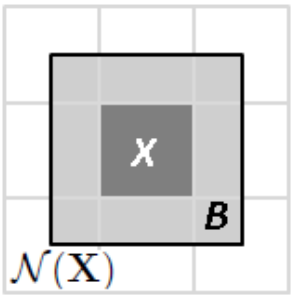

Figure 6.2: An illustration of the missing block $\mathbf{X}$, and matrices $\mathcal{N}(\mathbf{X})$ and $\mathbf{B}$. Note that $\mathcal{N}(\mathbf{X})$ covers the missing block $\mathbf{X}$ and parts of the available spatial neighbors of $\mathbf{X}$. $\mathbf{B}$ is a matrix that contains the boundary pixels of $\mathcal{N}(\mathbf{X})$ around the missing block $\mathbf{X}$ (light-shaded area around $\mathbf{X}$ in this figure). Those elements of $\mathbf{B}$ whose coordinates coincide with $\mathbf{X}$ are set to zero. The saliency of $\mathbf{X}$ is computed within the area covered by $\mathcal{N}(\mathbf{X})$. In this example, it is assumed that all the 8-connected spatial neighbors of $\mathbf{X}$ are available. Depending on the availability of the spatial neighbors of $\mathbf{X}$, the area covered by $\mathcal{N}(\mathbf{X})$ changes, as discussed in Appendix A.

6.3 Computational complexity

In Section 6.3.1, we analyze the computational complexity of solving (6.1) when the convex saliency operator discussed above is used. Following that, in Section 6.3.2 we compare this complexity against the complexity of our previous method from [1].

6.3.1 Computational complexity of the proposed method

In this section, we estimate the computational cost of the error concealment method presented in Section 6.2.1. In the proposed method, the minimization problem defined in (6.1) is solved for the best K RECAP candidates whose L_2 difference with respect to the thumbnail block is the lowest. In the end, the best block whose saliency-distortion cost in (6.1) is the lowest, is taken as the concealed block.

To estimate the computational cost, we need to answer two questions: 1) how many evaluations of the objective function in (6.1) are needed? and 2) how many operations are required in each evaluation of the objective function in (6.1)? The first question is difficult to answer in general. As mentioned in Section 6.2.3, a convex optimization problem can be solved relatively easily (in polynomial time) by various convex optimization methods such as interior-point and ellipsoid methods [160, 161]. However, the exact number of objective

function evaluations is not easily determined. In our experiments we found that usually about 8 objective function evaluations are needed to achieve an acceptable tolerance level of $\epsilon = 10^{-6}$ when solving (6.1) for 16×16 blocks. Hence, for the purpose of estimating complexity, we assume that the average number of objective function evaluations in (6.1) is $N_e = 8$.

We now compute the number of operations that are performed in one evaluation of the objective function in (6.1). To find the cost for the first term in (6.1), we need to find the cost of the saliency operator $\mathcal{S}(\mathcal{N}(\mathbf{X}))$ defined in (6.6), which involves in computing $\mathcal{S}_{spatial}(\mathcal{N}(\mathbf{X}))$ and $\mathcal{S}_{temporal}(\mathcal{N}(\mathbf{X}))$. The first step in computing $\mathcal{S}_{spatial}(\mathcal{N}(\mathbf{X}))$ is to construct $\mathcal{N}(\mathbf{X})$. In practice, $\mathcal{N}(\mathbf{X})$ can be constructed by copying the $N_b \times N_b$ block $\mathbf{X}$ to the zero locations of the $p \times p$ matrix $\mathbf{B}$ (i.e., locations in which the elements of $\mathbf{B}$ are zero). To copy a $N_b \times N_b$ matrix to another place in memory, we need to update the pointer address of both the source and destination locations after reading/copying each row of the matrix. To obtain the pointer address of the next row of the matrix, we first need to increase the current row number by one, and then the convert the 2-D address of the first element of next row into a linear 1-D address. This needs 3 operations (two additions and one multiplication) [164]. Hence, we consider approximately $2 \cdot 3N_b = 6N_b$ operations for copying a $N_b \times N_b$ matrix to another place in memory. Assuming that $\mathbf{B}$ is available before solving (6.1), copying the $\mathbf{X}$ to the zero locations of $\mathbf{B}$ needs approximately $6N_b$ operations.

The next step is to compute the 2-D DCT of $\mathcal{N}(\mathbf{X})$. Note that the multiplication of a $A \times B$ matrix by a $B \times C$ matrix requires $A \cdot C \cdot (2B - 1)$ operations. Also, computing the 2-D DCT of a $p \times p$ block requires two $p \times p$ matrix multiplications. Hence, computing the 2-D DCT of $\mathcal{N}(\mathbf{X})$ requires $2p^2(2p - 1)$ operations. We then need to compute the square of the Wiener-filtered coefficients. This step needs $2p^2$ operations. Finally, all the squared Wiener-filtered coefficients should be summed up together. This step needs approximately p^2 operations. Hence, computing $\mathcal{S}_{spatial}(\mathcal{N}(\mathbf{X}))$ in the luma (Y) channel of $\mathbf{X}$ requires approximately $6N_b + p^2(4p + 1)$ operations. Assuming that $\mathbf{X}$ is in YUV 4:2:0 format, the total computational cost for computing $\mathcal{S}_{spatial}(\mathcal{N}(\mathbf{X}))$ will be $1.5(6N_b + p^2(4p + 1))$.

To compute $\mathcal{S}_{temporal}(\mathcal{N}(\mathbf{X}))$, we first need to compute the absolute difference between $\mathcal{N}(\mathbf{X})$ and the co-located $p \times p$ block in the previous frame in the luma (Y) channel. For this purpose, we need to construct the neighborhood in the previous frame similar to $\mathcal{N}(\mathbf{X})$. This approximately needs $6N_b$ operations. Note that $\mathcal{N}(\mathbf{X})$ is already constructed when computing $\mathcal{S}_{spatial}(\mathcal{N}(\mathbf{X}))$. Thus, this step requires about $6N_b + 2p^2$ operations, where we

considered two operations for computing the absolute difference between two elements of memory. We then need to compute the 2-D DCT of the obtained residual block, which requires $2p^2(2p-1)$ operations. After that we need to compute the sum of the squared Wiener-filtered coefficients of the residual block, which requires approximately $2p^2 + p^2$ operations. Hence, computing $\mathcal{S}_{temporal}(\mathcal{N}(\mathbf{X}))$ requires approximately $2p^2(2p+3)$ operations. Based on the above analysis, computing $\mathcal{S}(\mathcal{N}(\mathbf{X}))$ requires approximately $9N_b + p^2(10p+7.5) + 2$ operations.

To find the computational cost of the second and third terms in (6.1), we first note that if the size of $\mathbf{X}$ in (6.1) is $N_b \times N_b$, then $\mathbf{L}$ and $\widetilde{\mathbf{L}}$ are both of size $N_b^2 \times N_b^2$, while $\mathbf{D}$ (the down-sampling matrix) is a $(N_b^2/d_s^2) \times N_b^2$ matrix, where d_s is the down-sampling factor that is used to generate the thumbnail block $\mathbf{T}$. To vectorize a $N_b \times N_b$ matrix, similar to the case discussed above for copying a $N_b \times N_b$ block to another location in the memory, we consider about $6N_b$ operations. Hence, to obtain $vec(\mathbf{R}_k)$ or $vec(\mathbf{X})$, we consider approximately $6N_b$ operations. Similarly, we approximate the cost for obtaining $vec(\mathbf{T})$ by $6N_b/d_s$ operations.

To compute $\mathbf{DL}vec(\mathbf{X})$ for evaluating the second term in (6.1), we can first compute $\mathbf{L}vec(\mathbf{X})$, which requires $N_b^2(2N_b^2 - 1)$ operations. We can then multiply $\mathbf{D}$ by the resultant $N_b^2 \times 1$ vector. This requires additional $N_b^2(2N_b^2 - 1)/d_s^2$ operations. Hence, in total, computing $\mathbf{DL}vec(\mathbf{X})$ costs $N_b^2(2N_b^2 - 1) + N_b^2(2N_b^2 - 1)/d_s^2 + 6N_b$ operations.

As a simpler alternative, however, the low-pass filtering can be performed in the DCT domain. For this purpose, we first compute the 2-D DCT of $\mathbf{X}$, which needs $2N_b^2(2N_b - 1)$ operations. We then zero out the desired high frequency coefficients. This process needs approximately N_b^2 operations. We then take the inverse 2-D DCT of the obtained result to get the filtered block in the pixel domain. This step needs $2N_b^2(2N_b - 1)$ additional operations. Finally, we down-sample the obtained block by a down-sampling factor d_s to get a down-sampled block of the same size as $\mathbf{T}$. We consider N_b^2/d_s^2 operations for this step. Finally, the L_2-norm of the difference between the obtained low-resolution block and $\mathbf{T}$ must be calculated. This step requires approximately $3N_b^2/d_s^2$ operations. Therefore, in total, computing the second term of (6.1) in the luma (Y) channel requires approximately $N_b^2(8N_b - 3 + 4/d_s^2)$ operations.

For computing the third term in (6.1), a similar approach can be utilized. Specifically, we take the 2-D DCT of both $\mathbf{X}$ and $\mathbf{R}_k$, and compute the L_2-norm of the difference between the high frequency coefficients of $\mathbf{X}$ and $\mathbf{R}_k$. To compute the L_2-norm, only those high frequency DCT coefficients that are zeroed out when computing the second term of (6.1)

are utilized. Note that since DCT is a unitary transform, we do not need to take the inverse 2-D DCT to compute the L_2-norm difference in the pixel domain. The 2-D DCT of $\mathbf{X}$ is available after computing the second term in (6.1). Thus, we only need to compute the 2-D DCT of $\mathbf{R}_k$, which can be pre-computed before evaluating (6.1). Considering $3N_b^2$ operations for computing the L_2-norm, computing the third term in (6.1) in the luma (Y) channel requires approximately $3N_b^2$ operations.

In summary, we conclude that computing the second term in (6.1) for all three YUV 4:2:0 channels of $\mathbf{X}$ in each evaluation of the objective function requires approximately $1.5 \cdot (N_b^2(8N_b - 3 + 4/d_s^2)$ operations. For the third term, the cost is approximately $1.5 \cdot (3N_b^2)$ operations.

To evaluate the constraint in (6.1), we need to compare the 2-D DCT of $\mathbf{X}$ with both $\mathbf{B}_l$ and $\mathbf{B}_u$. For these two comparisons, we consider $2N_b^2$ operations. The 2-D DCT of $\mathbf{X}$ is computed during the evaluation of the second term in (6.1) as described above. Hence, assuming that $\mathbf{B}_l$ and $\mathbf{B}_u$ are pre-computed before solving (6.1), evaluating the constraint for all three YUV 4:2:0 channels of $\mathbf{X}$ requires $1.5 \cdot (2N_b^2) = 3N_b^2$ operations.

Before evaluating (6.1), we need to compute the 2-D DCT of $\mathbf{R}_k$, which requires $1.5 \cdot 2N_b^2 \cdot (2N_b - 1)$ operations. We also need to compute $\mathbf{B}_l$ and $\mathbf{B}_u$. Assuming the worst case (from the point of view of complexity) that all the four spatial neighbors of $\mathbf{X}$ are available, and that none of them are neighbors of any previously concealed blocks (in which case their 2-D DCT would already be available), we need to compute the 2-D DCT of all four neighbors. This requires $1.5 \cdot 4 \cdot 2N_b^2(2N_b - 1)$ operations. Assuming that finding the minimum or maximum of 4 DCT coefficients needs 3 operations, we can estimate the cost for computing $\mathbf{B}_l$ or $\mathbf{B}_u$ as $1.5 \cdot 3N_b^2 = 4.5N_b^2$ operations. Hence, the total cost for computing $\mathbf{R}_k$, $\mathbf{B}_l$, and $\mathbf{B}_u$ is approximately $N_b^2(30N_b - 11)$ operations.

Overall, for the YUV 4:2:0 video format, the total computational cost of the proposed error concealment method for reconstructing a $N_b \times N_b$ block $\mathbf{X}$ within a $p \times p$ neighborhood $\mathcal{N}(\mathbf{X})$ is approximately

$$\begin{aligned}\zeta(PM) &\approx N_b^2(30N_b - 11) + N_e\Big((9N_b + p^2(10p + 7.5) + 2) + \\ &\qquad 1.5(N_b^2(8N_b - 3 + \frac{4}{d_s^2})) + 3N_b^2\Big) \\ &= N_b^2(30N_b - 11) + N_e\Big(12N_b^3 - 1.5N_b^2 + 9N_b + \frac{6}{d_s^2} + 10p^3 + 7.5p^2 + 2\Big).\end{aligned} \tag{6.7}$$

6.3.2 Comparison with the method from [1]

In our experiments, the size of each missing block $\mathbf{X}$ is 16×16. Therefore, $N_b = 16$. We also set $d_s = 4$ and $p = 20$ so that the window $\mathcal{N}(\mathbf{X})$ covers a 20×20 region. With these parameters in (6.7), we get

$$\zeta(PM) \approx 1175379. \tag{6.8}$$

Meanwhile, our previous error concealment method from [1] requires the computation of IKN saliency [67] within an adaptive window of size $W_0 \times H_0$ that includes the missing block and its causal spatial neighborhood. As discussed in [103], the number of operations required to reconstruct a missing block of size $N_b \times N_b$ pixels by our previous method in [1] is

$$\zeta(OM) \approx 36.56N_b^3 + \left(\log_2 \tfrac{N_b^6}{4} + 1104.5\right) N_b^2 + 5882 \cdot W_0 \cdot H_0. \tag{6.9}$$

Substituting $N_b = 16$ we obtain

$$\zeta(OM) \approx 438133 + 5882 \cdot W_0 \cdot H_0. \tag{6.10}$$

Note that W_0 and H_0 can be as small as N_b, the size of the block, or as large as W and H, the width and height of the frame. The number of operations involved in reconstructing a block varies depending on the position of that block, which determines W_0 and H_0 [1]. At the low end, when $W_0 = H_0 = N_b = 16$, $\zeta(PM) \approx 0.60 \cdot \zeta(OM)$, making the proposed method roughly 40% less costly than the method from [1]. At the high end, when W_0 and H_0 are equal to the dimensions of the frame, then even for a CIF resolution of 352×288 (which may be considered small by today's standards), we obtain $\zeta(PM) \approx 0.002 \cdot \zeta(OM)$. Hence, in this case, the proposed method has only 1/500-th of cost of the method from [1]. In practice, the computational savings will be somewhere between these two extreme values. To get a feeling for the average case, consider CIF resolution video (352×288). Assuming that each block is equally likely to be damaged, the expected (average) position of the damaged block is at the center of the frame, and the expected values of W_0 and H_0 are $352/2 = 176$ and $288/2 = 144$, respectively. Using these values in (6.10) and comparing the result with $\zeta(PM)$, we find $\zeta(PM) \approx 0.008 \cdot \zeta(OM)$. That is, the expected cost of the proposed method in the case of CIF resolution video is about 1/120-th of that in [1].

6.4 Experimental results

In this section, we evaluate the performance of the saliency-cognizant error concealment method from Section 6.2.1 by comparing it with the original RECAP algorithm, as well as our previous error concealment method from [1].

In order to evaluate the performance of the proposed error concealment method, we used four standard 30 fps sequences: *Soccer* (704×576), *RaceHorses* (416×240), *Tractor* (768×432), and *Crew* (704×576). All sequences were 250 frames long. *RaceHorses* was encoded at 700 kbps, while the other three higher-resolution sequences were encoded at 1400 kbps using the H.264/AVC JM 18.0 reference software [114], with the GOP structure IPPP. The thumbnail videos were created by down-sampling their corresponding high resolution (HR) videos by a factor of 4 in each dimension, and were encoded at 10% of the bitrate of their HR version, using the same encoder structure as their HR version. We set $N_b = 16$, $p = 20$, $\alpha = 1$, $\lambda_1 = 1.5$ and $\lambda_2 = 0.5$.

In order to find the most salient regions (ROIs), we first computed the full IKN saliency map of each video frame of each sequence. The saliency map of each frame was then binarized based on the 75-th percentile of the saliency map of that frame. Macroblocks with saliency above the 75-th percentile threshold were considered as ROIs.

To simulate a video streaming scenario with RECAP as its error control mechanism, a video frame was selected randomly, and its macroblocks in non-ROI parts were dropped randomly based on a two-state Gilbert model [165] at two different average loss rates (3% and 10%) with an average burst loss length of 8. The corrupted frame was then concealed using the original RECAP algorithm, our previous error concealment method from [1], as well as our proposed error concealment method from Section 6.2.1. The RECAP method, as well as the two other error concealment methods, require a correctly-received reference frame to generate RECAP candidates. This was assumed to be either 5 or 10 frames away. In practice, the distance between the concealed and reference frame is random. We used 5 and 10 simply as representative test values. This procedure was repeated on about 30% of the randomly chosen frames from each sequence.

6.4.1 Objective quality assessment

In Table 6.1, we compared the performance of the proposed error concealment method with the RECAP method and our earlier error concealment method from [1] at 3% loss

Table 6.1: Comparing the proposed error concealment method with RECAP and [1], using various image/video quality assessment methods, at 3% loss rate, and at two reference frame distances: $d = 10$ and $d = 5$.

		Soccer			*RaceHorses*		
d	Metric	RECAP	[1]	Proposed	RECAP	[1]	Proposed
10	PSNR	34.6	35.3	35.5	37.6	38.0	38.2
	SSIM	0.943254	0.944754	0.946126	0.978554	0.979591	0.980300
	VQM	0.204069	0.161319	0.157103	0.088587	0.081535	0.080902
5	PSNR	35.7	36.1	36.2	38.3	38.5	38.9
	SSIM	0.955522	0.956073	0.956709	0.990184	0.992794	0.993050
	VQM	0.168544	0.153910	0.139484	0.077677	0.077879	0.077382

		Tractor			*Crew*		
d	Metric	RECAP	[1]	Proposed	RECAP	[1]	Proposed
10	PSNR	32.4	33.8	34.2	35.1	38.2	38.4
	SSIM	0.930999	0.940424	0.943242	0.956591	0.969242	0.970139
	VQM	0.170746	0.139316	0.138356	0.217980	0.148807	0.148376
5	PSNR	34.2	34.3	35.0	36.5	38.6	38.9
	SSIM	0.973539	0.981457	0.982164	0.965405	0.972251	0.973920
	VQM	0.125716	0.126531	0.125092	0.185925	0.137344	0.136188

Table 6.2: Comparing the proposed error concealment method with RECAP and [1] based on various image/video quality assessment methods, at 10% loss rate, and at two different reference frame distances: $d = 10$ and $d = 5$.

		Soccer			*RaceHorses*		
d	Metric	RECAP	[1]	Proposed	RECAP	[1]	Proposed
10	PSNR	30.1	31.0	31.2	28.5	28.9	29.1
	SSIM	0.847758	0.854268	0.855404	0.857703	0.863775	0.866455
	VQM	0.413155	0.339648	0.313936	0.326603	0.264199	0.240614
5	PSNR	31.1	31.5	31.6	29.1	29.5	29.7
	SSIM	0.874573	0.875573	0.876853	0.878562	0.883668	0.885283
	VQM	0.366916	0.315949	0.305230	0.276700	0.238212	0.235563

		Tractor			*Crew*		
d	Metric	RECAP	[1]	Proposed	RECAP	[1]	Proposed
10	PSNR	27.2	28.9	29.0	29.8	33.2	33.4
	SSIM	0.790720	0.822753	0.822901	0.867791	0.904089	0.904329
	VQM	0.271512	0.225952	0.223710	0.363882	0.292193	0.253789
5	PSNR	30.0	30.4	30.5	31.1	33.3	33.6
	SSIM	0.905805	0.906624	0.910247	0.890988	0.908552	0.910276
	VQM	0.248732	0.220100	0.203267	0.320792	0.261871	0.241848

rate, and at two reference frame distances, $d = 5$ and $d = 10$, based on three metrics: PSNR, SSIM [126], and VQM [140, 141]. These frame-level metrics were computed at the aforementioned average loss rates on the concealed frames. The general VQM model [140] was utilized for computing the VQM values. Only the luma (Y) channel was considered for computing the PSNR and SSIM values. Table 6.2 shows the results for the same comparison as in Table 6.1 but at an average loss rate of 10%.

As seen from Table 6.1 and Table 6.2, the proposed method is able to improve the PSNR of the concealed frames by up to 3.6 dB compared to RECAP (*Crew* with $d = 10$ at 10% loss rate), and by up to 0.7 dB compared to our earlier method from [1] (*Tractor* with $d = 5$ at 3% loss rate). This shows that the proposed error concealment method is able to provide correct side information for resolving the ambiguity in reconstructing the missing blocks in the under-determined problem of error concealment. As seen from the SSIM and VQM results, the proposed error concealment method provides better quality than the RECAP method. Note that the smaller the VQM value, the better the quality. We also note that the objective quality of the proposed error concealment method as measured by the SSIM and VQM metrics is close to or better than our earlier method from [1].

The results demonstrate that even though our earlier method in [1] used the actual IKN saliency while the method proposed here uses only an approximation, we are able to improve upon the results from [1]. This is because the present error concealment formulation in (6.1) allows for direct search for the missing block $\mathbf{X}$, whereas in [1], the concealment proceeded indirectly by applying saliency reduction operators, in an iterative fashion, upon RECAP candidate blocks. This, combined with the non-convexity of the objective function from [1], made the algorithm in [1] susceptible to getting stuck in a local optimum. The present algorithm does not have that problem, and it is computationally more efficient.

6.4.2 Subjective evaluation

Since the proposed error concealment method aims at reducing the saliency of concealed blocks, we performed a subjective test to verify the improvement in subjective quality. For this purpose, we compared the subjective quality of the proposed error concealment method with RECAP, as well as our earlier method from [1].

In our experiment, a Two Alternative Forced Choice (2AFC) method [142] was used to compare subjective video quality. In 2AFC, the participant is asked to make a choice between two alternatives, in this case, the proposed method vs. either the original RECAP

method or our earlier method [1]. This way of comparing quality is less susceptible to measurement noise than quality ratings based on scale, such as Mean Opinion Score (MOS) and Double Stimulus Continuous Quality Scale (DSCQS) [143], because participant's task is much simpler than mapping quality to a number on the scale.

Four test sequences mentioned above, at two loss rates (3% and 10%) were used in the experiment. In each trial, participants were looking at two side-by-side videos (in the same vertical position, separated by 1 cm horizontally) on a mid-gray background. Each video pair was shown for 9 seconds. After this presentation, a mid-gray blank screen was shown for 5 seconds. During this period, participants were asked to indicate on an answer sheet, which of the two videos looks better (Left or Right). They were asked to answer either Left or Right for each video pair, regardless of how certain they were of their response. Participants did not know which video was obtained by the proposed method and which one was obtained by the alternative method (RECAP or [1]). Randomly chosen half of the trials had the video produced by the proposed method on the left side of the screen and the other half on the right side, in order to counteract side bias in the responses. This gave a total of $4 \cdot 2 \cdot 2 = 16$ trials for comparing the proposed error concealment method with each of the alternative methods.

The experiment was run in a quiet room with 15 participants (11 male, 4 female, aged between 18 and 30). All participants had normal or corrected to normal vision. A 22-inch Dell monitor with brightness 300 cd/m^2 and resolution 1680×1050 pixels was used in our experiments. The brightness and contrast of the monitor were set to 75%. The actual height of the displayed videos on the screen was 185 millimeters. The illumination in the room was in the range 280-300 Lux. The distance between the monitor and the subjects was fixed at 80 cm. Each participant was familiarized with the task before the start of the experiment via a short printed instruction sheet. The total length of the experiment for each participant was approximately 8 minutes.

The results for the comparison between the RECAP method and our proposed error concealment method are shown in Tables 6.3 and 6.4. In Table 6.3 we show the number of responses that showed preference for the original RECAP method vs. the proposed method, and in Table 6.4 we show the votes for the method from [1] vs. the proposed one.

To test for statistical significance, we used a two-sided χ^2-test [144], with the null hypothesis that there is no preference for either method, i.e., that the votes for each method come from distributions with equal means. Under this hypothesis, the expected number of

Table 6.3: Subjective comparison of the proposed method against RECAP.

Loss Rate	Method	*Crew*	*Soccer*	*Tractor*	*RaceHorses*
3%	RECAP	2	6	6	3
	Proposed	28	24	24	27
	p-value	0.0001	0.0010	0.0010	0.0001
10%	RECAP	1	5	8	4
	Proposed	29	25	22	26
	p-value	0.0001	0.0003	0.0106	0.0001

Table 6.4: Subjective comparison of the proposed method against the method from [1].

Loss Rate	Method	*Crew*	*Soccer*	*Tractor*	*RaceHorses*
3%	[1]	11	9	10	12
	Proposed	19	21	20	18
	p-value	0.1441	0.0285	0.0679	0.2733
10%	[1]	17	10	16	14
	Proposed	13	20	14	16
	p-value	0.4652	0.0679	0.7150	0.7150

votes is 15 for each method under study. The p-value [144] of the test is indicated in the two tables. As a rule of thumb, the null hypothesis is rejected when $p < 0.05$. When this happens in Table 6.3 or 6.4, it means that the two methods under the comparison cannot be considered to have the same subjective quality, since one of them has obtained a statistically significantly higher number of votes, and therefore seems to have better quality.

In all of the 16 trials in Table 6.3 we have $p < 0.05$, which indicates that subjects showed a statistically significant preference for the proposed method vs. RECAP. Looking across all trials (i.e., summing up all the votes for the two options), the results show that participants have preferred the proposed method much more than RECAP (205 vs. 35 votes) with overall $p = 0.0001$, which is a very statistically significant result. This confirms that the proposed method is able to improve the perceptual quality of the concealed frames compared to the original RECAP method.

In Table 6.4, in all of the 16 trials except for one (*Soccer* at 3%) we have $p > 0.05$. This indicates that the subjective quality of the proposed error concealment method is statistically indistinguishable from our earlier method in [1] at the significance level $p = 0.05$ on all videos except for *Soccer* at 3% loss rate, where the result is significant in favor of the proposed method.

Fig. 6.3 shows a frame from the sequence *Crew* concealed by the three methods (RECAP, [1], and the proposed) based on a reference frame that is 10 frames away. One can easily see that our new method is able to improve the visual quality of the concealed frames compared to RECAP method, while the differences between the frames produced by the newly proposed method and that in [1] are harder to see. Indeed, this is to be expected, since both methods operate on similar principles by trying to reduce the saliency of concealed blocks.

6.5 Conclusions

Error concealment in loss-corrupted streaming video is a challenging under-determined problem. In the method described in this chapter, we add a low-saliency prior as a regularization term to the replacement block search problem. Low saliency provides the correct side information in ROI-based UEP video streaming systems for client to identify correct replacement blocks for concealment. Also, low saliency reduces viewer's visual attention on the loss-stricken regions. Incorporated into a previously proposed RECAP error concealment setup, our experimental results show that our method can clearly improve the visual quality of the loss-corrupted frames both objectively (up to 3.6 dB in PSNR) and subjectively. Moreover, incorporating the newly-developed convex approximation to visual saliency into the error concealment process results in expected complexity reduction of two orders of magnitude for CIF resolution video, while at the same time providing a gain of up to 0.7 dB in PSNR compared to an earlier version of the algorithm. Although we utilized RECAP as a platform to demonstrate the performance and effectiveness of our proposed low-saliency prior for video error concealment, other concealment methods can also benefit from the notion of a low-saliency prior. In fact, the low-saliency prior can be utilized by any video error concealment method that can offer multiple candidates for reconstructing missing blocks so as to reduce the ambiguity in the selection of correct blocks.

(a) (b)

(c) (d)

Figure 6.3: A frame from *Crew*: (a) original frame (b) the frame reconstructed by RECAP (PSNR = 34.3 dB) (c) the frame reconstructed by the method from [1] (PSNR = 36.6 dB) (d) the frame reconstructed by the proposed method (PSNR = 36.8 dB).

Chapter 7

Conclusions and Future Directions

7.1 Summary of contributions

In this dissertation, we presented various novel methods for utilizing visual saliency in the context of video compression and transmission. Specifically, we presented two novel computationally-efficient saliency estimation methods inspired by the well-known IKN saliency model. The first method is a convex approximation to the IKN saliency model, consisting of a spatial and a temporal component. Its spatial component can be used to estimate visual saliency in static images, while the two components together can be used to estimate the saliency in video. The computational cost of the spatial component is about 1/11-th of the complexity of the IKN model for images, while the combined complexity of the spatial and temporal components is about 1/9-th of that of the IKN model for video. The convexity of this approximation makes it very attractive to incorporate within various optimization procedures in image and video processing.

The second proposed saliency estimation method uses the spatial component from the convex approximation mentioned above, but improves temporal saliency estimation via global motion compensation. Overall, this method is not convex, but is more accurate than the IKN saliency model on certain sequences with camera motion. This method uses motion vectors to accomplish global motion compensation and subsequently temporal saliency estimation, so it can be very attractive for video compression applications where motion vectors are readily available. The complexity of this method is about 1/6-th of that of the IKN model for video.

During the course of this research, we also developed an eye-tracking dataset for a number of standard video sequences that are commonly used in the field of video compression and transmission. This dataset is publicly available online, and can be utilized for benchmarking and evaluation of visual saliency models and perceptually-motivated video processing algorithms as well as video quality assessment methods.

In the context of video compression, we presented a novel saliency-aware video compression method within a region-of-interest (ROI) video coding framework. In ROI-based video coding, ROIs are encoded with higher quality compared to non-ROIs. Hence, various coding artifacts may be produced in non-ROI parts, especially at low bit rates. Such coding artifacts may become attention-grabbing (visually salient), and draw viewer's attention away from ROI parts. This may degrade the perceived video quality as the visual quality in non-ROI parts is lower. The proposed saliency-aware video compression method attempts to reduce such attention-grabbing coding artifacts in non-ROI parts so as to keep viewer's attention on ROI parts. At the same time, the proposed method allows saliency to increase in high quality ROI parts of the frame, and decrease in non-ROI parts. It was demonstrated that the proposed method achieves higher video quality compared to conventional rate-distortion optimization, as well as two recent psychovisually-motivated video coding methods from the literature.

In the context of video transmission, we presented a novel saliency-cognizant video error concealment method for ROI-based video streaming. In ROI-based transmission, ROIs are protected more heavily than non-ROI parts, for example, using stronger channel codes. This way, if errors or losses occur during transmission, the affected regions will most likely be from non-ROI parts, and so they will be of low visual saliency. Hence, the reconstruction of the corrupted regions should be such that they end up with low visual saliency after error concealment; otherwise, if their saliency increases, they may grab viewer's attention and thereby degrade visual quality. To achieve this goal, we added a low saliency prior to the under-determined problem of error concealment. Such a prior serves two purposes. First, in ROI-based video streaming, low-saliency prior is likely the correct side information for reconstructing the lost block and helps the client identify the correct replacement block for concealment. Second, in the event that a perfectly matched block cannot be identified, the low-saliency prior reduces viewer's visual attention on the reconstructed region, and so the overall subjective quality of the reconstructed frame is increased. It was shown that this strategy leads to improved video quality of concealed frames, both objectively and

subjectively.

7.2 Future directions

Having summarized the contributions of this dissertation, we now outline several possible directions for future research.

In our proposed global motion-compensated saliency detection method we used a global motion compensation process to obtain the motion saliency of a video frame. The employed global motion compensation method uses only the motion vectors of the video frame. Better results, however, can be achieved if more compressed-domain information such as block coding (partition) mode is used for global motion compensation [166]. In particular, a motion segmentation and object tracking approach like the recent method proposed in [166] can be used to dynamically track foreground objects across different frames. The method in [166] uses both motion vectors and block coding modes to segment and track foreground objects by the help of a spatio-temporal Markov Random Field (ST-MRF) model. Hence, as a future work, we can use a method like [166] to improve our proposed GMC saliency detection method as well as our proposed saliency-aware video compression method.

In our proposed saliency-aware video compression method, we combined a saliency distortion term with the conventional MSE distortion metric. As a possible future work, the conventional MSE distortion metric can be replaced by a more perceptually-relevant distortion metric such as SSIM to achieve even better results. For instance, the reduced-reference SSIM estimation method proposed in [130] can be utilized in conjunction with the proposed saliency distortion metric to achieve better perceptual quality in video compression. Also, in Section 5.2.2, we set the saliency-related Lagrange multiplier λ_{S_i} based on (5.9) to either zero, or an experimentally determined value of 1.5. However, further adaptation of this Lagrange multiplier can be introduced based on the saliency of each macroblock. For example, the value of λ_S can be increased in ROI parts to emphasize the effect of saliency distortion in these regions.

Our proposed saliency-cognizant error concealment method attempts to reduce the saliency of the reconstructed regions in non-ROI parts of the frame so that the visual attention is not directed towards the reconstructed regions. As a future direction for improving our proposed saliency-cognizant error concealment method, an efficient method can be designed to deliberately increase the saliency of ROI parts of the frame after performing the

proposed error concealment method to make sure that the visual attention is directed away from the reconstructed regions as much as possible. For instance, the attention-guiding method from [167] can be utilized to further increase the visual saliency of ROI parts of the video frame. In particular, the saliency adjustment can be performed in such a way that the objective or perceptual quality of the manipulated ROI parts is not degraded too much. This can possibly be achieved by adding a distortion metric (e.g., MSE or SSIM) to the saliency adjustment process as a regularization term so that a trade off between the amount of saliency change and objective/subjective quality can be made.

We hope that the proposed methods and future directions can enlighten the future research in this increasingly attractive field.

Appendices

Appendix A

Various Cases For $\mathcal{N}(\mathbf{X})$

In Section 6.2.2, we introduced a matrix expansion operator $\mathcal{Z}(\mathbf{X}, \mathcal{N}(\mathbf{X}))$ for expanding a $N_b \times N_b$ matrix $\mathbf{X}$ to a $p \times p$ matrix $\mathbf{X}_e$ by zero-padding it based on the $p \times p$ spatial neighborhood $\mathcal{N}(\mathbf{X})$. As we mentioned in Section 6.2.2, $\mathcal{Z}(\mathbf{X}, \mathcal{N}(\mathbf{X}))$ can be realized by a linear transformation as follows:

$$\mathbf{X}_e = \mathcal{Z}(\mathbf{X}, \mathcal{N}(\mathbf{X})) = \mathbf{M}\mathbf{X}\mathbf{N}, \tag{A.1}$$

where $\mathbf{M}$ is a binary matrix of size $p \times N_b$ and $\mathbf{N}$ is a binary matrix of size $N_b \times p$. In this appendix, we derive $\mathbf{M}$ and $\mathbf{N}$ so that $\mathcal{Z}(\mathbf{X}, \mathcal{N}(\mathbf{X}))$ can be utilized in our error concealment methodology in Section 6.2.1.

Note that in our error concealment method, missing blocks are reconstructed in a raster-scan order. Hence, the causal neighbors of all missing blocks will always be available. However, the anti-causal neighbors of the missing blocks may be missing. Therefore, depending on the availability of the anti-causal neighbors of the missing block in a 8-connected neighborhood, we may encounter one of the cases depicted in Fig. A.1. For each of these cases, we obtain a different $\mathbf{M}$ and $\mathbf{N}$ as follows:

- Case 1 in Fig. A.1 shows the situation in which all the 8-connected neighbors of the current block are available, and we want to expand the current block $\mathbf{X}$ by zero-padding it from all sides. In this case, $\mathbf{M}$ and $\mathbf{N}$ are defined as follows

$$\mathbf{M} = \begin{pmatrix} [\mathbf{0}]_{\frac{(p-N_b)}{2} \times N_b} \\ [\mathbf{I}]_{N_b \times N_b} \\ [\mathbf{0}]_{\frac{(p-N_b)}{2} \times N_b} \end{pmatrix}_{p \times N_b}, \mathbf{N} = \mathbf{M}^t, \tag{A.2}$$

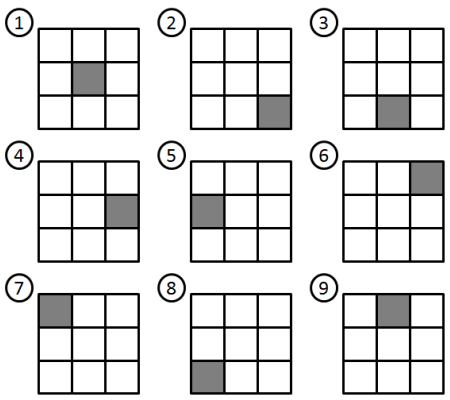

Figure A.1: In the proposed error concealment method, depending on the availability of the neighbors of a missing block, various situations may arise. In this figure, the missing block has been depicted by a gray box while its available neighbors have been depicted by white boxes. The available neighbors of the missing block $\mathbf{X}$ are used to define $\mathcal{N}(\mathbf{X})$.

where $[\mathbf{0}]_{x\times y}$ denotes a $x \times y$ matrix whose elements are all zero, and $[\mathbf{I}]_{x\times y}$ denotes the identity matrix of size $x \times y$.

- Case 2 in Fig. A.1 shows the situation in which only the causal 8-connected neighbors of the current block $\mathbf{X}$ are available, and we want to expand the current block by zero-padding it from the top and left. In this case, $\mathbf{M}$ and $\mathbf{N}$ are defined as follows

$$\mathbf{M} = \begin{pmatrix} [\mathbf{0}]_{(p-N_b)\times N_b} \\ [\mathbf{I}]_{N_b\times N_b} \end{pmatrix}_{p\times N_b}, \mathbf{N} = \mathbf{M}^t. \tag{A.3}$$

- Case 3 in Fig. A.1 shows the situation in which all the 8-connected neighbors of the current block $\mathbf{X}$ are available except for one or more of its neighbors from below, and we want to expand the current block by zero-padding it from the left, top, and right. In this case, $\mathbf{M}$ and $\mathbf{N}$ are defined as follows

$$\mathbf{M} = \begin{pmatrix} [\mathbf{0}]_{(p-N_b)\times N_b} \\ [\mathbf{I}]_{N_b\times N_b} \end{pmatrix}_{p\times N_b}, \tag{A.4}$$

$$\mathbf{N} = \begin{pmatrix} [\mathbf{0}]_{N_b\times \frac{(p-N_b)}{2}} & [\mathbf{I}]_{N_b\times N_b} & [\mathbf{0}]_{N_b\times \frac{(p-N_b)}{2}} \end{pmatrix}_{N_b\times p}. \tag{A.5}$$

- Case 4 in Fig. A.1 shows the situation in which all 8-connected neighbors of the current block are available except for one or more of its 8-connected neighbors to the right, and we want to expand the current block $\mathbf{X}$ by zero-padding it from the left, top, and bottom. In this case, $\mathbf{M}$ and $\mathbf{N}$ are defined as follows

$$\mathbf{M} = \begin{pmatrix} [\mathbf{0}]_{\frac{(p-N_b)}{2} \times N_b} \\ [\mathbf{I}]_{N_b \times N_b} \\ [\mathbf{0}]_{\frac{(p-N_b)}{2} \times N_b} \end{pmatrix}_{p \times N_b}, \tag{A.6}$$

$$\mathbf{N} = \begin{pmatrix} [\mathbf{0}]_{N_b \times (p-N_b)} & [\mathbf{I}]_{N_b \times N_b} \end{pmatrix}_{N_b \times p}. \tag{A.7}$$

- Case 5 in Fig. A.1 shows the situation in which the current block is on the left boundary of the frame and all of its 8-connected neighbors are available, and we want to expand the current block by zero-padding it from all sides except left. In this case, $\mathbf{M}$ and $\mathbf{N}$ are defined as follows

$$\mathbf{M} = \begin{pmatrix} [\mathbf{0}]_{\frac{(p-N_b)}{2} \times N_b} \\ [\mathbf{I}]_{N_b \times N_b} \\ [\mathbf{0}]_{\frac{(p-N_b)}{2} \times N_b} \end{pmatrix}_{p \times N_b}, \tag{A.8}$$

$$\mathbf{N} = \begin{pmatrix} [\mathbf{I}]_{N_b \times N_b} & [\mathbf{0}]_{N_b \times (p-N_b)} \end{pmatrix}_{N_b \times p}. \tag{A.9}$$

- Case 6 in Fig. A.1 shows the situation in which the current block is at the top-right corner of the frame and all of its 8-connected neighbors are available, and we want to expand the current block by zero-padding it from the left and bottom. In this case, $\mathbf{M}$ and $\mathbf{N}$ are defined as follows

$$\mathbf{M} = \begin{pmatrix} [\mathbf{I}]_{N_b \times N_b} \\ [\mathbf{0}]_{(p-N_b) \times N_b} \end{pmatrix}_{p \times N_b}, \tag{A.10}$$

$$\mathbf{N} = \begin{pmatrix} [\mathbf{0}]_{N_b \times (p-N_b)} & [\mathbf{I}]_{N_b \times N_b} \end{pmatrix}_{N_b \times p}. \tag{A.11}$$

- Case 7 in Fig. A.1 shows the situation in which the current block is at the top-left corner of the frame and all of its 8-connected neighbors are available, and we want to expand the current block by zero-padding it from the right and bottom. In this case, $\mathbf{M}$ and $\mathbf{N}$ are defined as follows

$$\mathbf{M} = \begin{pmatrix} [\mathbf{I}]_{N_b \times N_b} \\ [\mathbf{0}]_{(p-N_b) \times N_b} \end{pmatrix}_{p \times N_b}, \tag{A.12}$$

$$\mathbf{N} = \begin{pmatrix} [\mathbf{I}]_{N_b \times N_b} & [\mathbf{0}]_{N_b \times (p-N_b)} \end{pmatrix}_{N_b \times p}. \tag{A.13}$$

- Case 8 in Fig. A.1 shows the situation in which the current block is at the bottom-left corner of the frame and all of its 8-connected neighbors are available, and we want to expand the current block by zero-padding it from the top and right. In this case, $\mathbf{M}$ and $\mathbf{N}$ are defined as follows

$$\mathbf{M} = \begin{pmatrix} [\mathbf{0}]_{(p-N_b) \times N_b} \\ [\mathbf{I}]_{N_b \times N_b} \end{pmatrix}_{p \times N_b}, \tag{A.14}$$

$$\mathbf{N} = \begin{pmatrix} [\mathbf{I}]_{N_b \times N_b} & [\mathbf{0}]_{N_b \times (p-N_b)} \end{pmatrix}_{N_b \times p}. \tag{A.15}$$

- Case 9 in Fig. A.1 shows the situation in which the current block in on the top boundary of the frame and all of its 8-connected neighbors are available, and we want to expand the current block by zero-padding it from all sides except the top. In this case, $\mathbf{M}$ and $\mathbf{N}$ are defined as follows

$$\mathbf{M} = \begin{pmatrix} [\mathbf{I}]_{N_b \times N_b} \\ [\mathbf{0}]_{(p-N_b) \times N_b} \end{pmatrix}_{p \times N_b}, \tag{A.16}$$

$$\mathbf{N} = \begin{pmatrix} [\mathbf{0}]_{N_b \times \frac{(p-N_b)}{2}} & [\mathbf{I}]_{N_b \times N_b} & [\mathbf{0}]_{N_b \times \frac{(p-N_b)}{2}} \end{pmatrix}_{N_b \times p}. \tag{A.17}$$

For all other possible cases, we assume that $\mathcal{N}(\mathbf{X})$ covers only $\mathbf{X}$, and so we set both $\mathbf{M}$ and $\mathbf{N}$ to $N_b \times N_b$ identity matrices.

Bibliography

[1] H. Hadizadeh, I. V. Bajić, and G. Cheung, "Saliency-cognizant error concealment in loss-corrupted streaming video," in *Proc. IEEE Int. Conf. Multimedia Expo*, July 2012, pp. 73–79.

[2] L. Itti, C. Koch, and E. Niebur, "A model of saliency-based visual attention for rapid scene analysis," *IEEE Trans. Pattern Anal. Machine Intell.*, vol. 20, pp. 1254–1259, Nov. 1998.

[3] L. Itti and C. Koch, "A saliency-based search mechanism for overt and covert shifts of visual attention," *Vision Research*, vol. 40, pp. 1489–1506, 2000.

[4] W. James, *The Principles of Psychology.* Holt, New York, 1890.

[5] L. Itti, "Automatic foveation for video compression using a neurobiological model of visual attention," *IEEE Trans. Image Process.*, vol. 13, no. 10, pp. 1304–1318, 2004.

[6] A. Borji and L. Itti, "State-of-the-art in visual attention modeling," *IEEE Trans. Pattern Anal. Mach. Intell.*, vol. 35, no. 1, p. 185207, Jan. 2013.

[7] J. M. Shapiro, "Embedded image coding using zerotrees of wavelet coefficients," *IEEE Trans. Signal Process.*, vol. 41, pp. 3445–3462, Dec. 1993.

[8] P. T. Kortum and W. S. Geisler, "Implementation of a foveated image coding system for image bandwidth reduction," in *Human Vision and Electronic Imaging, SPIE Proceedings*, 1996, pp. 350–360.

[9] N. Doulamis, A. Doulamis, D. Kalogera, and S. Kollias, "Improving the performance of MPEG coders using adaptive regions of interest," *IEEE Trans. Circuits Syst. Video Technol.*, vol. 8, pp. 928–934, 1998.

[10] L. B. Stelmach, W. J. Tam, and P. J. Hearty, "Static and dynamic spatial resolution in image coding: An investigation of eye movements," in *Human Vision, Visual Processing, and Digital Display II, SPIE Proceedings*, 1991, pp. 147–152.

[11] M. Hannuksela, Y.-K. Wang, and M. Gabbouj, "Sub-picture: ROI coding and unequal error protection," *Proc. IEEE Int. Conf. Image Process.*, vol. 3, pp. 537 – 540, 2002.

[12] H. Hadizadeh, M. J. Enriquez, and I. V. Bajić, "Eye-tracking database for a set of standard video sequences," *IEEE Trans. Image Process.*, vol. 21, no. 2, pp. 898–903, Feb. 2012.

[13] H. Hadizadeh, I. V. Bajić, and G. Cheung, "Video error concealment using a computation-efficient low saliency prior," submitted to *IEEE Trans. Multimedia*. Available: http://mcl.ensc.sfu.ca/pubs/hbc-tmm-sub-2012.pdf, 2012.

[14] Y.-M. Chen and I. V. Bajić, "Motion vector outlier rejection cascade for global motion estimation," *IEEE Signal Process. Lett.*, vol. 17, no. 2, pp. 197–200, Feb. 2010.

[15] H. Hadizadeh and I. V. Bajić, "Saliency-aware video compression," submitted to *IEEE Trans. Image Process.*, Feb. 2013.

[16] ——, "Saliency-preserving video compression," *presented at IEEE Int. Conf. Multimedia Expo (AVCC)*, Jul. 2011.

[17] L. Itti and P. F. Baldi, "A principled approach to detecting surprising events in video," in *Proc. IEEE Conf. Comput. Vision Pattern Recog.*, San Siego, CA, Jun. 2005, pp. 631–637.

[18] M. Carrasco, "Visual attention: The past 25 years," *Vision Research*, vol. 51, pp. 1484–1525, 2011.

[19] L. Itti, G. Rees, and J. K. Tsotsos, *Neurobiology of Attention*. Academic Press, 2005.

[20] J. R. Anderson, *Cognitive psychology and its implications*. Worth Publishers, 2004.

[21] S. Fuller, R. Z. Rodriguez, and M. Carrasco, "Apparent contrast differs across the vertical meridian: Visual and attentional factors," *Journal of Vision*, vol. 8, no. 1, pp. 11–16, 2008.

[22] P. F. Montagna, B. and M. Carrasco, "Attention trades off spatial acuity," *Vision Research*, vol. 49, no. 7, pp. 735–745, 2009.

[23] L. Huang and K. R. Dobkins, "Attentional effects on contrast discrimination in humans: Evidence for both contrast gain and response gain," *Vision Research*, vol. 45, no. 9, pp. 1201–1212, 2005.

[24] J. Braun and B. Julesz, "Withdrawing attention at little or no cost: detection and discrimination tasks," *Perception and Psychophysics*, vol. 60, pp. 1–23, 1998.

[25] O. Hikosaka, S. Miyauchi, and S. Shimojo, "Orienting a spatial attention - its reflexive, compensatory, and voluntary mechanisms," *Brain Research and Cognitive Brain Research*, vol. 5, pp. 1–9, 1996.

[26] J. R. Bergen and B. Julesz, "Parallel versus serial processing in rapid pattern discrimination," *Nature*, vol. 303, pp. 1176–1196, 1983.

[27] A. M. Sillito and H. E. Jones, "Context-dependent interactions and visual processing in V1," *Journal of Physiology Paris*, vol. 90, pp. 205–209, 1996.

[28] J. B. Levitt and J. S. Lund, "Context-dependent interactions and visual processing in V1," *Nature*, vol. 387, pp. 73–76, 1997.

[29] A. L. Yarbus, *Eye-movements and Vision.* Plenum Press, 1967.

[30] M. Sodhi, B. Reimer, J. L. Cohen, Vastenburg, R. Kaars, and S. Kirsschenbaum, "On-road driver eye movement tracking using head-mounted devices," *Symp. Eye Tracking Research and Applications*, 2002.

[31] J. M. Henderson and A. Hollingworth, "High-level scene perception," *Ann. Rev. Psychology*, vol. 50, pp. 243–271, 1999.

[32] M. Land and M. Hayhoe, "In what ways do eye movements contribute to everyday activities," *Vision Research*, vol. 41, pp. 3559–3565, 2001.

[33] J. Shi and C. Tomasi, "Good features to track," *Proc. IEEE Conf. Computer Vision Pattern Recog.*, pp. 593–600, 1994.

[34] B. Triggs, "Detecting keypoints with stable position, orientation, and scale under illumination changes," *Proc. ECCV*, pp. 100–113, 2004.

[35] K. Yamada and G. W. Cottrell, "A model of scan paths applied to face recognition," *Proceedings of the Seventeenth Annual Cognitive Science Conference*, pp. 55–60, 1995.

[36] N. Sebe and M. S. Lew, "Comparing salient point detectors," *Pattern Recognition Letters*, vol. 24, pp. 89–96, Jan. 2003.

[37] T. Kadir and M. Brady, "Scale, saliency and image description," *International Journal of Computer Vision*, vol. 45, pp. 83–105, 2001.

[38] J. Harel, C. Koch, and P. Perona, "Graph-based visual saliency," in *Proc. NIPS*, 2006, pp. 313–335.

[39] V. Navalpakkam and L. Itti, "An integrated model of top-down and bottom-up attention for optimal object detection," *Proc. IEEE Computer Vision Pattern Recog.*, pp. 2049–2056, 2006.

[40] E. Borenstein and S. Ullman, "Learn to segment," *Proc. European Conference on Computer Vision*, pp. 315–328, 2004.

[41] P. Felzenszwalb, R. Girshick, D. McAllester, and D. Ramanan, "Object detection with discriminatively trained part based models," *IEEE Trans. Pattern Anal. Mach. Intell.*, no. 9, 2010.

[42] P. Viola and M. J. Jones, "Robust real-time face detection," *International Journal of Computer Vision*, no. 2, 2004.

[43] V. Navalpakkam and L. Itti, "Search goal tunes visual features optimally," *Neuron*, vol. 53, no. 4, pp. 605–617, 2007.

[44] A. M. Treisman and G. Gelade, "A feature integration theory of attention," *Cognitive Psychology*, vol. 12, pp. 97–136, 1980.

[45] C. Koch and S. Ullman, "Shifts in selective visual attention:towards the underlying neural circuitry," *Human Neurobiology*, vol. 4, pp. 219–227, 1985.

[46] J. K. Tsotsos, S. M. Culhane, W. Y. K. Wai, Y. Lai, N. Davis, and F. Nuflo, "Modeling visual attention via selective tuning," *Artificial Intelligence*, vol. 78, pp. 507–545, 1995.

[47] S. Baluja and D. Pomerleau, "Using a saliency map for active spatial selective attention:implementation and initial results," *Proc. NIPS*, pp. 451–458, 1994.

[48] C. Guo and L. Zhang, "A novel multiresolution spatiotemporal saliency detection model and its applications in image and video compression," *IEEE Trans. Image Process.*, vol. 19, no. 1, pp. 185–198, Jan. 2010.

[49] O. Le Meur and P. Le Callet, "What we see is most likely to be what matters : visual attention and applications," *Proc. IEEE Int. Conf. Image Process.*, pp. 3085–3088, 2009.

[50] S. Marat, T. Ho Phuoc, L. Granjon, N. Guyader, D. Pellerin, and A. Gurin-Dugu, "Spatio-temporal saliency model to predict eye movements in video free viewing," *Proc. 16th European Signal Process. Conf. (EUSIPCO'08)*, 2008.

[51] Y. Zhai and M. Shah, "Visual attention detection in video sequences using spatiotemporal cues," *Proc. ACM Int. Conf. Multimedia*, 2006.

[52] O. Boiman and M. Irani, "Detecting irregularities in images and in video," *Proc. IEEE Int. Conf. Computer Vision*, 2005.

[53] N. d. B. Bruce and J. K. Tsotsos, "Saliency based on information maximization," *Proc. Advances in Neural Info. Proc. Systems*, 2005.

[54] R. Desimone and J. Duncan, "Neural mechanisms of selective visual attention," *Ann. Rev. Neuroscience*, vol. 18, pp. 193–222, 1995.

[55] O. Le Meur, P. Le Callet, and D. Barba, "Predicting visual fixations on video based on low-level visual features," *Vision Research*, vol. 47, no. 19, pp. 2483–2498, Sep. 2007.

[56] B. A. Wandell, *Foundations of Vision*. Sinauer Associates, 1995.

[57] L. Itti and P. F. Baldi, "Bayesian surprise attracts human attention," in *Advances in Neural Inf. Process. Syst.* MIT Press, 2006, pp. 547–554.

[58] ——, "Bayesian surprise attracts human attention," *Vision Research*, vol. 49, no. 10, pp. 1295–1306, May 2009.

[59] A. Oliva, A. Torralba, M. S. Castelhano, and J. M. Henderson, "Top-down control of visual attention in object detection," *Proc. Int. Conf. Image Process.*, pp. 253–256, 2003.

[60] L. Zhang, M. H. Tong, T. K. Marks, H. Shan, and G. W. Cottrell, "SUN: a bayesian framework for saliency using natural statistics," *Journal of Vision*, vol. 8, no. 32, pp. 1–20, 2008.

[61] A. Torralba, "Modeling global scene factors in attention," *Journal of the Optical Society of America*, vol. 20, pp. 1407–1418, 2003.

[62] T. M. Cover and J. A. Thomas, *Elements of Information Theory.* John Wiley and Sons, 1991.

[63] D. Gao and N. Vasconcelos, "Discriminant saliency, the detection of suspicious coincidences, and applications to visual recognition," *IEEE Trans. Pattern Anal. Mach. Intell.*, vol. 31, no. 6, pp. 989–1005, Jun. 2009.

[64] C. Bishop, *Pattern Recognition and Machine Learning.* Springer, 2006.

[65] X. Hou and L. Zhang, "Saliency detection: A spectral residual approach," *Proc. IEEE Int. Conf. Computer Vision Pattern Recog.*, 2007.

[66] W. Kienzle, M. O. Franz, B. Scholkopf, and F. A. Wichmann, "Center-surround patterns emerge as optimal predictors for human saccade targets," *Journal of Vision*, vol. 9, p. 115, 2009.

[67] L. Itti, "Automatic foveation for video compression using a neurobiological model of visual attention," *IEEE Trans. Image Process.*, vol. 13, no. 10, pp. 1304–1318, 2004.

[68] N. D. B. Bruce and J. K. Tsotsos, "Saliency based on information maximization," *Proc. NIPS*, pp. 155–162, Jun. 2006.

[69] T. Judd, K. Ehinger, F. Durand, and A. Torralba, "Learning to predict where humans look," in *Proc. IEEE ICCV*, 2009.

[70] M. Cerf, J. Harel, W. Einhauser, and C. Koch, "Predicting human gaze using low-level saliency combined with face detection," *Proc. NIPS*, vol. 20, pp. 241–248, 2007.

[71] R. J. Peters and L. Itti, "Beyond bottom-up: Incorporating task dependent influences into a computational model of spatial attention," *Proc. IEEE Conf. Computer Vision Pattern Recog.*, 2007.

[72] Z. Li, S. Qin, and L. Itti, "Visual attention guided bit allocation in video compression," *Image and Vision Computing*, vol. 29, pp. 1 –14, 2011.

[73] J. Li, Y. Tian, T. Huang, and W. Gao, "Probabilistic multi-task learning for visual saliency estimation in video," *Int. Journal of Computer Vision*, vol. 90, pp. 150–165, 2010.

[74] F. Shic and B. Scassellati, "A behavioral analysis of computational models of visual attention," *Int. Journal of Computer Vision*, vol. 73, pp. 159–177, 2007.

[75] P. K. Mital, T. J. Smith, R. L. Hill, and J. M. Henderson, "Clustering of gaze during dynamic scene viewing is predicted by motion," *Cognitive Computation*, vol. 3, no. 1, pp. 5–24, Mar. 2011.

[76] "Stefan Winkler's website," http://stefan.winkler.net/.

[77] "Locarna systems," http://www.locarna.com.

[78] J. T. McClave and T. Sincich, *Statistics*. Prentice Hall, Upper Saddle River, NJ, 9th edition, 2003.

[79] ITU-R, "Recommendation BT.500-8: Methodology for the subjective assessment of the quality of television pictures," International Telecommunications Union, Tech. Rep., 1998.

[80] M. Cerf, E. P. Frady, and C. Koch, "Faces and text attract gaze independent of the task: Experimental data and computer model," *Vision Research*, vol. 9(12), no. 10, pp. 1–15, 2009.

[81] B. Tatler, R. Baddeley, and I. Gilchrist, "Visual correlates of fixation selection: Effects of scale and time," *Vision Research*, vol. 45, no. 5, pp. 643–659, 2005.

[82] "Saliency benchmark datasets," [Online] Available: http://people.csail.mit.edu/tjudd/SaliencyBenchmark/.

[83] S. Lee, M. S. Pattichis, and A. C. Bovik, "Foveated video quality assessment," *IEEE Trans. Multimedia*, vol. 4, pp. 129–132, Mar. 2002.

[84] Y. Fang, Z. Chen, W. Lin, and C.-W. Lin, "Saliency detection in the compressed domain for adaptive image retargeting," *IEEE Trans. Image Process.*, vol. 21, no. 9, pp. 3888–3901, Sep. 2012.

[85] R. Achanta, S. Hemami, F. Estrada, and S. Susstrunk, "Frequency-tuned salient region detection," in *Proc. IEEE Comput. Vision Pattern Recog.*, Miami Beach, FL, June 2009.

[86] J. W. Woods, *Multidimensional signal, image, and video processing and coding*, 2nd ed. Academic Press/Elsevier, 2012.

[87] H. Stark and J. W. Woods, *Probability, statistics, and random processes for engineers*, 4th ed. Pearson/Prentice Hall, 2012.

[88] J. S. Lim, *Two-dimensional signal and image processing.* Prentice Hall, 1989.

[89] A. Torralba and A. Oliva, "Statistics of natural image categories," *Network: Comput. Neural Syst.*, vol. 14, pp. 391–412, 2003.

[90] L. Itti, "Quantifying the contribution of low-level saliency to human eye movements in dynamic scenes," *Visual Cognition*, vol. 12, no. 6, pp. 1093–1123, 2005.

[91] Z. Wang and Q. Li, "Video quality assessment using a statistical model of human visual speed perception," *Journal of the Optical Society of America*, vol. 24, no. 2, pp. B61–B69, Dec. 2007.

[92] V. A. Mateescu, H. Hadizadeh, and I. V. Bajić, "Evaluation of several visual saliency models in terms of gaze prediction accuracy on video," in *Proc. IEEE Globecom'12 Workshop: QoEMC*, Dec. 2012.

[93] Y. Fang, Z. Chen, W. Lin, and C.-W. Lin, "Saliency detection in the compressed domain for adaptive image retargeting," *IEEE Trans. Image Process.*, vol. 9, no. 21, pp. 3888–3901, Sep. 2012.

[94] C. Chamaret, J. C. Chevet, and O. Le Meur, "Spatio-temporal combination of saliency maps and eye-tracking assessment of different strategies," *IEEE International Conf. on Image Proc.*, pp. 1077–1080, Sep. 2010.

[95] D. J. Sheskin, *Handbook of Parametric and Nonparametric Statistical Procedures*. Chapman & Hall/CRC, 2007.

[96] "iLab neuromorphic vision C++ toolkit," [Online] Available: http://ilab.usc.edu/toolkit/.

[97] B. Schauerte and R. Stiefelhagen, "Predicting human gaze using quaternion DCT image signature saliency and face detection," *Proc. IEEE WACV'12*, pp. 137–144, 2012.

[98] S. Goferman, L. Zelnik-Manor, and A. Tal, "Context-aware saliency detection," *Proc. IEEE Computer Vision Pattern Recog.*, pp. 2376–2383, Jun. 2010.

[99] Y. Fang, W. Lin, B. Lee, C. Lau, Z. Chen, and C. Lin, "Saliency detection model based on human visual sensitivity and amplitude spectrum," *IEEE Trans. Multimedia*, vol. 14, no. 1, pp. 187–198, Feb. 2012.

[100] H. J. Seo and P. Milanfar, "Static and space-time visual saliency detection by self-resemblance," *Journal of Vision*, vol. 9, no. 12, pp. 1–27, Nov. 2009.

[101] W. Kim, C. Jung, and C. Kim, "Spatiotemporal saliency detection and its applications in static and dynamic scenes," *IEEE Trans. Circuits Syst. Video Technol.*, vol. 21, no. 4, pp. 446–456, Apr. 2011.

[102] Y. Hochberg and A. C. Tamhane, *Multiple Comparison Procedures*. Hoboken, NJ: John Wiley and Sons, 1987.

[103] H. Hadizadeh, I. V. Bajić, and G. Cheung, "Complexity of saliency-cognizant error concealment based on the Itti-Koch-Niebur saliency model," [Online] Available: http://summit.sfu.ca/item/10942, Multimedia Communications Lab, Simon Fraser University, Tech. Rep. MCL-TR-2012-11-01, Nov. 2012.

[104] A. Smolic, M. Hoeynck, and J.-R. Ohm, "Low-complexity global motion estimation from P-frame motion vectors for MPEG-7 applications," in *Proc. IEEE Int. Conf. Image Process.*, vol. 2, Sep. 2000, pp. 271–274.

[105] G. H. Golub and C. F. Van Loan, *Matrix Computations*. Mathematics, 1996.

[106] M. A. Robertson and R. L. Stevenson, "DCT quantization noise in compressed images," *IEEE Trans. Circuits Syst. for Video Technol.*, vol. 15, no. 1, pp. 27–38, 2005.

[107] A. Leontaris, P. C. Cosman, and A. R. Reibman, "Quality evaluation of motion-compensated edge artifacts in compressed video," *IEEE Trans. Image Process.*, vol. 16, no. 11, pp. 943–956, Apr. 2007.

[108] Z. Chen, N. K. Ngan, and W. Lin, "Perceptual video coding: Challenges and approaches," in *Proc. IEEE Int. Conf. Multimedia Expo*, Jul. 2010, pp. 784–789.

[109] Y. Liu, Z. Li, and Y. C. Soh, "Region-of-interest based resource allocation for conversational video communications of H.264/AVC," *IEEE Trans. Circuits and Syst. Video Technol.*, vol. 18, no. 1, pp. 134 –139, 2008.

[110] S. Daly, "The visible difference predictor: an algorithm for the assessment of image fidelity," in *Digital Images and Human Vision*, A. B. Watson, Ed. MIT Press, 1993, pp. 179–206.

[111] I. E. Richardson, *The H.264 Advanced Video Compression Standard*. Wiley, 2010.

[112] T. Wiegand and B. Girod, "Lagrange multiplier selection in hybrid video coder control," *Proc. IEEE Int. Conf. Image Process.*, vol. 3, pp. 542–545, 2001.

[113] G. Sullivan and T. Wiegand, "Rate-distortion optimization for video compression," *IEEE Signal Process. Mag.*, vol. 15, no. 6, pp. 74–90, 1998.

[114] "The H.264/AVC JM reference software," [Online] Available: http://iphome.hhi.de/suehring/tml/.

[115] X. Li, N. Oertel, A. Hutter, and A. Kaup, "Laplace distribution based lagrangian rate distortion optimization for hybrid video coding," *IEEE Trans. Circuits Syst. Video Technol.*, vol. 19, no. 2, pp. 193–205, Feb. 2009.

[116] ——, "Advanced lagrange multiplier selection for hybrid video coding," in *Proc. IEEE Conf. Multimedia Expo*, July 2007, pp. 364–367.

[117] L. Chen and I. Garbacea, "Adaptive lambda estimation in Lagrangian rate-distortion optimization for video coding," in *Visual Commun. Image Process. (VCIP)*, Jan. 2006.

[118] J. Zhang, X. Yi, N. Ling, and W. Shang, "Context adaptive Lagrange multiplier (CALM) for rate-distortion optimal motion estimation in video coding," *IEEE Trans. Circuits Syst. Video Technol.*, vol. 20, no. 6, pp. 820–828, June 2010.

[119] M. Jiang and N. Ling, "On Lagrange multiplier and quantizer adjustment for H.264 frame-layer video rate control," *IEEE Trans. Circuits Syst. Video Technol.*, vol. 16, no. 5, pp. 663–669, May 2006.

[120] M. Wang and B. Yan, "Lagrangian multiplier based joint three-layer rate control for H.264/AVC," *IEEE Signal Process. Lett.*, vol. 16, no. 8, pp. 679–682, Aug. 2009.

[121] X. Yang, W. Lin, Z. Lu, E. Ong, and S. Yao, "Motion-compensated residue preprocessing in video coding based on just-noticeable distortion profile," *IEEE Trans. Circuits Syst. Video Technol.*, vol. 15, no. 6, pp. 742–752, Jun. 2005.

[122] Z. Chen and C. Guillemot, "Perceptually-friendly H.264/AVC video coding based on foveated just-noticeable-distortion model," in *IEEE Trans. Circuits Syst. Video Technol.*, vol. 20, no.6, June 2010, pp. 806–819.

[123] W. S. Geisler and J. S. Perry, "A real-time foveated multiresolution system for low-bandwidth video communication," *Proc. SPIE*, vol. 3299, pp. 294–305, Jul. 1996.

[124] Z. Wang and A. C. Bovik, "Embedded foveation image coding," *IEEE Trans. Image Proc.*, vol. 10, pp. 1397–1410, Oct. 2001.

[125] Z. Wang, L. Lu, and A. C. Bovik, "Foveation scalable video coding with automatic fixation selection," *IEEE Trans. Image Proc.*, vol. 12, no. 2, pp. 1–12, Feb. 2003.

[126] Z. Wang, A. C. Bovik, H. R. Sheikh, and E. P. Simoncelli, "Image quality assessment: From error visibility to structural similarity," *IEEE Trans. Image Process.*, vol. 13, no. 4, pp. 600–612, Apr. 2004.

[127] C. Yang, R. Leung, L. Po, and Z. Mai, "An SSIM-optimal H.264/AVC inter frame encoder," *Proc. IEEE International Conference on Intelligent Computing and Intelligent Systems*, vol. 4, pp. 291–295, 2009.

[128] C. Yang, H. Wang, and L. Po, "Improved inter prediction based on structural similarity in H.264,," *Proc. IEEE International Conference on Signal Processing and Communications*, vol. 2, pp. 340–343, 2007.

[129] Y. H. Huang, T. S. Ou, P. Y. Su, and H. Chen, "Perceptual rate-distortion optimization using structural similarity index as quality metric," *IEEE Trans. Circuits Syst. Video Technol.*, vol. 20, no. 11, pp. 1614–1624, Nov. 2010.

[130] S. Wang, A. Rehman, Z. Wang, S. Ma, and W. Gao, "SSIM-motivated rate-distortion optimization for video coding," *IEEE Trans. Circuits Syst. Video Technol.*, vol. 22, no. 4, pp. 516–529, Apr. 2012.

[131] X. Wang, L. Su, Q. Huang, and C. Liu, "Visual perception based Lagrangian rate distortion optimization for video coding," *Proc. IEEE Int. Conf. on Image Process.*, vol. 20, pp. 1653 – 1656, Sep. 2011.

[132] Z. G. Li, W. Gao, F. Pan, S. W. Ma, K. P. Lim, G. N. Feng, X. Lin, S. Rahardja, H. Q. Lu, and Y. Lu, "Adaptive rate control for H.264," *J. Visual Commun. Image Represent.*, vol. 17, pp. 376–406, Apr. 2006.

[133] N. Kamaci, Y. Altunbasak, and R. M. Mersereau, "Frame bit allocation for the H.264/AVC video coder via Cauchy-density-based rate and distortion models," *IEEE Trans. Circuits Syst. Video Technol.*, vol. 15, no. 8, pp. 994–1006, Aug. 2005.

[134] Z. Chen and K. N. Ngan, "Toward rate-distortion tradeoff in real-time color video coding," *IEEE Trans. Circuits Syst. Video Technol.*, vol. 17, no. 2, pp. 158–167, Feb. 2007.

[135] C. Yeo, Y. Han Tan, Z. Li, and S. Rahardja, "Mode-dependent transforms for coding directional intra prediction residuals," *Electronics Letters*, vol. 22, no. 4, pp. 545–554, Apr. 2012.

[136] A. K. Jain, *Fundamentals of Digital Image Processing.* NJ: Prentice-Hall, 1989.

[137] I.-M. Pao and M.-T. Sun, "Modeling DCT coefficients for fast video encoding," *IEEE Trans. Circuits Syst. Video Technol.*, vol. 9, no. 4, pp. 608–616, Jun. 1999.

[138] B. Widrow and I. Kollar, *Quantization Noise.* Cambridge, 2008.

[139] G. Bjontegaard, "Calculation of average PSNR differences between RD curves (VCEG-M33)," *VCEG Meeting (ITU-T SG16 Q.6)*, Apr. 2001.

[140] M. Pinson and S. Wolf, "A new standardized method for objectively measuring video quality," *IEEE Trans. Broadcasting*, vol. 50, no. 3, pp. 312–322, June 2004.

[141] S. Chikkerur, V. Sundaram, M. Reisslein, and L. J. Karam, "Objective video quality assessment methods: A classification, review, and performance comparison," *IEEE Trans. Broadcasting*, vol. 57, no. 2, pp. 165–182, June 2011.

[142] M. Taylor and C. Creelman, "PEST: Efficient estimates on probability functions," *Journal of Acoustical Society of America*, vol. 41, pp. 782–787, 1967.

[143] ITU-R, "Recommendation BT.500-8: Methodology for the subjective assessment of the quality of television pictures," ITU, Tech. Rep., 1998.

[144] D. J. Sheskin, *Handbook of Parametric and Nonparametric Statistical Procedures*. Chapman & Hall/CRC, 2007.

[145] "Cisco visual networking index: Forecast and methodology 2010-2015," http://www.cisco.com/.

[146] A. Kubota, A. Smolic, M. Magnor, M. Tanimoto, T. Chen, and C. Zhang, "Multi-view imaging and 3DTV," in *IEEE Signal Process. Mag.*, vol. 24, no.6, Nov. 2007.

[147] G.-M. Muntean, G. Ghinea, and T. Sheehan, "Region of interest-based adaptive multimedia streaming scheme," in *IEEE Trans. Broadcast.*, vol. 54, no.2, June 2008, pp. 296–303.

[148] F. Boulos, W. Chen, B. Parrein, and P. L. Callet, "A new H.264/AVC error resilience model based on regions of interest," in *Proc. 17th International Packet Video Workshop (PV 2009)*, Seattle, WA, May 2009.

[149] N. Bruce and P. Kornprobst, "Region-of-interest intra prediction for H.264/AVC error resilience," in *Proc. IEEE Int. Conf. Image Process.*, Cairo, Egypt, Nov. 2009.

[150] Y. Chen, Y. Hu, O. Au, H. Li, and C. W. Chen, "Video error concealment using spatio-temporal boundary matching and partial differential equation," in *IEEE Trans. Multimedia*, vol. 10, no.1, Jan. 2008, pp. 2–15.

[151] "Oxford dictionary: definition of concealment," [Online] Available: http://oxforddictionaries.com/definition/american_english/conceal.

[152] C. Yeo, W.-T. Tan, and D. Mukherjee, "Receiver error concealment using acknowledge preview (RECAP)–an approach to resilient video streaming," in *Proc. IEEE Int. Conf. Acoustics, Speech and Signal Process.*, Taipei, Taiwan, Apr. 2009.

[153] I. V. Bajić, "Error control for broadcasting and multicasting: An overview," in *Mobile Multimedia Broadcasting Standards: Technology and Practice*, F.-L. Luo, Ed. Springer, 2008, pp. 313–335.

[154] E. Maani and A. K. Katsaggelos, "Unequal error protection for robust streaming of scalable video over packet lossy networks," *IEEE Trans. Circ. Syst. Video Tech.*, vol. 20, no. 3, pp. 407–416, Mar. 2010.

[155] I. E. G. Richardson, *H.264 and MPEG-4 Video Compression: Video Coding for Next-Generation Multimedia*. NJ:Wiley, 2003.

[156] H. Hadizadeh and I. V. Bajić, "Burst loss resilient packetization of video," *IEEE Trans. Image Process.*, 2011.

[157] X. Hou and L. Zhang, "Saliency detection: A spectral residual approach," in *Proc. IEEE Comput. Vision Pattern Recog.*, Minneapolis, MN, June 2007.

[158] P. List, A. Joch, J. Lainema, G. Bjntegaard, and M. Karczewicz, "Adaptive deblocking filter," *IEEE Trans. Circuits Syst. Video Technol.*, vol. 13, no. 7, pp. 614–619, July 2003.

[159] P. P. Vaidyanathan, *Multirate Systems and Filter Banks*. Prentice-Hall, 1993.

[160] Y. Nesterov and A. Nemirovskii, *Interior-Point Polynomial Algorithms in Convex Programming*. Siam Studies in Applied Mathematics, 1994.

[161] S. Boyd and L. Vandenberghe, *Convex Optimization*. Cambridge University Press, 2004.

[162] J. R. Magnus and H. Neudecker, *Matrix Differential Calculus with Applications in Statistics and Econometrics*. Wiley, 1999.

[163] "cvx users guide," [online] http://cvxr.com/cvx/.

[164] R. W. Vuduc, "Automatic performance tuning of sparse matrix kernels," Ph.D. dissertation, Computer Science, University of California, Berkeley, Fall 2003.

[165] E. N. Gilbert, "Capacity of a burst-noise channel," *Bell Sys. Tech. J.*, vol. 39, pp. 1253–1266, Sep. 1960.

[166] S. H. Khatoonabadi and I. V. Bajić, "Video object tracking in the compressed domain using spatio-temporal Markov random fields," *IEEE Trans. Image Process.*, vol. 22, no. 1, pp. 300 – 313, Jan. 2013.

[167] A. Hagiwara, A. Sugimoto, and K. Kawamoto, "Saliency-based image editing for guiding visual attention," in *Proc. 1st International Workshop on Pervasive Eye Tracking and Mobile Eye-Based Interaction*, Beijing, China, Sep. 2011.